The Numerical Prediction of Panel Dent Resistance Incorporating Panel Forming Strains

by

Dylan Thomas

A thesis
presented to the University of Waterloo
in fulfillment of the
thesis requirement for the degree of
Master of Applied Science
in
Mechanical Engineering

Waterloo, Ontario, 2001

Acknowledgements

I would like to thank Mark Finn, Larry Sutak and Kevin Gong of ALCAN for their help and guidance during this research. Mark, your modelling expertise helped immensely, thanks for letting me use your computing resources. Larry, your knowledgeable guidance and help during dent testing was much appreciated.

Thanks to Michael Worswick for his guidance during this research. I owe Nathan Dwyer a debt of gratitude for his help with dent testing and submitting models. Thanks also go out to Steve Truttmann, Young Lee and Xavier Lalbin for their contributions during the research.

I would like to acknowledge the funding recieved by ALCAN, OGS and NSERC without which this research would not have been possible.

Finally, thanks Tasha for your patience, love and support during this research.

Dedication

To Mom, Dad
and Tasha.

Thanks for all the love
and support.

Abstract

This thesis presents a numerical method of predicting both static and dynamic denting phenomena in automotive body panels. The finite element method is used as a predictive tool to assess panel performance prior to production of tooling. A custom software package has been developed to transform existing finite element forming models into "ready-to-run" finite element denting models, minimising the effort required to perform dent simulations.

Over 50 multi-step finite element models were performed. Each of these models simulated the forming, springback and subsequent denting of either 1.05mm thick AA5754, or 0.81mm, 0.93mm or 1.00mm thick AA6111 aluminum sheet

Experimental validation of dent predictions using this method has shown that the trends in both static and dynamic dent resistance have been captured quite well. These validation studies demonstrated the sensitivity of the results to various parameters such as panel thickness, pre-strain, curvature and thickness, as well as numerical formulation parameters. It has been determined that it is particularly important to use forming data within the denting models for accurate results to be obtained.

Contents

1 Introduction 1

1.1 Motivation 1

1.2 Automotive Body Panels 2

1.2.1 Automotive Panel Stiffness 3

1.2.2 Panel Dent Resistance 5

1.2.3 Panel Stiffness and Dent Resistance Testing 11

1.3 Finite Element Method Applied to Dent Resistance Predictions 13

1.3.1 Forming Models 13

1.3.2 Springback Models 15

1.3.3 Static Dent Models 16

1.3.4 Dynamic Dent Models 17

1.4 Current Work 18

2 D-Mesh Software 21

2.1 Software Overview 21

2.2 Classes 22

2.2.1 Node Class 22

2.2.2 Shell Element Class 24

2.2.3 Solid Element Class 24

2.3 External Libraries 24

2.3.1 Standard Template Library 26

2.3.2 MOTIF Library 26

2.3.3 Tab Library 27

2.4 Program Flow 27
2.4.1 Input Routines 27
2.4.2 Element Refinement and Stress Remapping 28
2.4.3 Panel Curvature Approximation 33
2.4.4 Removal of Mid-Edge Nodes 38
2.4.5 Indentor Positioning 38
2.4.6 Output Routines 39

3 Materials Tested **44**
3.1 Material Selection 44
3.2 Material Characterisation 45

4 Experimental Procedures **56**
4.1 Panel Stamping 56
4.1.1 Specimen Preparation 61
4.1.2 Tooling Setup 62
4.2 Paint Bake Cycle 62
4.3 Static Dent and Panel Stiffness Tests 63
4.4 Dynamic Dent Tests 68

5 Finite Element Models **74**
5.1 Forming Models 76
5.1.1 Finite Element Mesh 76
5.1.2 Element Formulation 80
5.1.3 Contact 80
5.1.4 Friction 81
5.1.5 Drawbeads 82
5.1.6 Displacement Boundary Conditions 83
5.1.7 Anisotropy 85
5.1.8 Forming Model Output 86
5.2 Springback Models 86
5.2.1 Finite Element Mesh 86

5.2.2 Boundary Conditions 87
5.2.3 Element Formulation and Material Models 87
5.2.4 Springback Solution Control Parameters 88
5.2.5 Springback Model Output 88
5.3 Remeshing 89
5.4 Denting 90
5.4.1 Panel Stiffness and Static Denting 91
5.4.2 Element Formulation and Material Properties 91
5.4.3 SIGINI and HARDINI User Subroutines 92
5.4.4 Contact 92
5.4.5 Boundary Conditions 93
5.4.6 Static Denting Model Output 94
5.5 Dynamic Denting and Final Springback 94
5.5.1 Element Formulation and Material Properties 94
5.5.2 Contact 95
5.5.3 Boundary Conditions 95
5.5.4 Dynamic Denting Springback 95
5.5.5 Dynamic Denting Model Output 95

6 Experimental and Numerical Results 96
6.1 Panel Forming and Springback 96
6.1.1 Blank Draw-In and Final Shape 96
6.1.2 Panel Thickness 99
6.1.3 Forming Strains 100
6.2 Stiffness and Static Dent Tests 103
6.2.1 AA5754 Panel Load-Displacement Responses 104
6.2.2 AA6111 Panel Load-Displacement Responses 108
6.2.3 Panel Stiffness 114
6.2.4 Residual Dent Depths for the AA5754 panels. 115
6.2.5 Residual Dent Depths for the AA6111 Panels. 117
6.3 Dynamic Dent Tests 126
6.3.1 Dynamic Dent Response of the AA5754 panels. 126

6.3.2 Dynamic Dent Response of the AA6111 panels. 127
6.3.3 Sensitivity of the Dynamic Denting Results to Finite Element Model Parameters. 132

7 Discussion and Conclusion 137

7.1 Discussion 137
7.2 Conclusions 140
7.3 Recommendations 141

List of Tables

3.1 Summary of Tensile Tests Performed 48
3.2 Results of Tensile Tests 50
3.3 Aluminum Yield Strength Curve Coefficients 51

4.1 Summary of Dynamic Dent Tests Performed 70

5.1 Number of Finite Elements in Each Blank 79

6.1 AA5754 Panel Draw-in Summary. 98
6.2 AA6111 Panel Draw-in Summary. 98
6.3 Panel Thickness after Forming. 99
6.4 Initial Panel Stiffness Summary. 115
6.5 Secondary Panel Stiffness Summary. 116
6.6 Final Panel Stiffness Summary. 116

List of Figures

1.1 A Typical Autobody Panel Stiffness Plot 3
1.2 Static Dent Energy for Two Panels of Different Stiffness . . . 7
1.3 Dynamic Dent Depth Predictions of Worswick et al. 10
1.4 Static Dent Depth Predictions of Worswick et al. 11
1.5 Steps of a Finite Element Denting Prediction 14

2.1 D-Mesh Input Tab Window 23
2.2 Node Class Properties 23
2.3 Element mid-edge and Vertex Neighbours 25
2.4 Element Class Properties 25
2.5 Solid Element Class Properties 25
2.6 D-Mesh Remeshing Tab Window 29
2.7 Refinement of Shell Elements 29
2.8 Remeshing Parameters 31
2.9 Area Remeshing Function 31
2.10 Area Based Remeshing of A Finite Element Forming Model . 32
2.11 Shell Element Parametric Coordinate System 35
2.12 Shell Element Parametric Coordinate System 35
2.13 Shell Element Normal Calculation 36
2.14 Surface Tangent Calculation For a Quadrilateral Shell 36
2.15 Surface Tangent Approximation for a Triangular Shell 37
2.16 Curvature Approximation During Refinement 38
2.17 Mid-Edge Node Removal Rules 40
2.18 D-Mesh Indentor Tab Window 40

2.19 Positioning of an Indentor 41
2.20 D-Mesh Output Tab Window 42

3.1 Automated Tensile Testing Robot 46
3.2 Tensile Test Extensometers 47
3.3 Tensile Test Specimen 49
3.4 AA5754-O True Stress - Effective Plastic Strain Curve 52
3.5 AA6111 0.81mm True Stress - Effective Plastic Strain Curve . 53
3.6 AA6111 0.93mm True Stress - Effective Plastic Strain Curve . 54
3.7 AA6111 1.0mm True Stress - Effective Plastic Strain Curve . . 55

4.1 Sketch of IRDI Panel 57
4.2 Curvature and Dent locations of the IRDI Panel 57
4.3 IRDI Press 58
4.4 IRDI Die Set 60
4.5 IRDI Binder Configuration 61
4.6 Wrinkling of the IRDI Pan 64
4.7 Static Dent Experimental Setup 64
4.8 Closeup of a Static Dent Test 65
4.9 Bubble-Type Level 66
4.10 Digital Gauge Measurement of Displacement 67
4.11 Dynamic Dent Experimental Setup 69
4.12 Measurement of Panel Location 72
4.13 Plumb-Bob and Magnetic Coil 73

5.1 Finite Element Mesh of the IRDI Tooling 78
5.2 Adapted Finite Element Mesh 79
5.3 Schematic of a Drawbead 82
5.4 IRDI Drawbead Restraining Forces 84
5.5 IRDI Drawbead Normal Forces 84
5.6 Die and Binder Velocity Boundary Condition. 85
5.7 A Refined Finite Element Mesh 90

6.1 Draw-In of the AA5754 Panel 97
6.2 Predicted AA5754 Panel Strains - X-Direction 101
6.3 Predicted AA5754 Panel Strains - Y-Direction 101
6.4 Predicted AA6111 1.0mm Panel Strains - X-Direction 102
6.5 Predicted AA6111 1.0mm Panel Strains - Y-Direction 102
6.6 Predicted AA6111 1.0mm Panel EPS Strains 104
6.7 Static Load vs Displacement of indentor on 1.05mm AA5754 at Point A 105
6.8 Static Load vs Displacement of indentor on 1.05mm AA5754 at Point B 106
6.9 Static Load vs Displacement of indentor on 1.05mm AA5754 at Point C 106
6.10 Static Load vs Displacement of indentor on 1.05mm AA5754 at Point D 107
6.11 Static Load vs Displacement of indentor on 1.05mm AA5754 at Point E 107
6.12 Static Load vs Displacement of indentor on 0.81mm AA6111 at Point A 109
6.13 Static Load vs Displacement of indentor on 0.81mm AA6111 at Point B 110
6.14 Static Load vs Displacement of indentor on 0.81mm AA6111 at Point C 110
6.15 Static Load vs Displacement of indentor on 0.93mm AA6111 at Point A 111
6.16 Static Load vs Displacement of indentor on 0.93mm AA6111 at Point B 111
6.17 Static Load vs Displacement of indentor on 0.93mm AA6111 at Point C 112
6.18 Static Load vs Displacement of indentor on 1.00mm AA6111 at Point A 112

6.19 Static Load vs Displacement of indentor on 1.00mm AA6111 at Point B 113
6.20 Static Load vs Displacement of indentor on 1.00mm AA6111 at Point C 113
6.21 Residual Dent Depth vs Peak Load on 1.05mm AA5754 at Point A 118
6.22 Residual Dent Depth vs Peak Load on 1.05mm AA5754 at Point B 118
6.23 Residual Dent Depth vs Peak Load on 1.05mm AA5754 at Point C 119
6.24 Residual Dent Depth vs Peak Load on 1.05mm AA5754 at Point D 119
6.25 Residual Dent Depth vs Peak Load on 1.05mm AA5754 at Point E 120
6.26 Residual Dent Depth vs Peak Load on 0.81mm AA6111 at Point A 120
6.27 Residual Dent Depth vs Peak Load on 0.81mm AA6111 at Point B 121
6.28 Residual Dent Depth vs Peak Load on 0.81mm AA6111 at Point C 121
6.29 Residual Dent Depth vs Peak Load on 0.93mm AA6111 at Point A 122
6.30 Residual Dent Depth vs Peak Load on 0.93mm AA6111 at Point B 122
6.31 Residual Dent Depth vs Peak Load on 0.93mm AA6111 at Point C 123
6.32 Residual Dent Depth vs Peak Load on 1.00mm AA6111 at Point A 123
6.33 Residual Dent Depth vs Peak Load on 1.00mm AA6111 at Point B 124

6.34 Residual Dent Depth vs Peak Load on 1.00mm AA6111 at Point C 124
6.35 Residual Dent Depth vs Peak Load for three thicknesses of AA6111 at Point A 125
6.36 Dynamic Dent Test Results - 1.05mm AA5754 Panels 126
6.37 Dynamic Dent Test Results - 0.81mm AA6111 Panels 129
6.38 Dynamic Dent Test Results - 0.93mm AA6111 Panels 129
6.39 Dynamic Dent Test Results - 1.00mm AA6111 Panels 130
6.40 Effect of AA6111 Panel Thickness at Point A 130
6.41 Effect of AA6111 Panel Thickness at Point B 131
6.42 Effect of AA6111 Panel Thickness at Point C 131
6.43 Sensitivity of Dent Depth to Finite Element Parameters. . . . 133

7.1 Yield Function Comparison 139

Chapter 1

Introduction

1.1 Motivation

A key performance indicator limiting the potential usage of aluminum alloy sheet in automotive body panels is dent resistance. This material is attractive in automotive body applications due to the weight savings and resulting fuel economy improvements over current steel autobodies that are necessary to meet current and anticipated legislative fuel consumption standards. The cost to replace steel body panels with aluminum alloy sheet is roughly \$1.00 per pound of steel removed which currently represents a barrier to the widespread use of aluminum. A significant component of this cost penalty is introduced through the need to utilise thicker gauges of aluminum sheet in order to meet panel stiffness and dent resistance requirements. The opportunity to reduce panel thickness exists, but a fundamental understanding of the mechanical and material parameters controlling the denting process and the interaction between forming and denting are needed to allow an engineered approach to panel optimisation.

1.2 Automotive Body Panels

Historically, automotive body panels have been manufactured from steel sheet. The sheet is stamped into the required shape using tooling which is mounted in a large mechanical press. Two stampings are required for each automotive panel, known as the “inner” and the “outer”. The outer or closure panel embodies the “shape” of the vehicle and is also subject to external loads due to wind loading, palm-prints and hail, for example. The inner panel is shaped to provide structural support (stiffness) for the closure panel and is attached to the car structure. The inner is joined to the outer using a hemming process that bends the edges of the outer panel around the inner. In addition, a heat-curable adhesive known as mastic is used to bond inner regions of the panels together. The panels are then joined to the frame of the automobile and can either be stressed members, as in a unibody construction, or non-stressed members, as in a space-frame construction.

Recent advances in vehicle construction have seen the replacement of conventional steel sheet with higher strength, lighter gauge steels and in some cases aluminum. Typically the use of aluminum panels has been limited to those that can be bolted on, such as hoods, liftgates and decklids. Advances in material processing has led to the development of heat-treatable steels and aluminum alloys with good formability. These materials typically have a low yield strength to allow reasonable formability, but when heated for a period of time exhibit a yield strength increase. The hardening kinetics of materials used in closure panels have been optimised to harden during the paint bake cycle of the manufacturing process. Examples of such materials are North American steels 210B BA and 210 CA, European steel 220B, and aluminum alloys such as AA6111 and AA6016.

All automotive body panels require several desirable characteristics in their final form. Panel stiffness has to be sufficiently high so that the outer panels can resist externally applied loads and fluttering due to wind loading at speed. Panel dent resistance is also desirable so that damage does not occur during manufacturing, shipping and end use. Customer awareness of these two panel characteristics has been increased through recent marketing strategies of Saturn and Volkswagen, for example. The factors affecting panel stiffness and dent resistance in automotive panels are discussed in the following sections.

1.2.1 Automotive Panel Stiffness

Automotive panel compliance is defined as the rate at which the panel displaces with respect to a normally applied load. Conversely, stiffness is the inverse of compliance. A typical curve of applied load versus panel displacement is shown in Figure 1.1. This figure highlights three distinct stiffness regions observed in many curved automotive panels. These stiffness regions are known as the initial (1), secondary (2) and final stiffnesses (3).

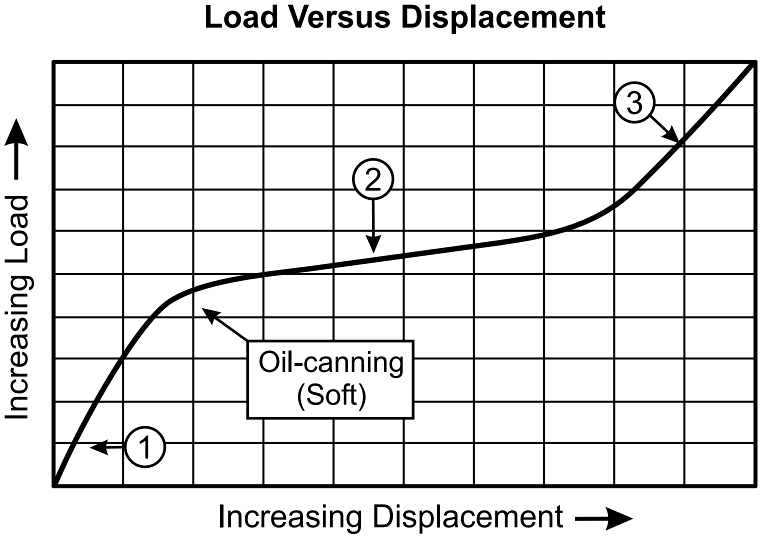

Figure 1.1: A typical autobody panel stiffness plot showing the three stiffness regions in a curved panel and the point at which the oil-canning response occurs.

The initial panel stiffness is known to be a function of elastic material properties such as Young's modulus, material thickness, curvature and supporting conditions (van Veldhuizen *et al.* [1]). In the initial stiffness region, the applied load is supported primarily by bending and compressive membrane stresses in the panel. As the applied load is increased, automotive panels exhibit a geometric softening response known as oil-canning. This panel softening occurs as the local curvature of the panel changes from a convex shape to a concave shape. The name “oil-canning” was given to this response as the base of old-style oil cans exhibited the same softening behaviour when pressed during use. This oil-canning response has two types, hard and soft. In a soft oil-canning response, the automotive panel remains in contact with the indentor, while in a hard oil-canning response, the panel can snap through, moving away from the indentor. In Figure 1.1, a soft oil-canning response is shown at the transition between initial and secondary stiffnesses. During the secondary stiffness region, the load is carried by a combination of bending and tensile membrane stresses. The panel stiffness increases again during the final stage as more of the load is carried by membrane tension. Often, the panel supporting conditions affect the stiffness in this region as well.

Several studies have been undertaken in order to understand the factors affecting panel stiffness. Mahmood [2] and Vadhavkar *et al.* [3] have stated that the initial stiffness of an unsupported autobody panel can be estimated using the following equation that was derived from spherical shell theory:

$$S = \frac{9.237 E t^2 h \pi^2}{k L_1 L_2 \sqrt{1-\nu^2}} \tag{1.1}$$

where S is the panel stiffness, E is Young’s modulus, t is the material thickness, ν is Poisson’s ratio and L_1,L_2 are the unsupported panel lengths. The value of k is 7.5 for $4 \leq \frac{h}{t} \leq 15$ and 6.3 for $15 \leq \frac{h}{t} \leq 60$. The panel crown height (h) can be estimated using:

$$h = \frac{L_1^2}{8R_1} + \frac{L_2^2}{8R_2} \tag{1.2}$$

where R_1,R_2 are the principal radii of curvature, corresponding to L_1,L_2. Unfortunately, as shown by Alaniz *et al.* [4], the applicability of Equation (1.1) is limited to the initial stiffness region shown in Figure 1.1. There are no known analytical solutions to calculate stiffness in the secondary and final regions, within which the deformation required to produce a visible dent normally occurs.

1.2.2 Panel Dent Resistance

A key distinction that is sometimes lacking in dent resistance studies is the nature of the dent. There are two types of denting that are of equal importance, static and dynamic denting. Static denting refers to a gradually applied load over a small area typified by a hand pushing on a hood. Dynamic denting occurs under impact loading typified by a hail stone. The key difference is the nature of load application, a static dent indicates a slowly applied force while a dynamic dent is driven by inertia and impact energy.

1.2.2.1 Static Dent Resistance

One of the first studies of static dent resistance was by DiCello and George [5]. They concluded that the energy required to produce a visible static dent on a panel could be represented by the equation:

$$W = K\frac{\sigma_y^2 t^4}{S} \tag{1.3}$$

where W is energy input during the loading of the panel via an indentor, K is a constant, σ_y is the panel yield strength, t is the panel thickness and S is the stiffness of the panel. DiCello and George described panels that could absorb high levels of input energy without producing a visible dent as having good static dent resistance. This definition of static dent resistance is different from that suggested by Yutori *et al.* [6], who described a panel with good static dent resistance as one that could support a large load prior to permanent indentation. From experiments performed on steel cylindrical shells of varying radii, Yutori *et al.* [6] formulated the following equation that describes the static load required to initiate a dent on a curved panel:

$$P_d = Kt^n\sigma_y \tag{1.4}$$

In Equation (1.4), P_d is the minimum load (in N) required to initiate a dent, K is a panel dependent constant, t is the sheet thickness (in mm) and n was experimentally determined to lie between 2.3 $\sim$ 2.4 for their steel panels. The yield strength, (σ_y) had units of MPa.

Interestingly, DiCello and George [5] and Yutori *et al.* [6] adopted different definitions of panel dent resistance and consequently arrived at conflicting conclusions regarding the effect that panel stiffness has on dent resistance. DiCello and George concluded that a less stiff panel was good for dent resistance whereas Yutori *et al.* concluded the opposite, that stiffer panels were more dent resistant.

Figure 1.2 illustrates how both conclusions regarding the effect of stiffness on panel dent resistance are true when the different definitions of static dent resistance is taken into account. The figure shows the load and unload curves for two panels of different stiffnesses, but equal thickness and yield strengths. For illustration purposes, it is assumed that the two panels experience the same residual dent depth (point 3 in the figure), but that the load to produce this dent is higher for the stiffer panel (point 1), compared to the more compliant panel (point 2). DiCello and George defined the static denting energy to be the work done on each panel; that is, the area under the loading curve. In Figure 1.2, the lower stiffness panel requires more work to produce a visible dent (point 3) even though the peak force at point 2 is less than at point 1. DiCello and George reasoned that this was due to the stiffer panels exhibiting less elastic deflection and would conclude that the more compliant panel was more dent resistant. In contrast, Yutori *et al.* [6] would conclude that the panel supporting the highest load for a given dent depth, in this case the stiffer panel, had the superior dent resistance. In light of these conflicting definitions of static dent resistance, for the purposes of this work, the static

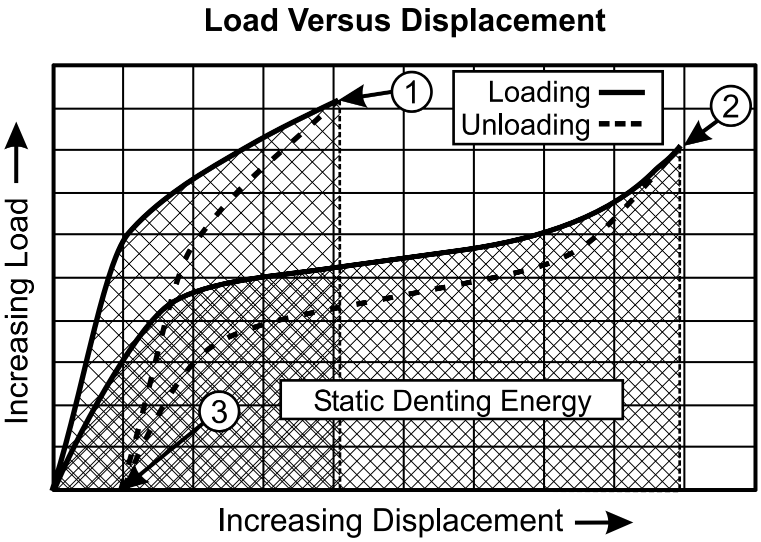

Figure 1.2: Hypothetical static dent loading and unloading curves with dent energy for two theoretical panels of equal thicknesses and yield strength, but of different curvatures. The stiffness of curve 1 is higher due to a tighter radius of panel curvature. Both panels were loaded to different forces that resulted in an identical, barely visible dent depth.

dent resistance of a panel will be taken as the load the panel supports prior to permanent indentation.

Mahmood [7] expanded on the work of DiCello and George, by incorporating the estimate of stiffness given by Equation (1.1) into DiCello's Dent Energy Equation (1.3). Mahmood states that the stiffness of either a shallow spherical shell [8] or an unsupported rectangular area can be used, resulting in the following expression for the energy required to statically dent a panel:

$$W = \frac{C_2 k a \sqrt{1-\nu^2}\sigma_y^2 t^2}{Eh} \tag{1.5}$$

C_2 is a constant that should not be calculated, as this equation is meant for relative comparisons of the dent resistance of similar panels. The term k equals 7.5 for $4 \leq \frac{h}{t} \leq 15$ and equals 6.3 for $15 \leq \frac{h}{t} \leq 60$. The area of the panels, a, can be calculated using either the area of a circular or rectangular unsupported area, whichever fits the dent location best. E, ν, and σ_y are Young's modulus, Poisson's ratio and the material yield strength. h is the crown height of the panel and t is the material thickness. Mahmood used these equations to design liftgate and decklid slam areas that were resistant to dents.

More recently, van Veldhuizen *et al.* [1] used the same definition of static dent resistance as that of Yutori *et al.* [6] and concluded that a power law equation similar to Equation (1.4) could be used to determine the load required to produce small dents. This equation has the form:

$$F_\delta = C \left(\frac{\delta}{\delta_0}\right)^\alpha \left(\frac{\sigma_y}{\sigma_0}\right)^\beta \left(\frac{t}{t_0}\right)^\gamma \tag{1.6}$$

where: C is a constant in Newtons, F_δ is the dent force in Newtons, δ is the dent depth in millimeters, σ_y is the yield strength in MPa and t is the material thickness. The denominators of δ_0, σ_0 and t_0 are factors that ensure the dimensional integrity of the equation and have magnitudes of $1mm$, $1N/mm^2$ and $1mm$ respectively. The results of their work on aluminum specimens yielded the following simplification of Equation (1.6) that could be used to calculate the load required to produce a barely visible dent of 0.1mm:

$$F_{0.1} = 0.557\sigma_y^{1.1}t^{1.5} \tag{1.7}$$

where the units are consistent with Equation (1.6), above. It is worthwhile to note that results of tests performed on steel samples had a similar form, but showed a dependence on curvature as well. This was confirmed by tests performed by McCormick *et al.* [9].

1.2.2.2 Dynamic Dent Resistance

There have been several studies published on dynamic denting; one of the first was by Johnson and Schaffnit [10]. Their experiments consisted of dropping an indentor onto rigidly constrained, flat, low-carbon steel plates of different thicknesses and yield strengths. For their work, they defined dynamic dent resistance as the following ratio:

$$Dent\ Resistance\ \ (D_r) = \frac{impact\ energy}{dent\ depth} \tag{1.8}$$

which they used to compare They were able to establish that the dent resistance of their samples followed the following relationship:

$$D_r \propto \sigma_y(\dot{\epsilon})t^2 \tag{1.9}$$

where D_r is the dent resistance of the sample, σ_y is the sample yield strength and t is the sheet thickness. They stressed that, for steels, it was imperative that the yield strength be corrected for the strain rate at which the dent took place. Unfortunately their experiment was designed so that little or no rebound of the indentor was noted. This implies that the sheet was absorbing most of the impact energy through plastic work. It is well known that if most of the impact energy can be absorbed elastically, then there will be little or no plastic work on the sheet. This results in better dynamic dent resistance. This has lead to the conclusion that panels of lower stiffness are better for dynamic dent resistance as shown by Worswick *et al.* [11].

In another dynamic dent resistance study, Burley *et al.* [12] showed that there exists a linear relationship between impact velocity and dent depth. Moreover, there exists a finite velocity below which no residual dent will be observed. These results have been confirmed in many subsequent studies [12–17]. More importantly, Burley *et al.* [12] also showed that dynamic dent resistance was not merely a function of yield strength and thickness, as reported by Johnson and Schaffnit [10], but was affected by factors such as panel density, modulus of elasticity and curvature.

The work of Nomura *et al.* [18] concluded that the dent resistance of curved panels did not always increase with sheet thickness, as was the case with flat panels. Their work also showed that the flatter panels tended to have better dynamic dent resistance. Worswick *et al.* [11] added to this by examining a full range of curvatures, from flat to highly curved. They showed that dynamic dent resistance for a panel will reach a maximum at one level of curvature, but will decrease for both flatter and more curved configurations, as shown in Figure 1.3. Interestingly, at the curvature for which a minimum dynamic dent occurred, a maximum static dent occurred. This opposing behaviour is evident when Figure 1.3 is compared to Figure 1.4.

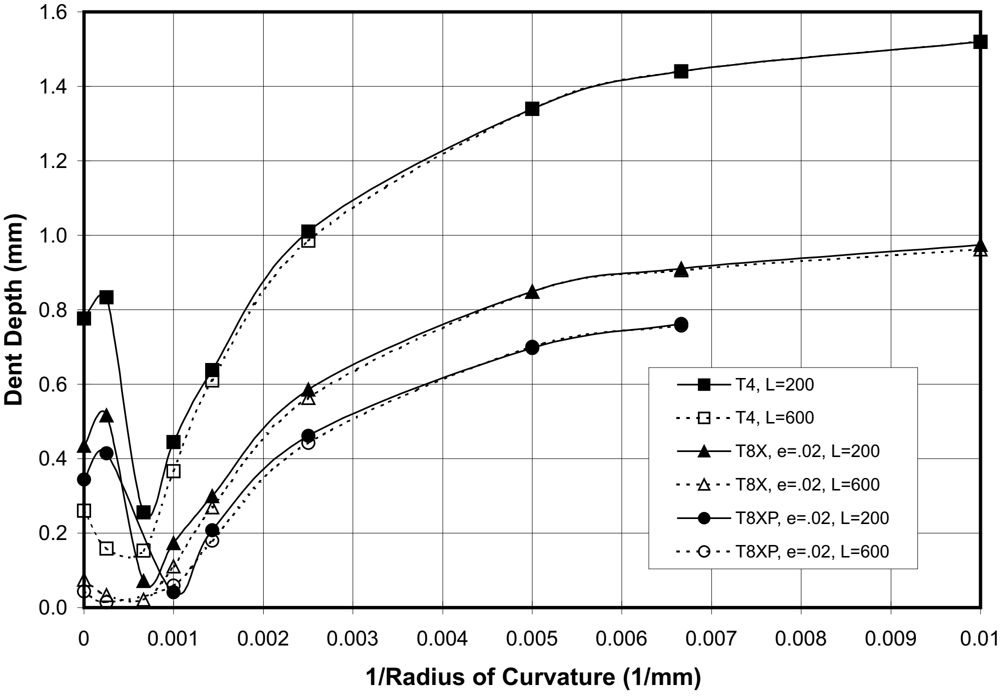

Figure 1.3: Dynamic dent depth predictions of Worswick *et al.* [11] for 1.0mm AA6111 sheet of varying prestrain (e), curvature (R), support span (L) and temper. Predictions are for a 25.4mm ball bearing dropped from 1219.2mm above the panel.

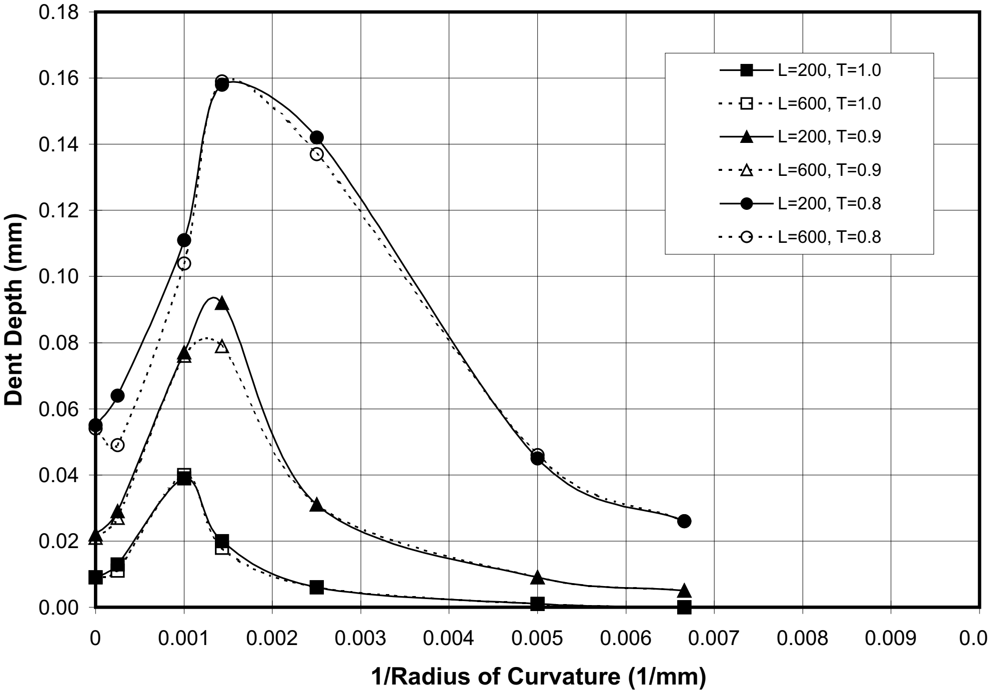

Figure 1.4: Static dent depth predictions of Worswick *et al.* [11] for AA6111 panels of varying thickness (T), curvature (R), and support span (L). Predictions are for a 25.4mm ball bearing dropped from 1219.2mm above the panel.

1.2.3 Panel Stiffness and Dent Resistance Testing

Even though there has been considerable work on panel stiffness [4, 19–21], static dent resistance [1, 3–7, 9, 16, 19, 20, 22–38] and dynamic dent resistance [3, 5, 10, 12–16, 19, 34, 37, 39–44], the automotive industry is just starting to adopt standardised test methods. A recent report published by the Standardized Dent Resistance Test Task Force (an Auto/Steel Partnership) [34], contains guidelines for performing stiffness and dent tests. Key points of this report include specification of indentor types, static load application methods, indentor velocities for dynamic denting and specification of the depth of a barely visible dent.

Although numerous types of indentors have been used in prior works, only two types of indentors are recommended for static denting. These are a steel hemispherical indentor and a flat rubber disk. The steel hemispherical indentor is 25.4mm in diameter and is meant to simulate elbow marks, luggage rack damage, thumb prints, etc. This indentor is recommended for use on laboratory prepared specimens, automotive outer body panels, or full vehicle testing. The flat rubber disk is 50.8mm in diameter and is meant to simulate palm, knee, hip and large object panel denting on automotive outer body panels or full vehicles.

For dynamic denting, the Standardized Dent Resistance Test Task Force recommends use of a 25.4mm steel ball. Experience shows that this type of indentor can produce sufficient impact energy to generate visible dents when dropped from heights up to 5 meters.

There has been considerable debate over what constitutes a “barely visible dent” in the literature. DiCello and George [5] used a dent depth of 0.0254mm (0.001 inches), which was the smallest dent that could be measured. Seel [17] determined that on average, a dent first becomes visible at 0.08mm. Other studies by Nomura *et al.* [18] and McCormick *et al.* [9], have designated dent depths of 0.1mm as barely visible.

The experimental program for the current study was derived from recommendations based on experience of ALCAN personnel [45] and the test procedures set out in the Auto/Steel Partnership report [34]. The actual testing methods used in this work are described in Chapter 4.

It has been mentioned that dent resistance is a function of many coupled influences such as panel stiffness, curvature, support conditions and material strength. In addition, the effects of prior work, that is, thickness reduction and work hardening during panel stamping must be considered when optimising panels for weight. In an effort to include more of the factors contributing to panel dent resistance, several researchers have used the finite element method (FEM) as a means of predicting panel stiffnesses and both static and dynamic dent resistance. An overview of application of the finite element method to predict panel stiffness and denting characteristics is discussed next.

1.3 Finite Element Method Applied to Dent Resistance Predictions

A principle goal of this research is to produce software tools and methodologies which can be used with the finite element method (FEM) to accurately predict panel stiffness and dent resistance. A flow chart of the complete process is shown in Figure 1.5. The prediction of a dent requires several steps, the first being a sheet metal forming analysis. This step is followed by a springback prediction where the stamped panel is removed from the tooling and allowed to deform due to the residual stresses in the sheet from the forming stage. Once the finite element model has been allowed to springback, the mesh in the model must often be locally refined so that an accurate denting prediction can be performed. This denting prediction can be either static or dynamic; if a dynamic dent is being simulated, then an additional springback simulation step is required. Complicating the issue of dent resistance prediction is the number of software programs required to perform this type of analysis. The individual stages of dent and stiffness prediction are discussed in the following sections.

1.3.1 Forming Models

An accurate prediction of a dent begins with the initial finite element forming model. This model must capture the panel stamping process accurately to predict the panel prestrain, shape and thickness changes. In industry, finite element software codes such as LS-DYNA[46], PAMSTAMP[47], OPTRIS[48] and AUTOFORM[49] are routinely used to predict the formability of autobody panels. The particular software used for this research was

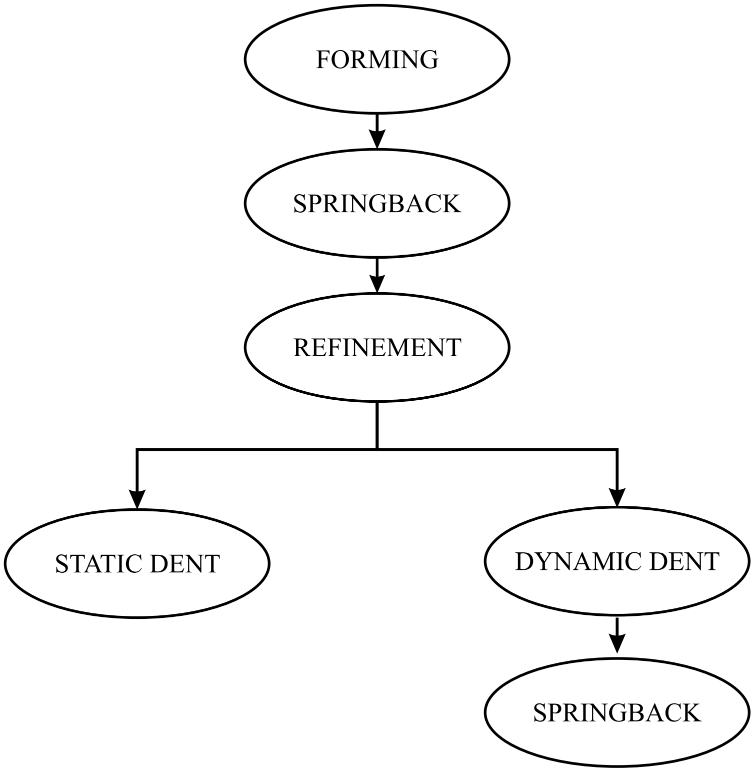

Figure 1.5: The steps required to accurately predict the static or dynamic dent of a panel using the finite element method. Each bubble requires a finite element simulation and often different software programs.

LS-DYNA[46], an explicit dynamic code that is ideally suited to solving large deformation, non-linear problems such as sheet metal forming.

Considerable work on finite element sheet metal forming prediction has been undertaken recently. One only has to search the literature to find that in recent years many organizations have adopted finite element analysis (FEA) as part of their design cycle to predict the formability of parts prior to producing tooling. In the work by Harpell [50], FEA was used to predict the limiting draw ratio of aluminum in cylindrical cup drawing. Lamontagne [51] has incorporated plastic anisotropy into sheet metal forming simulations. Recent benchmark studies as part of the Numisheet conference series [52] have examined forming of automotive panels as well as other pressing operations.

The focus of this thesis is not on the finite element method, nor on sheet metal forming predictions using the finite element method. Both of these topics have been covered extensively in prior works, so only the aspects of FEA particular to this research will be discussed, in Chapter 5.

1.3.2 Springback Models

Although explicit time integration codes tend to handle large deformation quite well, they introduce dynamic effects such as oscillation of the panel. These oscillations must be damped out prior to denting using a quasi-static or implicit time integration code such as LS-DYNA version 950 or ABAQUS [53]. This step is known as springback, a procedure used in finite element analysis to allow the residual stresses in the formed part to find static equilibrium without any externally applied loads. The residual stresses may arise from constraints imposed by tooling, or dynamic effects from the forming models. Numerical prediction of springback has been covered in a recent thesis by Zhou [54].

1.3.3 Static Dent Models

The first known example of FEM simulation of static denting was in 1980 by Yutori *et al.* [6] who used FEA to look at strain levels underneath the indentor as the panel was displaced. Their model used only 30 axi-symmetric elements and the indentor was described as a point load.

Following this study, the work of Sakai *et al.* [26] compared finite element stiffness values to those obtained from laboratory panels. They were able to show good correlation between panel stiffnesses in both the primary and secondary stiffness regions; however, convergence issues prevented them from obtaining a residual dent depth after unloading.

As computing power became more available, the size of the models used in static dent resistance computations became larger and more complex. In 1990, Alaniz *et al.* [4] showed the applicability of the finite element method to predict panel stiffness in the secondary and final stiffness regions, but did not incorporate panel forming data in their analysis. The material properties they used were in the as-received condition, which is known to affect accuracy in predicting the secondary and final panel stiffnesses.

Finite element codes have progressed as well. In 1993, Werner [24] compared the results of static dent tests obtained using three different finite element codes, MARC [55], ABAQUS [53] and LS-DYNA [46]. Interestingly, this was the first time a meshed indentor was used instead of a point load at the dent site. It was also the first time a residual dent depth was obtained after unloading of the indentor. Unfortunately, poor correlation with the experimental results was obtained, which may have been due to an insufficiently refined mesh.

In 1994, Montgomery and Brooks [23] performed several finite element analyses on laboratory type panels of varying curvature. They were able to show that for stiffer panels, significant dents can occur at loads slightly greater than oil-canning load shown in Figure 1.1; however, for less stiff panels, the dent initiation load was farther along the secondary stiffness curve.

Sabbagh *et al.* [22] were the first to use FEA to predict static dent depths in actual automotive panels. Two doors were modelled, both considering several dent locations. One of the doors was a complete assembly, including the inner and outer panel, with the mastic modelled as a linear spring. Their work was also the first to include local refinement of the finite element mesh in the denting region in order to gain sufficient resolution. Material stress-strain data for the finite element simulations was obtained from tensile sections cut from existing doors. They were able to establish that FEA was a viable technique to predict the denting characteristics of automotive panels.

Chavali and Song [38] continued the work of Sabbagh *et al.* by using a forming simulation instead of tensile data to account for the initial forming of the door panel. This was the first example of incorporating forming strains from a finite element analysis directly into a subsequent denting analysis.

The work of Raghavan and Arwashan [36] again used forming strains from a forming analysis performed using LS-DYNA. The results of this analysis was subsequently used in a static denting analysis using the LS-NIKE software code. No local mesh refinement was used between the forming and denting steps, as the samples tested were small and could be refined prior to the forming simulation. Interestingly, they concluded that there was a need for better interfaces between implicit and explicit finite element codes to solve complex multi-stage forming problems such as denting.

1.3.4 Dynamic Dent Models

There has been very limited use of the finite element method to predict the dynamic denting characteristics of panels. The first known example was by Ni [40] in 1976. This study considered a finite element model to predict the dynamic denting of a flat rectangular plate subjected to an impulsive load. The predicted dent depths were higher than those measured, which was attributed to the one-point contact used in the model. No springback was modelled; however, it was accounted for by running the simulation long enough to note the range of panel oscillation after impact. This allowed prediction of the dent depth by using the average location of the contact site during oscillation.

Following this work, no examples of dynamic dent prediction using FEA was reported until 1995 when Vreede *et al.* [41] used the method to predict dynamic denting in small, flat laboratory specimens. These specimens were modelled using a simple axi-symmetric element formulation that included strain rate effects for steel. Springback was handled using a technique known as dynamic relaxation. This method applies a carefully selected damping matrix to the system of explicit finite element equations, which eventually allows the system to come to rest. This method has not yet gained acceptance as an accurate way of predicting springback.

The most recent work on dynamic dent prediction using FEA was by Worswick *et al.* [11] in 1997. This study included both static and dynamic dent predictions of panels of varying curvature, size and material. Springback of the dynamic dents was handled using the implicit LS-NIKE software code; however, no comparison to experimental results was made. This study did, however, show that both static and dynamic dent depths have a strong dependence on material strength, thickness, panel size, curvature, support conditions and loading. Most interestingly was the conclusion that static and dynamic denting mechanisms are of a competing nature, such that panels that perform well in static dent tests perform poorly in dynamic dent tests (Figure 1.3 and 1.4). They concluded that high local panel stiffness, which favours static dent performance increases contact forces generated during a dynamic dent to the detriment of dynamic dent performance. Conversely, the same stiffness allowed a higher static load to be carried by the panel prior to a static dent occurring.

1.4 Current Work

The use of initial forming models for subsequent dent predictions is a new concept. Historically, researchers have omitted this step and made simplifications regarding material properties in their finite element dent models. Typically, in order to capture panel pre-strain, a tensile test would be performed on a formed panel; however, this is not possible unless a panel has already been produced. This method does not allow for optimisation of a panel early-on in the design cycle. Only recently have coupled explicit/implicit finite element codes become available, such as LS-DYNA and ABAQUS Explicit/Standard. These codes can simplify the process of transferring data between the various simulations outlined in Figure 1.5; however, there is still a requirement for considerable user intervention between each stage.

The finite element models can capture the forming and springback processes quite well and could be used for a subsequent denting analysis; however, the amount of pre-processing work required to convert one of these models into a subsequent denting model has been prohibitive. This preprocessing typically includes refinement of the finite element mesh in the region to be dented and re-mapping the stress and strain values to the new refined mesh. Positioning of an indentor over the panel finite element mesh is also necessary, as is setting up the initial conditions for the simulation to run. For this reason, one of the goals of this research was the development and validation of a software tool, described in Chapter 2, that could help manage the preprocessing work.

The second major goal of this research was to perform forming experiments followed by static and dynamic denting that could be used to assess or validate the finite element predictions. Chapter 3 describes the material characteristics of the AA5754 and AA6111 aluminum sheet used in these studies. The forming and subsequent denting of these panels is discussed in Chapter 4. Finite element modelling of the complete forming, springback and denting process was undertaken using the commercial finite element codes LS-DYNA and ABAQUS. These finite element models were used to predict panel displacement and dent depths as a function of static loading. Dynamic dent depths were also predicted as a function of indentor velocity. The finite element models are presented in Chapter 5, while the experimental and numerical results are presented in Chapter 6. Discussions of the experimental results and numeric predictions are given in Chapter 7 along with the conclusions drawn from this research.

Chapter 2

D-Mesh Software

2.1 Software Overview

Finite element analysis of the autobody panel stamping process is routinely performed using software such as LS-DYNA [56]. Such forming models can be used in subsequent dent predictions; however, they typically have insufficient refinement in regions where dent resistance studies are performed. Forming models also lack the supporting conditions presented by inner panels which, together with the closure panel make up the panel assembly. The interaction between the inner and closure panel greatly affects the dent resistance characteristics of the autobody closure panel [57].

As a major component of this research, a software program that can locally refine an existing finite element mesh and remap the plastic strain, and stress components to the new mesh has been created. This software program has been entitled D-Mesh. The main input window of D-Mesh is shown in Figure 2.1. Functions were added to the software to minimise the preprocessing work required to set up a finite element dent analysis model. These functions include the ability to place an indentor above the dent location and also to replace adaptive-type constraints with combinations of quadrilateral and triangular meshes.

D-Mesh was programmed using an object oriented approach and the C++

programming language. The Standard Template Library [58] was used to store and manage memory for large amounts of data. The MOTIF [59] libraries were used to provide a standard graphical user interface, that could be ported to any of the UNIX platforms also supporting MOTIF.

2.2 Classes

In object oriented programming, objects are created as a way to group program data with functions that operate on data. This has the effect of encapsulating code, so that it can be used in other programs. It also provides an efficient way to handle large amounts of associated data. In C++, a class refers to a certain type of object that has been defined. This definition includes declaration of the data associated with that type of object and the functions that provide the interface to the data. In the context of C++ programming, data is considered to belong to the class that it was defined in and is known as a property of that class. C++ functions can also belong to a class. The ones that do are known as methods. These methods can only operate on the properties of the class, a typical method known as a *set* type is used to set the value of a certain property. Conversely, a *get* type method is used to return the current value of a property. These two types of methods were written for each of the properties defined in classes of the D-Mesh program. The properties of these classes are outlined in the following sections.

2.2.1 Node Class

The node class is used to define storage space for the node number, coordinate location, boundary conditions and neighbouring element information for a given node in the finite element mesh. Figure 2.2 shows the properties stored within each node object in D-Mesh.

In finite element remeshing software, an element that uses a certain node is known as a neighbour to that node. If the element uses the node as a

Input File Options

File Type

◆ LS-DYNA KEYWORD
◇ LS-NIKE SHORT
◇ LS-NIKE LONG

Options

☐ Read Stresses
☐ Read Adaptivity

Input File Name: hood.in

Line Before Nodes: *NODE
Line After Nodes: $
Line Before Elements: *ELEMENT_SHELL
Line After Elements: $
Line Before Stresses: *INITIAL_STRESS_SHELL
Line After Stresses: $
Line Before Adaptivity: *CONSTRAINED_ADAPTIVITY
Line After Adaptivity: $

Figure 2.1: D-Mesh user interface showing the input window.

```
node
--------------------------------
node_num = 4
x_loc    = 0.5
y_loc    = 0.5
z_loc    = 0.0

vertex_neighbours  = 2,3
midedge_neighbours = 1
```

Figure 2.2: D-Mesh Node Class showing the class properties stored within a typical node.

corner node, then the element is a vertex neighbour. If the element uses the node along an edge, then the element is a mid-edge neighbour to the node. Figure 2.3 shows a finite element mesh containing both vertex and mid-edge neighbours.

Although not necessary, the storage of neighbouring element information with each node greatly speeds up the time taken to search for associated element data when remeshing. As such it was decided to include the element neighbour data along with each node, at the expense of additional memory.

2.2.2 Shell Element Class

Figure 2.4 shows the properties of each shell element in D-Mesh. These properties include the element number, the number of nodes the element contains, the node numbers, thicknesses at each node, an element type identifier and the section number that the element belongs to. Also included is the centroid of the element, number of stress components stored at each integration point, as well as the number of through-thickness points and the number of in-plane integration points. Any number of stress values can be stored for each element. Memory is only allocated for the required amount.

2.2.3 Solid Element Class

Figure 2.5 shows the properties of each solid element read into D-Mesh. Stored within each element is the element number, node connectivity and the section number that the solid belongs to. The use of this class is currently limited to storage of solid indentor elements. As such, no gauss point data is stored with each of these elements, nor can the solid elements be refined.

2.3 External Libraries

When necessary, external programming libraries were used to speed up the code development process. These libraries can be considered to lie outside

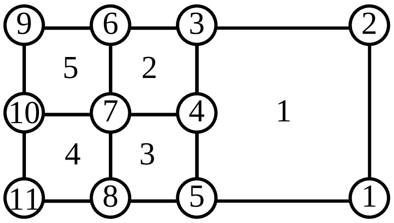

Figure 2.3: Connectivity of some elements showing how element 1 is a vertex neighbour to node 1,2,3 and 5, but also a mid-edge neighbour to node 4.

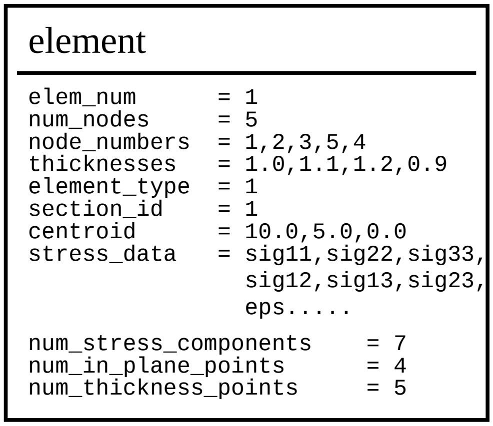

element

```
elem_num      = 1
num_nodes     = 5
node_numbers  = 1,2,3,5,4
thicknesses   = 1.0,1.1,1.2,0.9
element_type  = 1
section_id    = 1
centroid      = 10.0,5.0,0.0
stress_data   = sig11,sig22,sig33,
                sig12,sig13,sig23,
                eps.....

num_stress_components    = 7
num_in_plane_points      = 4
num_thickness_points     = 5
```

Figure 2.4: D-Mesh Element Class showing the class properties stored within a typical element.

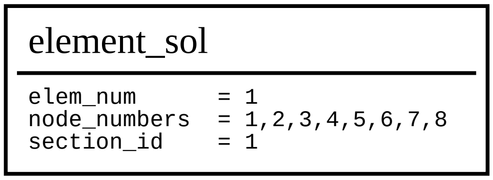

element_sol

```
elem_num      = 1
node_numbers  = 1,2,3,4,5,6,7,8
section_id    = 1
```

Figure 2.5: D-Mesh Solid Element Class showing the class properties stored within a typical element.

of a standard C++ installation and are highlighted here.

2.3.1 Standard Template Library

The Standard Template Library [58], or *STL*, is a library written in C++ for object oriented programming. This library provides a group of classes called containers that are used to hold other objects. An analogy of a very simple container class would be of a FORTRAN array, which can hold only one value in each location of the array, such as integer numbers. The container classes defined in the STL can hold any type of object and automatically manage memory when these objects are inserted and deleted. The obvious benefit of this is the ability to access all of the information associated with an object through the use of only one index. Depending on the type of container used, these objects can be inserted or deleted at any point within the container. Within the context of the STL library, a vector is defined as an STL container that supports random insertion and deletion of objects, as well as automatic memory management. For this reason, the STL vector was chosen as the container class for any objects within D-Mesh that may increase or decrease in number. These objects include the elements and nodes among others. The STL library also provides basic methods and iterators for each of its container classes. The methods provide a means to add and delete objects from within the containers while the iterators can be considered pointers that reference the different objects.

2.3.2 MOTIF Library

MOTIF [59] is an X Windows toolkit that provides the necessary programming tools (called widgets) to easily program a graphical user interface. These widgets include objects such as text boxes, forms, radio buttons, etc. This toolkit was chosen over others as it enables platform-independent coding of the user interface. To date, D-Mesh has been compiled on Silicon Graphics and Linux operating systems using the same code.

2.3.3 Tab Library

The Tab Widget library [60] was downloaded from the internet. It is an addition to the standard set of MOTIF programming widgets that provides the tabbed window look of D-Mesh. This software was made available for free use by Pralay Dakua.

2.4 Program Flow

The D-Mesh program has been structured to allow the user to try different remeshing parameters on the existing finite element mesh without having to re-input data. This is achieved through the use of the MOTIF interface, which retains all of the user supplied data while a given mesh is being processed. After the program has been run once, the output can be examined to determine if the resulting finite element mesh is sufficiently refined. If further refinement is necessary, individual values can be changed to fine-tune the results. The execution process consists of reading in the input file, refinement and remapping stresses within the finite element mesh, approximating original panel curvature, removal of any adaptive constraints, positioning of the indentor and output of the new data files. These sections of the program are discussed further here.

2.4.1 Input Routines

There are three different input file formats supported in D-Mesh. These are LS-NIKE short, LS-NIKE long and LS-DYNA Keyword. The appropriate input file format is selected using the *File Type* radio buttons shown in Figure 2.1. The input file is specified using the *Input File Name* text box. The routine that processes this file only reads in the nodes, shell elements, any adaptive constraints and stress data. This data is stored into two STL vectors, one for the nodes and one for the shell elements. Each section of the input file is parsed using the string data entered in the text boxes below the *Input File Name* text box. The lines before the start of each section of the file must be unique. The default values are for a LS-DYNA Keyword format file. Reading in the stress and adaptive constraint data is activated or deactivated through the use of their associated option buttons.

2.4.2 Element Refinement and Stress Remapping

Figure 2.6 shows the remeshing window of D-Mesh. To refine the mesh, three parameters must be entered. These parameters are the refinement location, refinement radius and the number of refinements.

Figure 2.7 shows how individual elements are refined. One refinement for a quadrilateral shell element consists of subdivision into four smaller quadrilateral shell elements, while one refinement of a triangular element results in three smaller quadrilateral elements. The location of any new mid-edge nodes is calculated to lie halfway between the two vertex nodes lying on the same edge. This is consistent with the position of nodes used in LS-DYNA adaptive constraints. The location of the new node that lies in the center of the old element is calculated as the average of the vertex node positions.

There are two element paving methods used in D-Mesh. The first is shown in Figure 2.8. The refinement location specifies the centroid of a sphere that will encompass all of the elements being refined, while the refinement radius specifies the radius of this sphere. The refinement location can either be given as a node number, or a geometric location in X,Y,Z coordinates. If the centroid of an element lies within the radius of the sphere, the number of refinements it will receive decreases linearly from the center of the sphere to one refinement at the periphery. The value at the center of the sphere is specified using the *Number of Refinements* text box. If the finite element mesh consists of several sections (as in a structural model), individual sections can be omitted from refinement by entering their section identification number in the *Sections to Avoid* text box.

The second element paving method available in D-Mesh uses a target

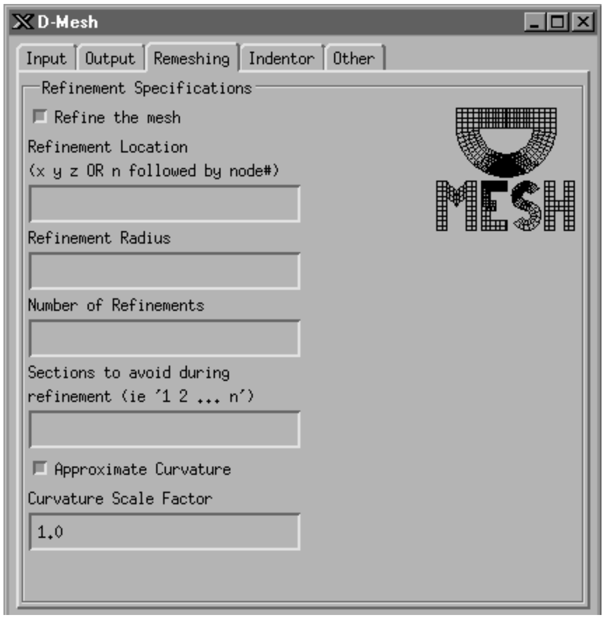

Refinement Specifications

☐ Refine the mesh

Refinement Location
(x y z OR n followed by node#)

Refinement Radius

Number of Refinements

Sections to avoid during
refinement (ie '1 2 ... n')

☐ Approximate Curvature

Curvature Scale Factor
1.0

Figure 2.6: D-Mesh remeshing tab window.

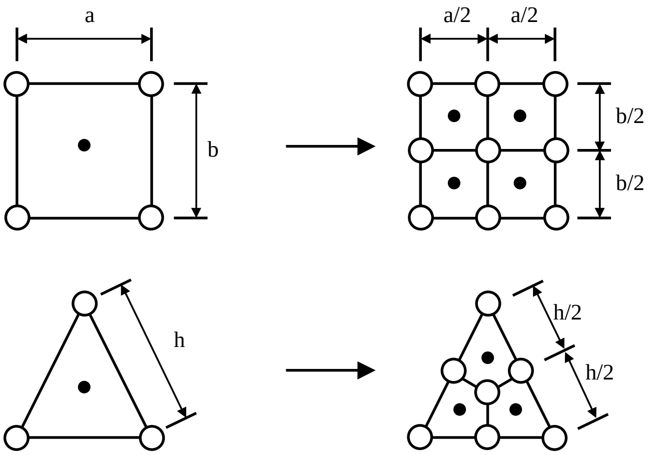

Figure 2.7: Refinement of quadrilateral and triangular shell elements by one level.

area as a means of choosing whether an element will be refined. This option is activated by entering a negative value in the *Number of Refinements* text box. If this value is negative, the magnitude corresponds to a target element area at the refinement location. Elements that are larger than this size will not be refined further. Smooth paving of the element size to the outer refinement radius is achieved through a target area function. This function has two regions, the first is a straight line, the second is a parabolic function. This target area function is plotted in Figure 2.9, the parabolic section is as follows:

$$A_{lt} = \frac{A_l - A_t}{R^2\left(z^2 - 2z + 1\right)} r^2 - \frac{2z\left(A_l - A_t\right)}{R\left(z-1\right)^2} r + \frac{A_l z^2 - 2A_t\left(1 - z\right)}{\left(z-1\right)^2} \tag{2.1}$$

where A_{lt} is the local element target area at any distance (r) from the refinement location. R is the user defined refinement radius and A_t is the target element area. A_l is the area of the largest element that existed in the refinement area prior to refinement. The length of the straight line shown in Figure 2.9 has been set to 0.55 times the refinement radius, 0.55 is also the value of z in the target area equation above. This constant enables a wide refined region that is necessary to capture oil-canning and secondary stiffness during denting. Use of this function has been found to give nicely refined meshes when adaptive elements have been used in the original forming model. An example of remeshing using this function is shown in Figure 2.10.

Remapping of Gauss point data is handled differently depending on the number of shell element in-plane Gauss points used in the input deck. For reduced integration elements, such as in the Belytschko Lin Tsay element [61], [62], there is only one in-plane Gauss point. In these cases, the stress and effective plastic strain values prescribed to each new element are not modified. In non-reduced integration elements, such as those using the Hughes-Liu element formulation [63], there exists four in-plane Gauss points. In this case, each of the in-plane Gauss point data variables is averaged before prescribing the result to the new shell elements.

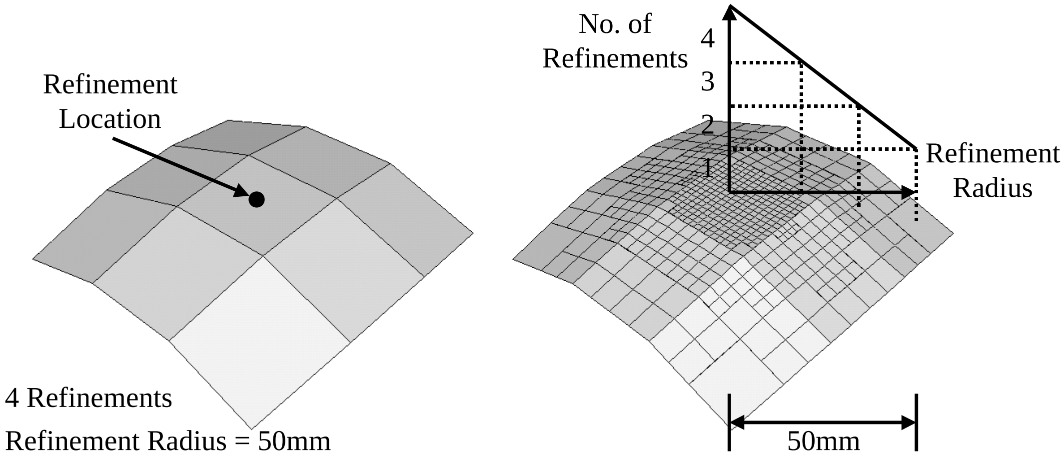

Figure 2.8: Finite element mesh before and after remeshing. 4 refinements were specified within a radius of 50mm.

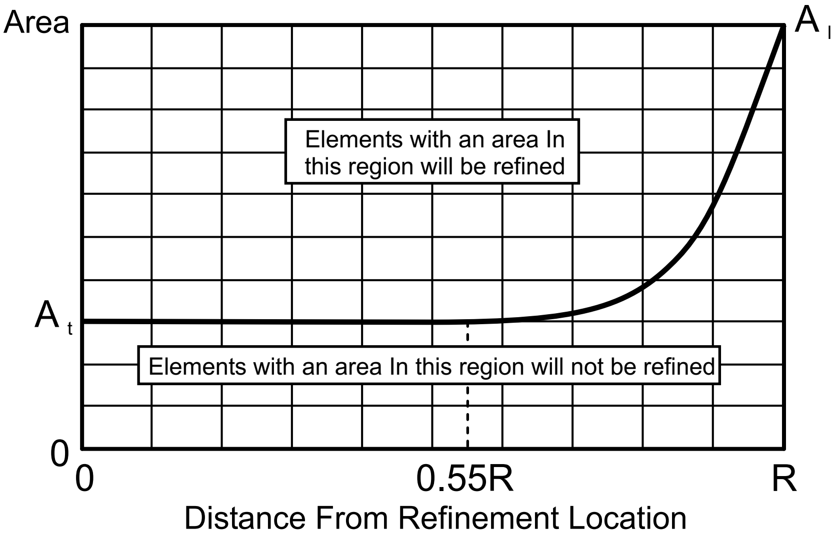

Figure 2.9: This figure shows the area based remeshing function used to determine whether an element will be refined.

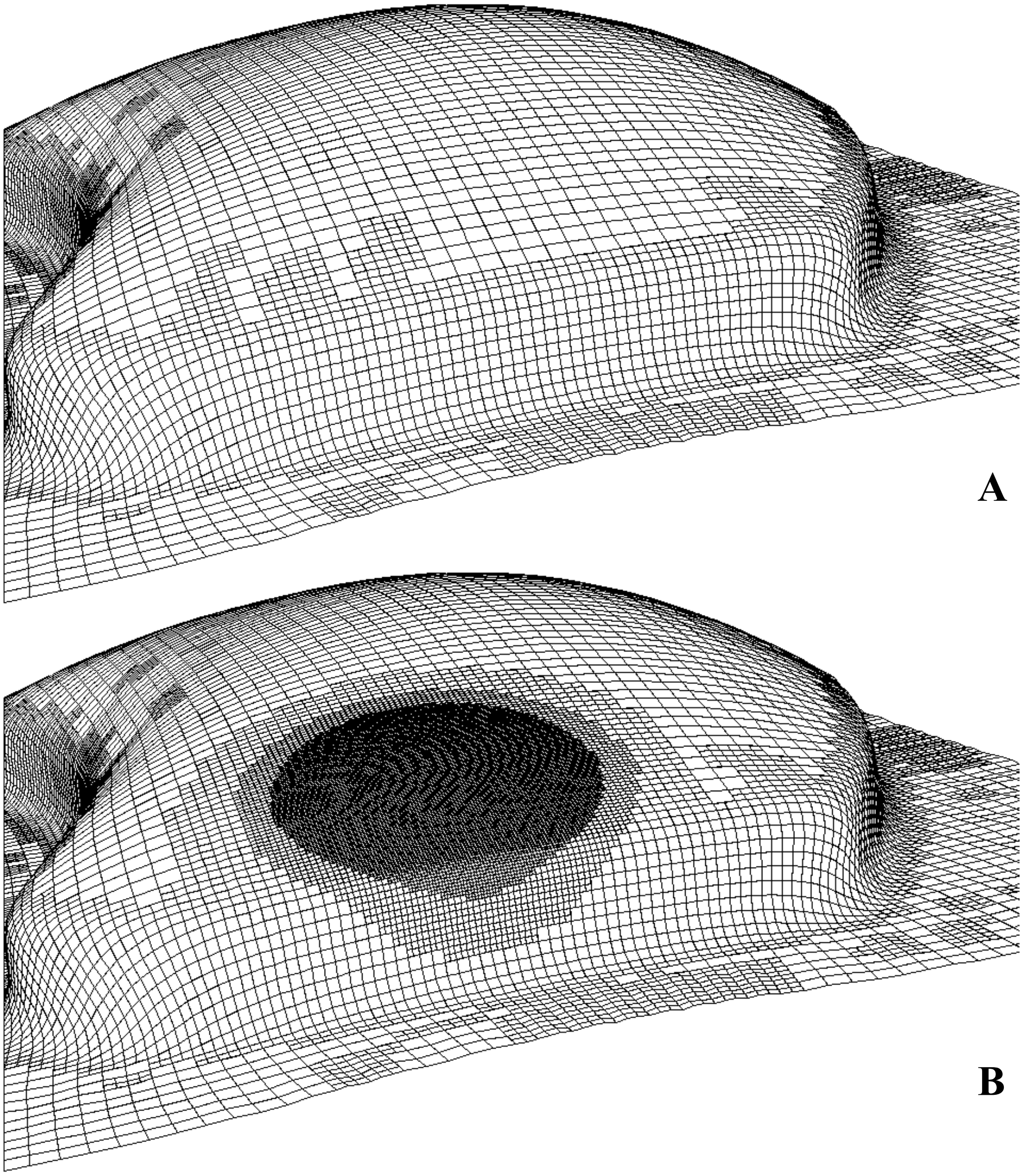

Figure 2.10: A finite element forming model before (a) and after (b) remeshing using the area-based element paving algorithm. Note that the original subdivided elements do not hinder the final mesh when this approach is used.

2.4.3 Panel Curvature Approximation

As local panel curvature is thought to greatly influence panel stiffness and dent resistance, a method of approximating panel curvature during refinement has been implemented in D-Mesh. This method uses bi-cubic hermite f-patches [64, pp 169 - 183] to represent the curved surface of each element as it is refined. The conventional geometric form of this type of surface patch is given in matrix notation as:

$$\mathbf{p}(u,w) = \mathbf{U}\mathbf{M}_F\mathbf{B}\mathbf{M}_F^T\mathbf{W}^T \tag{2.2}$$

where:

$$u, w \in [0,1]$$

$$\mathbf{U} = [\ u^3 \quad u^2 \quad u \quad 1\ ] \tag{2.3}$$

$$\mathbf{W} = [\ w^3 \quad w^2 \quad w \quad 1\ ] \tag{2.4}$$

$$\mathbf{M}_F = \begin{bmatrix} 2 & -2 & 1 & 1 \\ -3 & 3 & -2 & -1 \\ 0 & 0 & 1 & 0 \\ 1 & 0 & 0 & 0 \end{bmatrix} \tag{2.5}$$

and

$$\mathbf{B} = \begin{bmatrix} \mathbf{p}_{00} & \mathbf{p}_{01} & \mathbf{p}^w_{00} & \mathbf{p}^w_{01} \\ \mathbf{p}_{10} & \mathbf{p}_{11} & \mathbf{p}^w_{10} & \mathbf{p}^w_{11} \\ \mathbf{p}^u_{00} & \mathbf{p}^u_{01} & 0 & 0 \\ \mathbf{p}^u_{10} & \mathbf{p}^u_{11} & 0 & 0 \end{bmatrix} \tag{2.6}$$

Note that **B** is actually a 4x3x3 array, with the third dimension having different values for each Cartesian component of (x, y, z). $\mathbf{p}(u,w)$ gives a position vector in cartesian coordinates to a point lying on the patch surface at parametric coordinates (u,w). For a general 4-noded shell element, the local directions of u and w are chosen so that $u = 0$ lies along the element edge pointing from node 1 to 4, while $u = 1$ lies along the edge from node 2 to 3. Similarly, $w = 0$ lies along the element edge pointing from node 1 to

2, while $w = 1$ lies along the edge from node 4 to 3. This local coordinate system is shown in Figure 2.11.

Figure 2.12 shows each component of the $\mathbf{B}$ array. The vectors $\mathbf{p}_{00}$, $\mathbf{p}_{01}$, $\mathbf{p}_{10}$ and $\mathbf{p}_{11}$ point from the origin to the corner nodes of each element. The subscripts of 0 or 1 refer to the local parametric coordinates of u and w. As an example, $\mathbf{p}_{01}$ would mean the position vector pointing to the node at $u = 0$ and $w = 1$. The superscripted vectors of $\mathbf{p}^u_{00}$, $\mathbf{p}^u_{01}$, $\mathbf{p}^u_{10}$ and $\mathbf{p}^u_{11}$ are the surface tangent vectors in the local u direction at each of the four corner nodes, while $\mathbf{p}^w_{00}$, $\mathbf{p}^w_{01}$, $\mathbf{p}^w_{10}$ and $\mathbf{p}^w_{11}$ are the surface tangent vectors in the local w direction. The length of these surface tangent vectors ($\mathbf{p}^\alpha_{ij}$) determines the amount of curvature to be approximated during refinement.

Calculation of the surface tangent vectors $\mathbf{p}^\alpha_{ij}$ begins with an approximation of the average surface normal at each node. In D-Mesh, this is calculated as:

$$\bar{\hat{\mathbf{n}}} = \frac{\sum\limits_{i=1}^{\mathbf{El}_{neighb.}} \hat{\mathbf{n}}_i}{\mathbf{El}_{neighb.}} \tag{2.7}$$

where $\mathbf{El}_{neighb.}$ is the number of element neighbours for the node and $\hat{\mathbf{n}}_i$ is the unit normal calculated at the node using the element neighbour. Figure 2.13 shows how the normal $\mathbf{n}_i$ is calculated for both vertex and mid-edge neighbouring elements. In all calculations, the vectors $\mathbf{V}_1$ and $\mathbf{V}_2$ are ordered so that the resulting cross product, $\mathbf{V}_1 \times \mathbf{V}_2$, gives an outward normal vector $\mathbf{n}_i$ whose direction is consistent with the node connectivity right hand rule. The unit normal for each element is then calculated as:

$$\hat{\mathbf{n}}_i = \frac{\mathbf{n}_i}{|\mathbf{n}_i|} \tag{2.8}$$

Once the average unit normal $\bar{\hat{\mathbf{n}}}$ has been calculated, the surface tangent vectors $\mathbf{p}^\alpha_{ij}$ are calculated as in Figure 2.14 using an intermediate vector $\mathbf{a}$ at each node:

$$\mathbf{a} = \mathbf{e}_\alpha \times \bar{\hat{\mathbf{n}}} \tag{2.9}$$

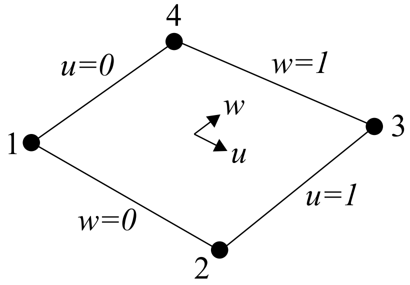

Figure 2.11: Shell element parametric coordinate system convention.

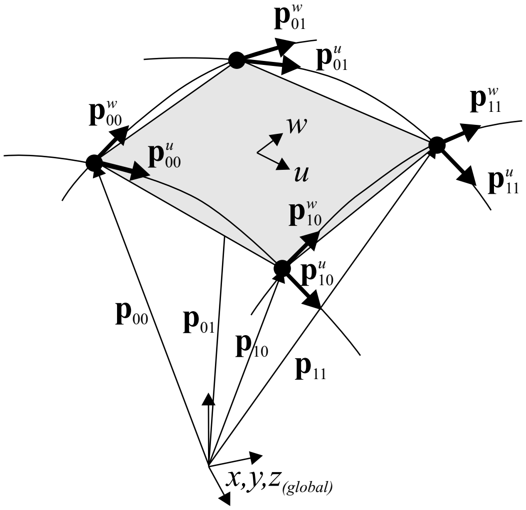

Figure 2.12: P-Vectors that are used to generate the bi-cubic hermite f-patch B matrix for each element.

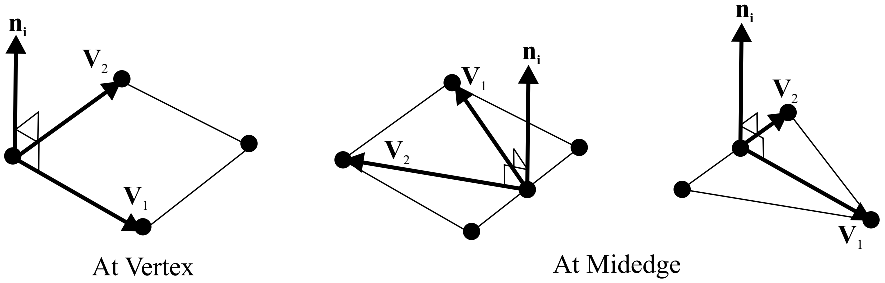

Figure 2.13: Shell element normal calculation at a vertex node and a mid-edge node.

where $\mathbf{e}_\alpha$ is a vector lying along the element edge that coincides with the surface tangent vector being calculated. In this example, the $\mathbf{p}^u_{00}$ vector is calculated using:

$$\mathbf{p}^u_{00} = \bar{\hat{\mathbf{n}}} \times \mathbf{a} \tag{2.10}$$

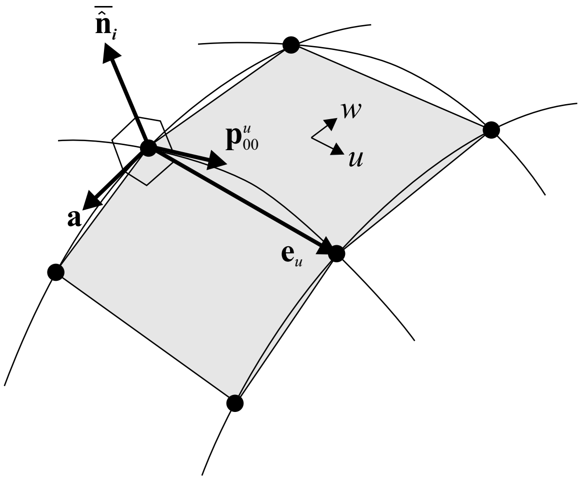

Figure 2.14: Surface tangent calculation at the corner node of a quadrilateral shell.

Triangular elements require special treatment for the surface tangent vectors of $\mathbf{p}^u_{01}$ and $\mathbf{p}^u_{11}$. In this case there is no edge vector $\mathbf{e}_\alpha$ since by convention nodes 3 and 4 of the shell element are coincident. For this case only, $\mathbf{p}_{01}^{u}$ and $\mathbf{p}_{11}^{u}$ are equal and approximated using a vector created between two points lying $1/10^{th}$ of the distance along the element edges as shown in Figure 2.15. This allows equations [2.2] through [2.6] to be used for 3 points instead of the usual four.

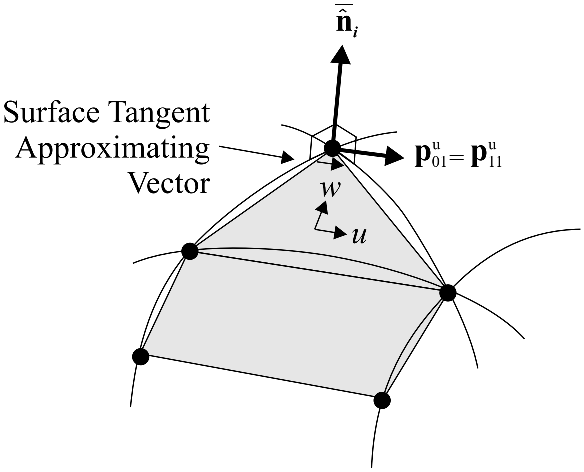

Figure 2.15: Surface tangent of a triangular shell at a corner node

Required input for this function is a value for the curvature scale factor, λ which is entered on the *remeshing* tab (Figure 2.6). This value can range from zero for no curvature to the default value of one. This value scales the length of the surface in-plane tangent vectors $\mathbf{p}_{ij}^{\alpha}$ from zero to the length of the element edge that the in-plane tangent vector corresponds to ($\mathbf{e}_{\alpha}$). Values greater than 1.0 should be avoided, as an erroneous surface will result.

A typical result of the bi-cubic hermite approximation is shown in Figure 2.16. The advantage of this method is that the original nodes lie on the surface and the surface in-plane and normal vectors are also matched at each original node. This has the effect of creating a smooth and continuous surface within the region being refined. If curvature is being approximated, the position of any new nodes created during the refinement step are moved to lie on the surface.

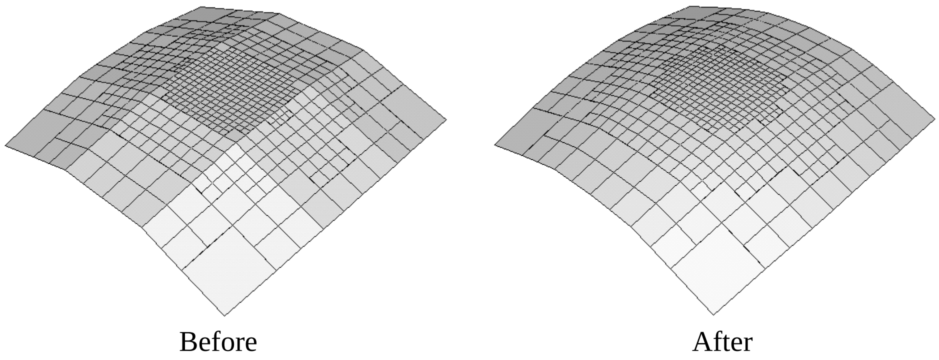

Figure 2.16: Finite element mesh before and after curvature approximation using Bi-Cubic Hermite F-Patches.

2.4.4 Removal of Mid-Edge Nodes

In Figure 2.3, node 4 is a mid-edge node. Adaptive constraints are used during sheet metal forming simulations to constrain these mid-edge nodes to remain at the element mid-edge during the forming simulation. The presence of these adaptive constraints was thought to hinder convergence of both springback and static dent simulations in LS-NIKE. This prompted the addition of a function that would take an existing finite element mesh with mid-edge nodes and replace them with combinations of smaller triangular and quadrilateral shell elements. This function is activated by selecting the *Remove Adaptivity* option button on the *Other Options* tab. Figure 2.17 shows the resulting elements created to replace any original elements containing mid-edge nodes. Any elements that contain these nodes are subdivided in such a way that the use of triangular elements is minimised.

2.4.5 Indentor Positioning

Currently there are three types of indentors commonly used in the automotive industry for panel dent resistance and stiffness tests. As an aid in streamlining the setup of denting simulations, a method of inserting these indentors into the output mesh has been implemented.

Figure 2.18 shows the D-Mesh tab window related to indentor input and positioning. This window allows the user to specify the indentor and how it will be positioned within the output mesh. As a separate input file is used, any shape of indentor may be used. The only restrictions are that the file must be in LS-DYNA Keyword format and solid brick elements must be used. Required input is the indentor file name, as well as strings to parse out the nodes and solid elements from the input file. The *New Indentor Location* text box allows the user to specify a node that the indentor will be positioned above. The indentor is rotated and translated so that its local z axis lies along the average outward normal ($\bar{\hat{\mathbf{n}}}$) of the surface calculated at the node. This normal is calculated as in Equation (2.7). The local x-direction of the indentor is rotated to lie in the plane created by the outward normal $\bar{\hat{\mathbf{n}}}$ and an element edge vector $\mathbf{e}$. The element chosen for the edge vector is the lowest numbered element, while the edge is chosen by the right handed node numbering rule. The distance away from the surface is specified using the *Distance From Node* text box, to which half of the shell thickness can be added. The loading direction can be reversed using the *Flip Indentor Side* option button. The nodes of the indentor can be renumbered using the *Renumber Indentor Nodes* option. This option requires that the new starting number for the nodes be entered in the *New Starting Number* text box. If the value entered is less than the maximum node number after remeshing, consecutively renumbered nodes will be output. An example of indentor positioning is shown in Figure 2.19.

2.4.6 Output Routines

Two output files are created during refinement. The first is a text file that is used as input for subsequent denting analysis. One of four different output file formats can be chosen, they are LS-NIKE short, LS-NIKE long, LS-DYNA Keyword and ABAQUS Standard. The appropriate file format is selected using the *File Type* radio buttons shown in Figure 2.20. The *Output File Name* text box can be used to change the default output filename.

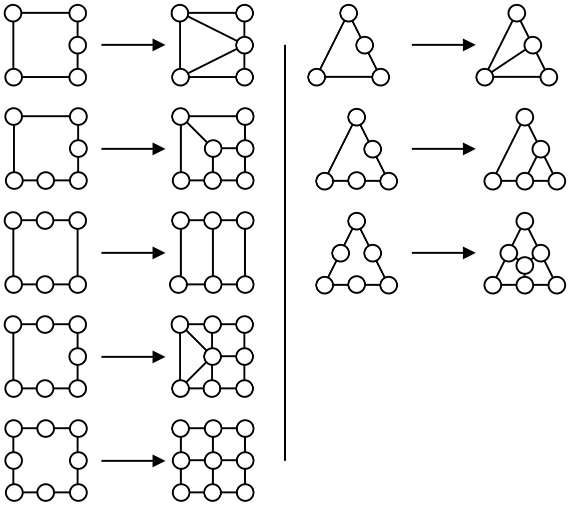

Figure 2.17: Shell element mid-edge node removal rules for each possible combination of nodes.

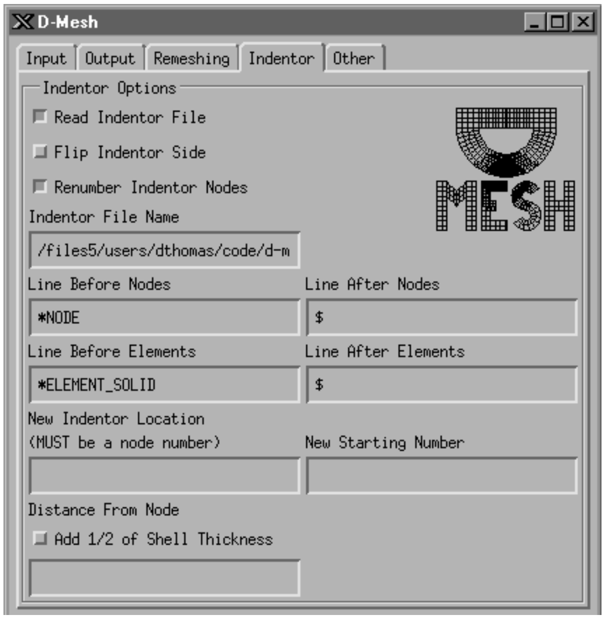

Indentor Options

☑ Read Indentor File

☐ Flip Indentor Side

☑ Renumber Indentor Nodes

Indentor File Name: /files5/users/dthomas/code/d-m

Line Before Nodes: *NODE

Line After Nodes: $

Line Before Elements: *ELEMENT_SOLID

Line After Elements: $

New Indentor Location (MUST be a node number):

New Starting Number:

Distance From Node

☐ Add 1/2 of Shell Thickness

Figure 2.18: D-Mesh indentor tab window.

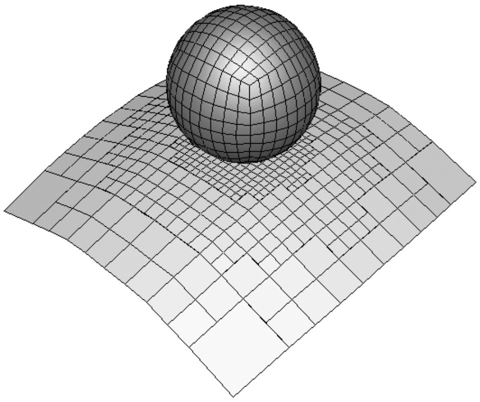

Figure 2.19: Positioning of a 25.4mm solid element indentor normal to the surface to be dented.

The second output file is a LS-TAURUS Data Base file [65] that contains data that can only be viewed using commercial viewers such as LS-POST [66]. This file is written in a proprietary format used mainly by the LS-DYNA software. The name of this file can be changed by modifying the *D3Plot File Name* text box. This binary database file should be used in conjunction with d3plot file viewers such as LS-POST to verify that the results of mesh refinement are acceptable.

In the current work LS-DYNA Keyword is the preferred output method for a dynamic dent analysis while ABAQUS Standard is preferred for a static dent. For an ABAQUS Standard output file, element stress values are written to a separate file entitled “stresses.inp”. This is necessary as current versions of ABAQUS are limited to allow initialisation of shell element stress values at only one location if the standard input file method is used. For shell elements this is insufficient as bending stresses cause significant differences in stress values through the shell thickness. In order to initialise all of the stress values, the ABAQUS user subroutines SIGINI and HARDINI [67, 25.2.11, 25.2.17] must be used. These input routines require that the initial stress values be in a local coordinate system for each shell element, so the element stress components are first rotated from the global to the local coordinate

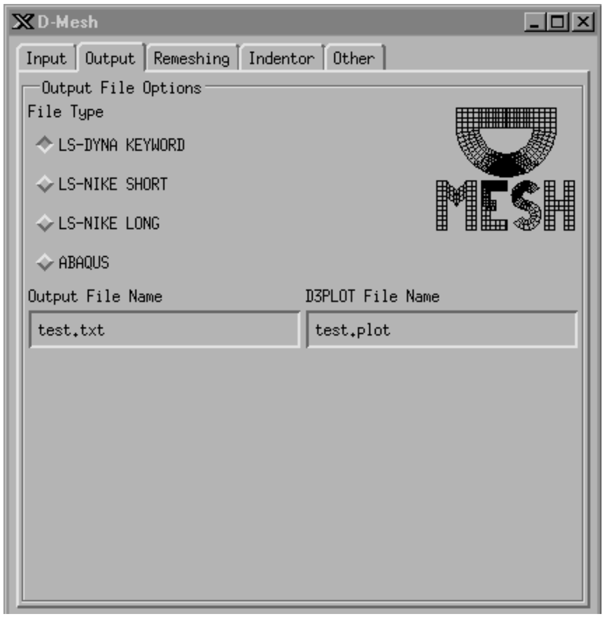

Output File Options

File Type

◇ LS-DYNA KEYWORD

◇ LS-NIKE SHORT

◇ LS-NIKE LONG

◇ ABAQUS

Output File Name: test.txt

D3PLOT File Name: test.plot

Figure 2.20: D-Mesh output tab window.

system using:

$$\sigma_{uw(local)} = \mathbf{a}_{ui}\mathbf{a}_{wj}\sigma_{ij(global)} \tag{2.11}$$

where:

$$u, w \ \& \ i, j = (1, 2, 3)$$

In Equation (2.11), $\mathbf{a}_{ij}$ represents a rotation tensor from the global Cartesian coordinate system to the local system. The individual components can be obtained from a unit triad located at each shell element centroid. This triad is formed using the same convention as in ABAQUS [53, 3.6.3], whereby the shell normal acts as the 3^{rd} local coordinate direction, while the 2^{nd} local coordinate is calculated using a cross product of the shell normal and the global x-axis. The exception to this rule is that if the x component of the shell normal lies within 0.1° of the global x-axis then the 2^{nd} local coordinate is calculated using a cross product of the normal and the global z-axis. The

1^{st} coordinate direction is then calculated using the cross product of the 2^{nd} with the 3^{rd}.

Once the local unit triad is known, the individual components of a tensor that rotates from a local to a global coordinate system is obtained from the direction cosines of the local unit triad. ie:

$$\mathbf{a}_{ij} = \begin{bmatrix} a_{11} & a_{12} & a_{13} \\ a_{21} & a_{22} & a_{23} \\ a_{31} & a_{32} & a_{33} \end{bmatrix} \tag{2.12}$$

in which the terms $\mathbf{a}_{ij}$ represent the direction cosines of the i^{th} principal directions.

The results of using this stress rotation have shown good agreement with the thin shell element stress condition that $\sigma_{zz} = 0$ when stress values were rotated from an LS-DYNA input deck to the local coordinate system used within ABAQUS. This was tested on the three main element formulations used for sheet metal forming, namely the Belytschko Lin Tsay element formulation, Hughes-Liu element formulation and element 16 [68] formulation. Slight errors can occur in the output for warped elements; however, so care should be taken to ensure that a well refined mesh is being used.

Chapter 3

Materials Tested

3.1 Material Selection

There are several aluminum alloys that have been developed for use in automotive body panels. Of these, AA6111, AA6016, AA5754 and AA5182 are commonly used. Candidate materials for outer or closure panels are AA6111 and AA6016, which are heat-treatable alloys with higher yield strengths for dent resistance. Typically, these alloys are formed in the T4 or unaged temper and then harden to a T8X condition during the paint bake cycle. Inner panels are fabricated from either AA5754 or AA5182, which are work-hardening alloys. AA5754 tends to have lower formability than AA5182, but is less expensive.

A typical automotive paint bake process consists of three heat cycles, to cure the electro-galvanizing coat, primer paint and top/clear coat paint applications. These cycles last 15-25 minutes each at 170 - 185°C, 160 - 170°C and 130 - 150°C, respectively. Lloyd [69] has stated that in laboratory tests considering AA6111, these three cycles can be condensed into a single representative 32 minute heat treatment cycle at 177°C. This single heat treatment cycle achieves the same yield strength increase in AA6111 because the panels do not have to heat up and cool three times as in the automotive paint bake process. Several variants of AA6111 undergo pre-treatments to obtain the maximum possible yield strength increase during an automotive paint bake process [69]. This pre-treatment does not affect the yield strength in the T4 condition which is good for formability, but does promote higher hardening rates during the paint bake cycle.

Two aluminum alloys, AA6111 and AA5754, were made available by ALCAN International Limited for use in this study. Three thicknesses of AA6111 were supplied, 0.81mm, 0.93mm and 1.00mm. The sheets were unaged, but pre-treated and were in the T4PD condition (a proprietary T4-variant with an optimised paint-bake response). Two gauges of 1.0mm and 1.6mm thick AA5754 were also supplied. The AA5754 was unstrained, or in the O-temper annealed condition. The 1.6mm thick AA5754 sheet was not used; however, as initial dent tests revealed that the panels were too strong to obtain dents at the loads considered. The 1.0mm AA5754 sheet used for this study was sheared from ALCAN coil number 12918117, the coil numbers of the AA6111 sheets were unknown.

3.2 Material Characterisation

The mechanical properties of the two aluminum alloys (AA6111 and AA5754) were determined at the ALCAN International Kingston Research and Development Center (KRDC). An Instron 4200 Series IX robotic tensile testing machine was used to test each sample, as shown in Figure 3.1. This tensile testing machine was configured to take three initial thickness and width measurements of each tensile test specimen. Each specimen was then mounted in the Instron apparatus and two extensometers were affixed as shown in Figure 3.2. The extensometers measured the axial and transverse extensions as the tensile test was performed. The load was measured during the tensile test using a 97 KN capacity Instron load cell.

Rolled sheet metal typically exhibits anisotropy due to the plastic work done on the sheet. During rolling, the individual grains within the metal tend to become elongated in the rolling direction and the distribution of

Figure 3.1: Automated tensile testing robot used at ALCAN KRDC.

slip plane orientations within each grain becomes less random. This texture creates differences in material yield strength and ductility when measured at various angles relative to the rolling direction (See Schey [70, p260]). This texture is often manifest in directional differences in the Lankford Coefficient, a measure of sheet anisotropy attributed to Lankford *et al.* [71] and given by:

$$R = \frac{\epsilon_w}{\epsilon_t} \tag{3.1}$$

where R is the Lankford Coefficient, commonly referred to as the R-value. The width and thickness strains (ϵ_w, ϵ_t) are obtained from the uniaxial tension tests.

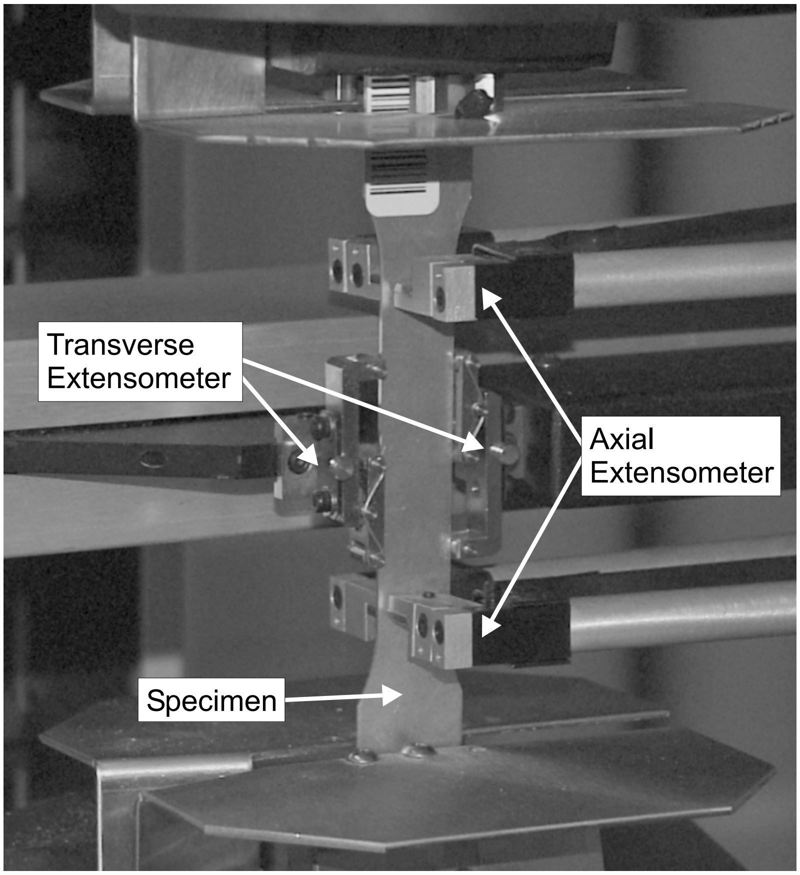

Figure 3.2: Axial and transverse extensometers affixed to a tensile specimen prior to testing

In order to quantify the yield strengths and Lankford Coefficients of each material, the tensile tests summarised in Table 3.1 were performed. A total of 39 tensile specimens were cut for each sheet thickness to the specifications shown in Figure 3.3. Twelve specimens were cut at each angle of 0°, 45° and 90° to the rolling direction. Six samples at each angle were then tested prior to heat treatment and six were tested following heat treatment. In addition, three AA6111 specimens were cut from a formed and paint baked panel for each gauge. This provided measured values of the yield strength increase achieved through forming and paint baking for comparison with the finite element forming model predictions. Tensile tests were also performed on the 1.0mm AA5754 sheet in both the unstrained and strained condition. For this work, the value of Young's Modulus that was used for the aluminum was 70GPa, while Poisson's ratio was 0.33, as taken from handbook data [72]. The Lankford Coefficients (R00, R45 and R90) were calculated at ten percent true strain. The stress-strain curves and R-values were used in the FEM models as described in Chapter 5.

Table 3.1: A listing of the tensile tests performed on the aluminum sheet. PB - Paint Baked, RD - Rolling Direction, F - Strained During Panel Forming

Material	Condition	Gauge [mm]	at 0°	at 45°	at 90°
5754	O	1.05	6	6	6
5754	F	1.05	3		
6111	T4	0.81	6	6	6
6111	T4	0.93	6	6	6
6111	T4	1.00	6	6	6
6111	PB	0.81	6	6	6
6111	PB	0.93	6	6	6
6111	PB	1.00	6	6	6
6111	PB,F	0.81	3		
6111	PB,F	0.93	3		
6111	PB,F	1.00	3		

The results of the tensile tests are summarised in Table 3.2, with the true yield stress versus effective plastic strain curves shown in Figures 3.4 to 3.7. The material stress-strain curves that were used during forming simulations were all taken from regression analyses that fit the following fifth order polynomial to the rolling direction true yield strength curves.

$$\bar{\sigma} = A\bar{\epsilon}^5 + B\bar{\epsilon}^4 + C\bar{\epsilon}^3 + D\bar{\epsilon}^2 + E\bar{\epsilon} + F \tag{3.2}$$

In Equation 3.2, $\bar{\sigma}$ is the effective true yield stress, $\bar{\epsilon}$ is the effective plastic strain and A, B, C, D, E and F are coefficients determined from the regression

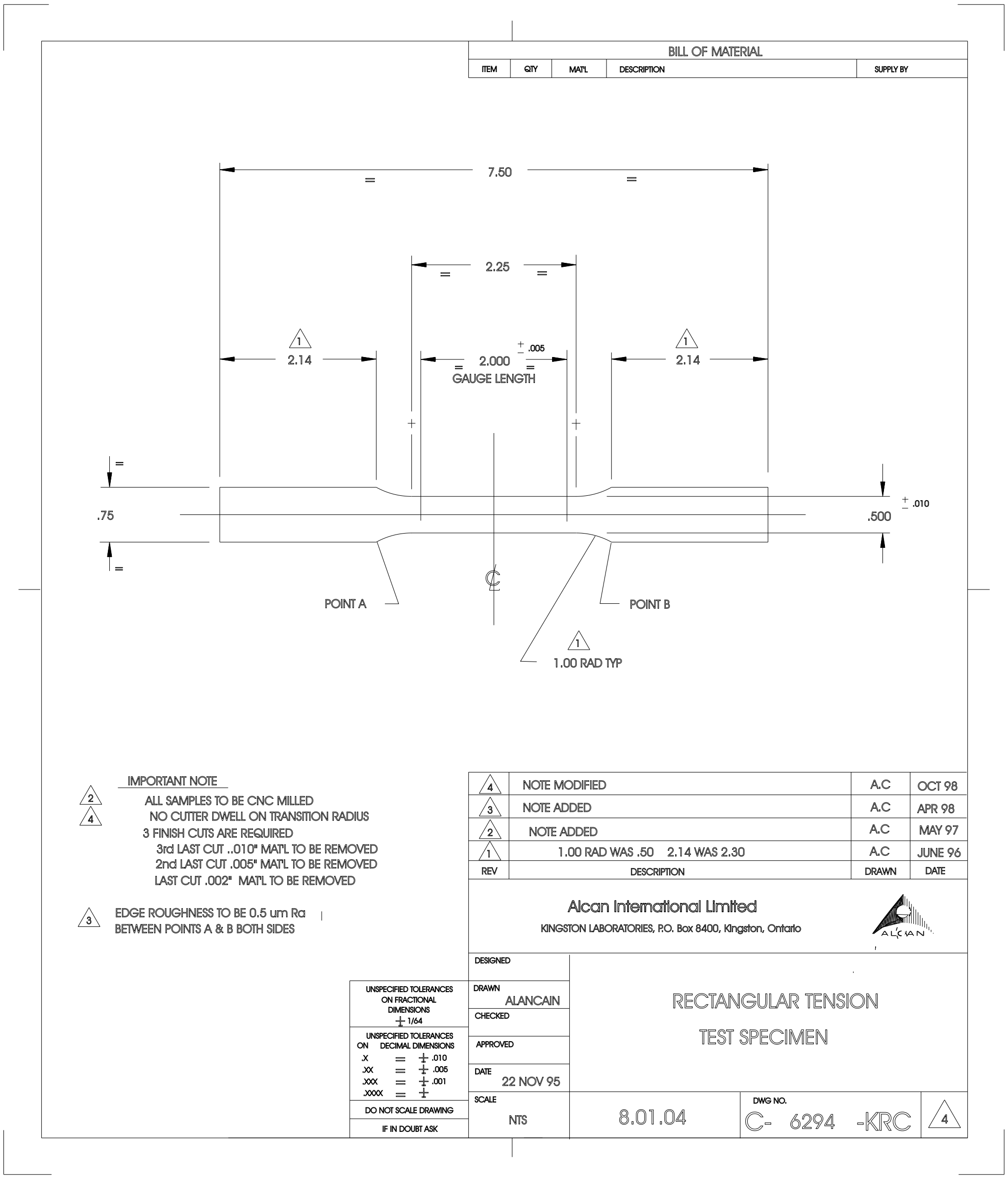

Figure 3.3: Drawing of tensile test specimen required for use with the robotic tensile tests at KRDC.

analysis. The values of these coefficients are given in Table 3.3, while the resulting curves are shown in Figures 3.4 to 3.7. During forming operations, strains can reach values considerably higher than those measurable during a tensile test. To approximate the material behaviour at the higher strains, a constant work hardening rate was assumed. This allowed the final work hardening rates for each material to be approximated as the average rate during the final 2% strain recorded for each tensile test.

Table 3.2: Results of the tensile tests performed on the aluminum sheet. PB - Paint Baked, RD - Rolling Direction, F - Strained During Panel Forming

Material	Condition	Gauge [mm]	σ_y [MPa]	R00	R45	R90
5754	O	1.05	101	0.64	0.75	0.77
5754	F	1.05	152	0.77		
6111	T4	0.81	140	0.62	0.66	0.86
6111	T4	0.93	158	0.68	0.54	0.54
6111	T4	1.00	140	0.60	0.71	0.62
6111	PB	0.81	222	0.61	0.66	0.87
6111	PB	0.93	215	0.68	0.55	0.55
6111	PB	1.00	215	0.59	0.68	0.63
6111	PB,F	0.81	258	0.65		
6111	PB,F	0.93	253	0.69		
6111	PB,F	1.00	252	0.62		

Table 3.2 highlights the differences in final yield strengths of the AA5754 and AA6111 sheet. The AA5754 sheet has an initial yield strength of 101MPa in the O-temper annealed condition. Work hardening this material by only 2-3% strain, which is typical of strain levels in closure panels, increases the yield strength to 150MPa. This is a 50% increase in strength. The initial yield strength of 140MPa for the AA6111 sheet is considerably higher than the initial AA5754 yield strength. By paint baking the AA6111 sheet, a further increase to 215MPa is realised. The combination of pre-strain and paint bake leads to a final yield strength of 253 MPa. Thus, the AA6111 sheet

Table 3.3: Listing of the coefficients that resulted from the regression analysis of the tensile material data. PB - Paint Baked, RD - Rolling Direction, F - Strained During Panel Forming

Material	**Yield Strength Coefficient**					
	A	B	C	D	E	F
5754-O, 1.05mm	1113511	-674531	172952	-26398	2903	101
6111-T4, 0.81mm	603652	-376164	103805	-18477	2596	140
6111-T4, 0.93mm	664284	-424787	114182	-18923	2568	158
6111-T4, 1.00mm	706940	-440602	118062	-19734	2618	140
6111-PB, 0.81mm	2072015	-981266	188695	-22164	2401	222
6111-PB, 0.93mm	2116174	-991991	188173	-21884	2407	215
6111-PB, 1.00mm	2848011	-1331566	248236	-26801	2545	215
6111-PB&F, 0.81mm	6008427	-2431145	379395	-32429	2471	258

has the largest final yield strength, which provides greater dent resistant than AA5754.

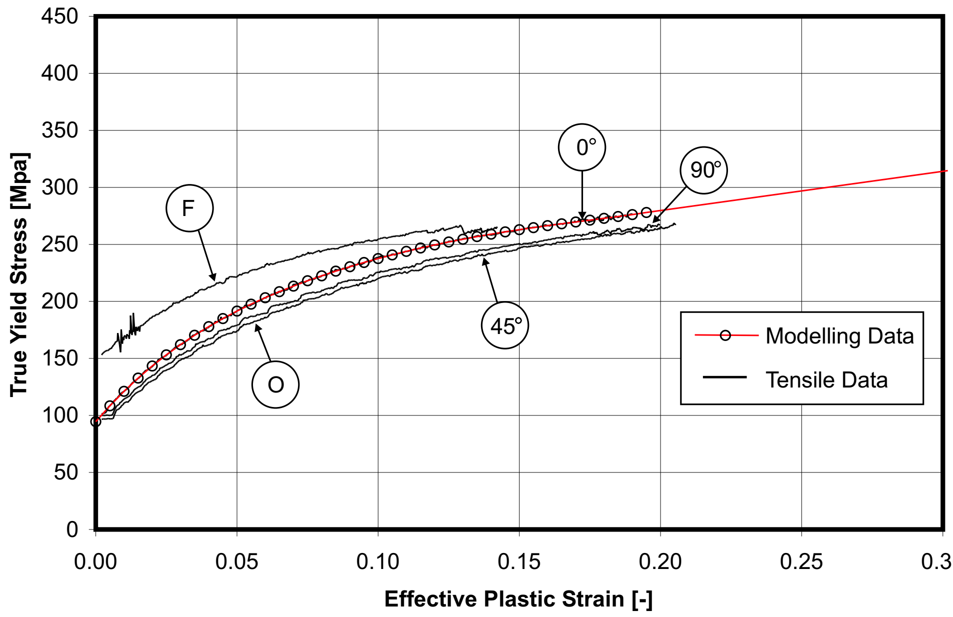

Figure 3.4: AA5754-O true stress versus effective plastic strain curves showing the slight differences in yield strength when tensile specimens are pulled at in-plane orientations of 0° 45° and 90° to the rolling direction. The data points used within the finite element models are shown as circles, these points correspond to the rolling direction. The curve from the formed panels is also shown.

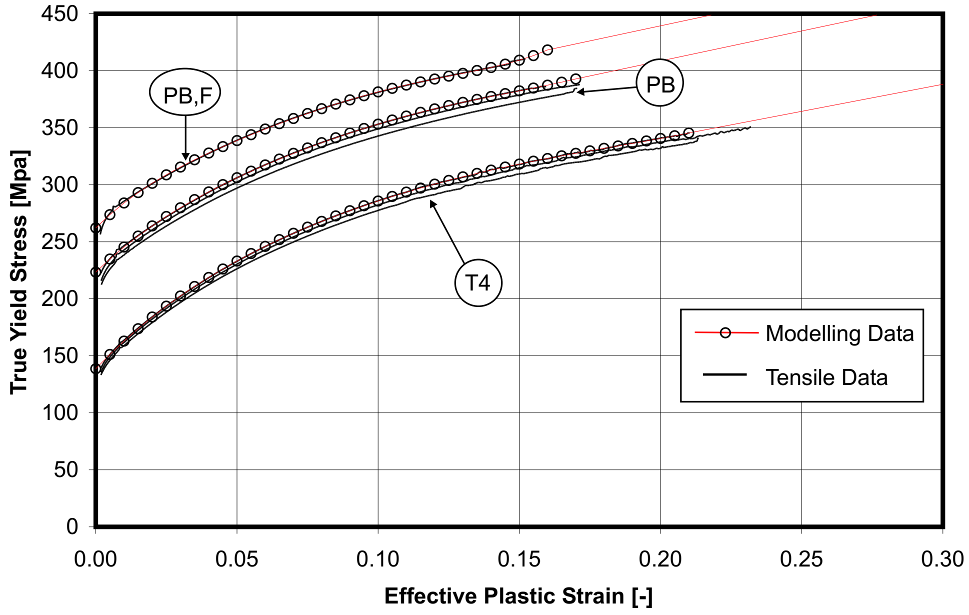

Figure 3.5: AA6111 0.81mm true stress versus effective plastic strain curves showing the yield strength increase due to paint bake (PB) heat treatment over the as-received (T4) condition. Each curve represents an average of the tensile tests performed at 0° 45° and 90° to the rolling direction. The data points used within the finite element models are shown as circles, these points correspond to the rolling direction. The curve from the formed and paint baked (PB,F) panels is also shown.

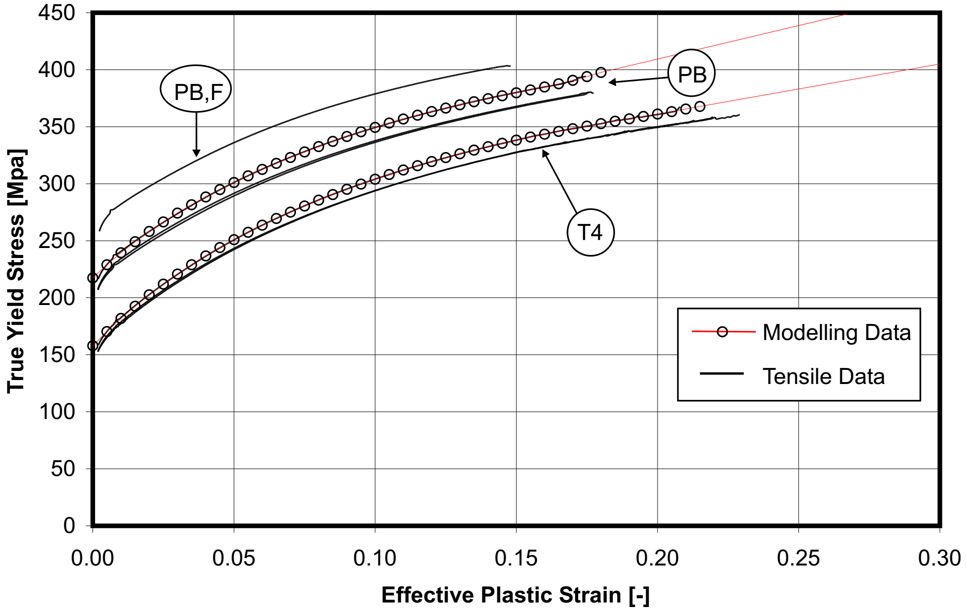

Figure 3.6: AA6111 0.93mm true stress versus effective plastic strain curves showing the yield strength increase due to paint bake (PB) heat treatment over the as-received (T4) condition. Each curve represents an average of the tensile tests performed at 0° 45° and 90° to the rolling direction. The data points used within the finite element models are shown as circles, these points correspond to the rolling direction. The curve from the formed and paint baked (PB,F) panels is also shown.

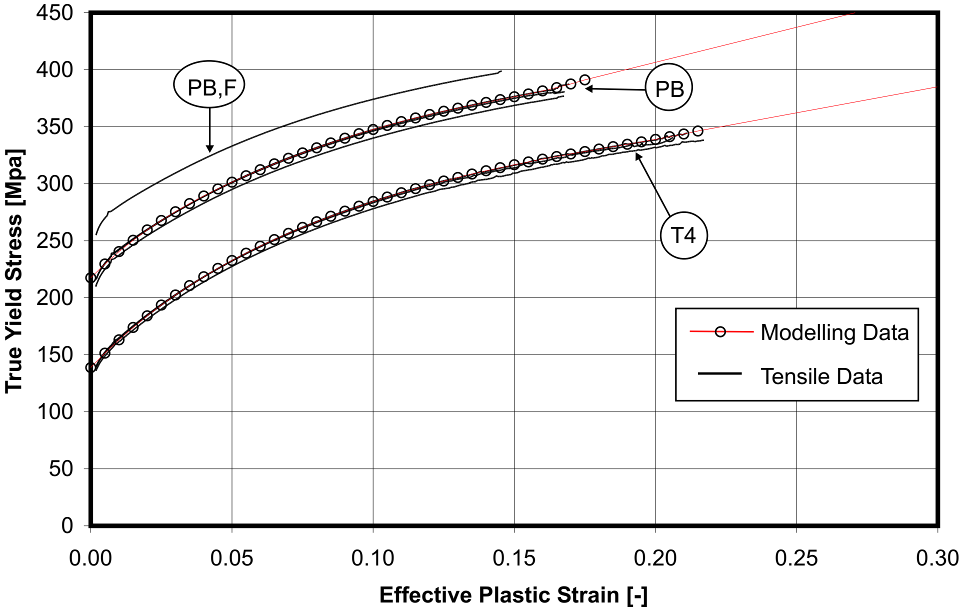

Figure 3.7: AA6111 1.0mm true stress versus effective plastic strain curves showing the yield strength increase due to paint bake (PB) heat treatment over the as-received (T4) condition. Each curve represents an average of the tensile tests performed at 0° 45° and 90° to the rolling direction. The data points used within the finite element models are shown as circles, these points correspond to the rolling direction. The curve from the formed and paint baked (PB,F) panels is also shown.

Chapter 4

Experimental Procedures

In order to perform dent resistance experiments, a tooling set of sufficient size to represent commercial closure panels was chosen. The formed panel, shown in Figure 4.1, was fabricated using tooling available at the Industrial Research and Development Institute (IRDI) in Midland, Ontario. The panels were stamped using both AA5754-O and AA6111-T4 sheet. The top or crown of these panels has a swept surface which affords differences in curvature and local stiffness from one location to the next. The curvature of the panel at different cross sections was estimated using calculations based on the original CAD surfaces of the tooling and is shown in Figure 4.2. Using these curvatures as a guide, both static and dynamic dent tests were performed at locations that would provide a range in local panel stiffness. The AA5754-O panels were statically dented at locations A through E, shown in Figure 4.2 and dynamically dented at locations A through C only. The AA6111 panels were statically and dynamically dented at locations A through C.

4.1 Panel Stamping

The deep drawing press used to stamp the panels was located at the Industrial Research and Development Institute (IRDI) in Midland, Ontario. This press, shown in Figure 4.3, has a moving platen and stationary punch.

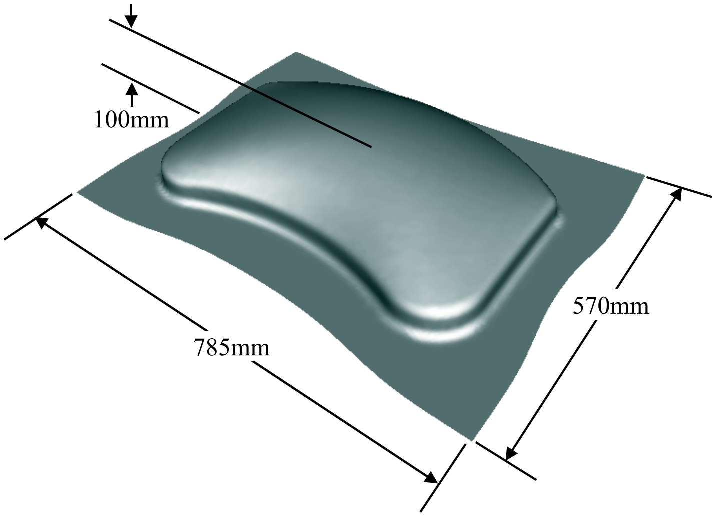

Figure 4.1: Sketch of the IRDI panel adopted in the current research, showing the draw depth and initial length and width.

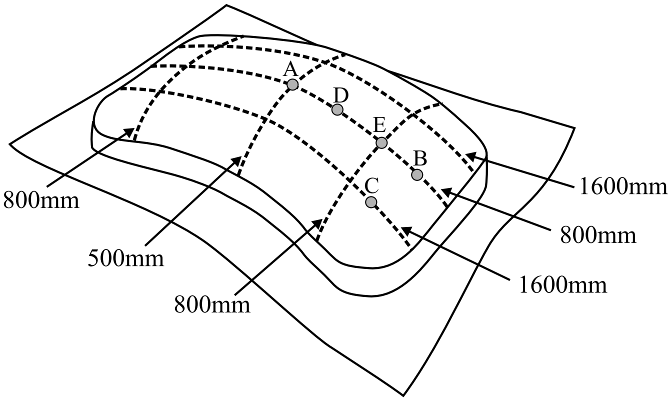

Figure 4.2: Radius of curvature of the IRDI panel at six different cross sections. These values were estimated by fitting a circular arc to three points along each of the dotted paths shown. Dent locations A through E are also shown.

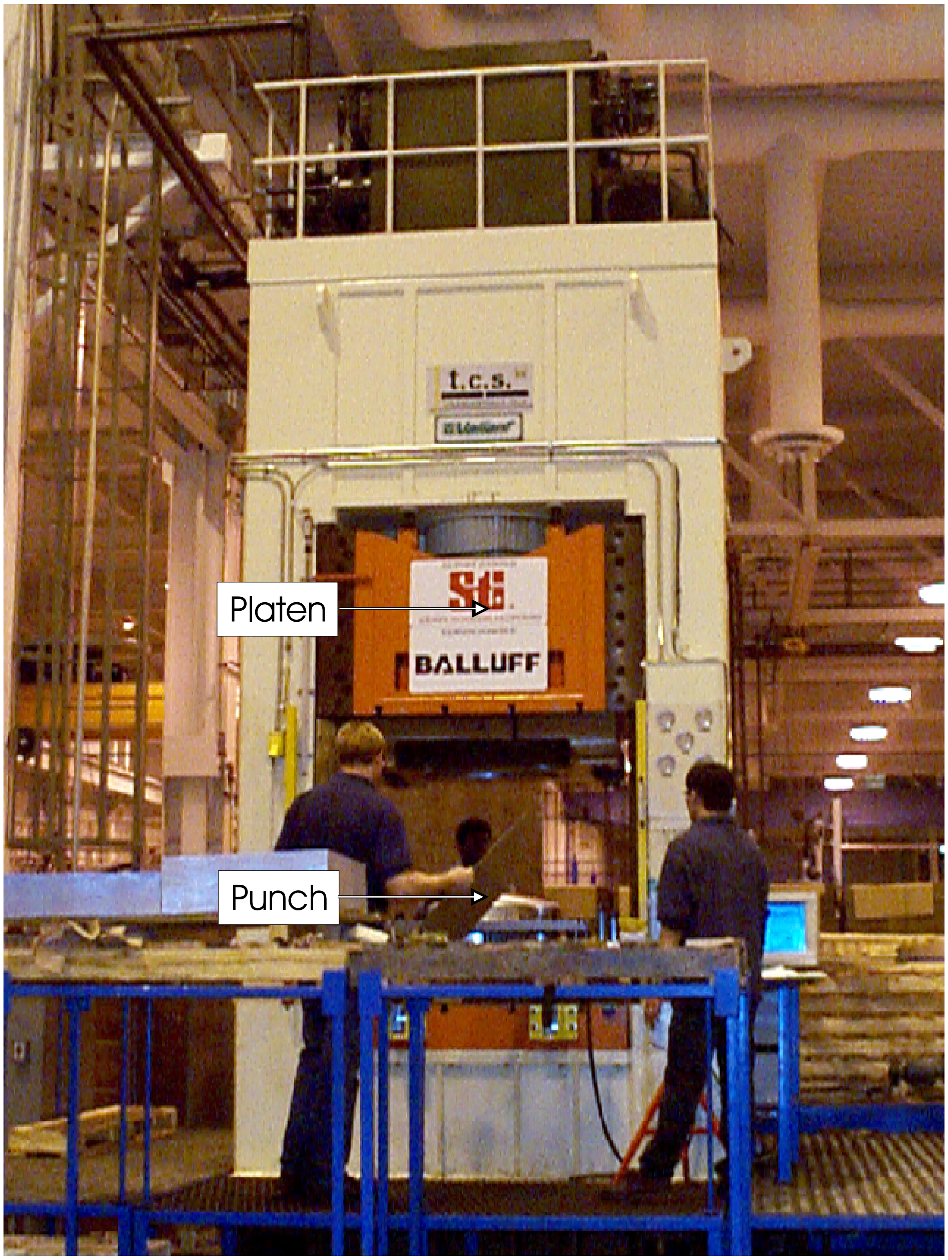

Figure 4.3: 1333 kN IRDI Press that was used to stamp the panels of AA5754-O and AA6111-T4 sheet.

The capacity of the press is 1333 kN acting on the main platen, while the blank holder can provide 667 kN of clamping force. These loads are controlled by hydraulic pressure; the main platen is actuated by a 457mm diameter (18" dia.) hydraulic piston, while the binder is actuated by four - 152mm diameter (6" dia.) hydraulic pistons. Experimental data is recorded using a PC-based data acquisition system controlled by the LabView software system.

The tooling used to stamp the panels, shown in Figure 4.4, was manufactured as part of an unrelated study on lubrication also sponsored by ALCAN. The design of this tooling is intended to simulate a scaled down hood of a typical automobile. Drawbeads are incorporated in the IRDI tooling, as shown in Figures 4.4 and 4.5. These drawbeads maintain tension in the sheet during stamping, by forcing the sheet to bend over the drawbead as the sheet flows through the drawbead region. The tension provided by the drawbead helps resist the onset of sheet wrinkling, caused when compressive in-plane stresses develop in the sheet. The mathematical modelling of drawbeads will be covered in further detail in section 5.1.5; however it is important to note that there exists two drawbead regions on the IRDI tooling, as shown in Figure 4.5. The drawbead geometry varies somewhat within each region as a hand grinder has been used to achieve their present shape. In the shallow region, the female drawbead depth is 3 - 4mm, while in the deeper region it is 5 - 6mm. The male drawbead is part of the binder, shown in Figure 4.4, the height of the male drawbead ranges from 5 - 6mm in both regions. The binder is relatively thin at 50mm (2") and flexed during the forming operations.

Also shown in Figures 4.4 and 4.5 are several stop-blocks that were bolted to the binder. The height of the stop-blocks can be varied to prevent the binder from fully closing on the die and also to control sheet draw-in during panel stamping. The minimum clearance between the die and binder was 1.4mm, a limitation that exists because of drawbead geometry and the flex in the binder. If the die is allowed to come closer than 1.4mm, then the sheet would be pinched between the drawbeads, resulting in tearing of the blank.

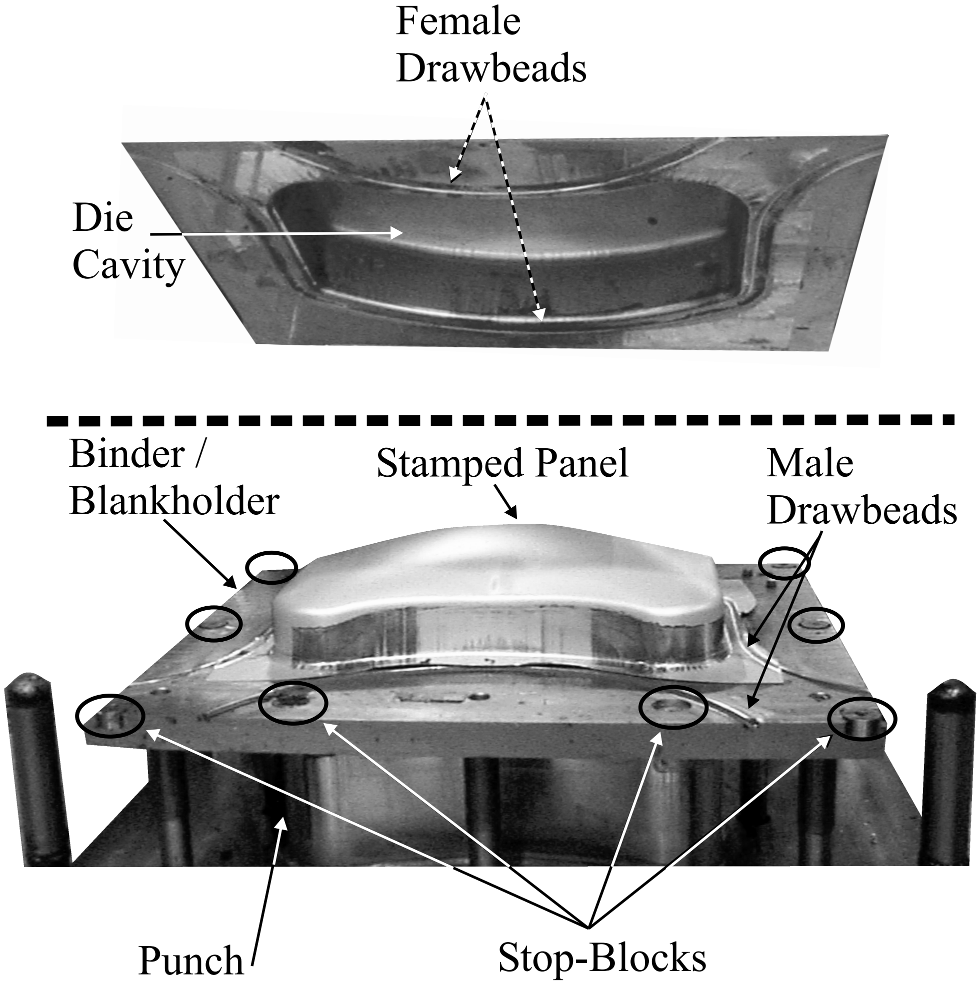

Figure 4.4: IRDI Die Set. The top half of the figure is rotated to show the die cavity and surrounding female drawbeads, while the lower half shows the punch, the blank holder, the stop-blocks and male drawbeads. The visible stop-blocks are circled.

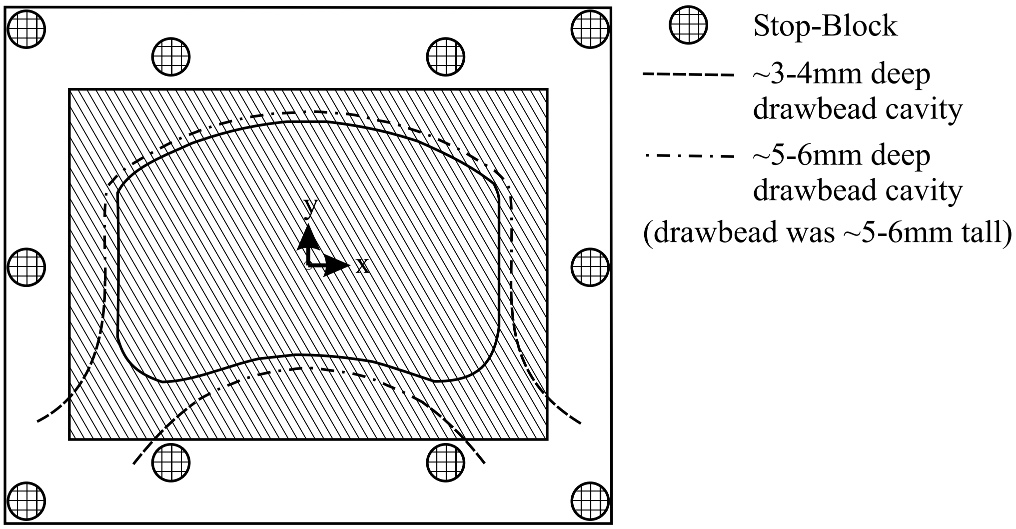

Figure 4.5: IRDI Binder Configuration. This figure shows the location of the binder stop-blocks. The blank is shaded to show placement prior to panel stamping and the two drawbead regions are shown.

4.1.1 Specimen Preparation

The 1.0mm AA5754 sheet used for this study was sheared from ALCAN coil number 12918117. Each blank was shipped in a pre-lubricated condition with an oil based lubricant, Parker MP404. The blanks were sheared to the dimensions of 785mm x 570mm. The sheet rolling direction was parallel to the 785mm dimension of each blank. 50.3mm diameter circles were scribed onto the surfaces of several undeformed blanks. During the forming operations these circles deform into ellipses that can be measured to provide an estimate of strain in each panel. Relatively large diameter circles of 50.3mm were used, as the strain levels in the panel only reached 2-3 percent strain which was too low for the resolution of more conventional techniques such as circle-grid analysis [73].

The 0.8mm, 0.93mm and 1.0mm AA6111-T4PD sheet provided by ALCAN for this study was sheared to the dimensions of 785mm by 570mm. In order to save material, the sheet rolling direction was chosen to lie parallel to 570mm dimension of each blank, which is perpendicular to the orientation of the AA5754 sheet. Parker MP404 lubricant was applied to each side of the AA6111 sheets prior to stamping using a paint roller.

4.1.2 Tooling Setup

The IRDI tooling was set up so that the stop-blocks shown in Figure 4.4 stood 1.4mm proud of the binder. This gap results in an initial overclosure of 0.6 - 1.6mm in the shallow drawbead cavities, but due to the flex in the binder still produced the best part. This configuration was kept constant for all of the panels. For both the AA5754 and AA6111 sheet, the main ram pressure was 6,067kPa (880psi), which results in a force of 996kN acting on the die. The average pressure acting on each of the four binder posts was 7,670kPa (1,113psi) for the AA5754 sheet, but for the AA6111 sheet, this was increased to an average of 12,404kPa (1,800psi). This results in a force of 249kN acting on the binder for the AA5754 and 402kN for the AA6111. All of the panels were drawn to a depth of 100mm as shown in Figure 4.1.

During forming, it was found that the four stop-blocks shown in the top of Figure 4.5 prevented the binder from applying sufficient tension in the 0.8mm and 0.93mm AA6111 sheet. This caused wrinkling in the stamped panels as shown in Figure 4.6. As was mentioned earlier, the stop-blocks could not be removed without causing the drawbeads to tear the sheet during stamping of the panel. As the wrinkling was outside of the regions subjected to dent loading, it was decided that the lower thickness AA6111 panels could still be used for subsequent denting analysis.

4.2 Paint Bake Cycle

All of the AA6111 panels underwent a single heat treatment cycle of 32 minutes at 177°C prior to dent testing. As was discussed in Chapter 3, this single heat treatment cycle is representative of an automotive paint bake process. A heat treatment oven, approximately 10 cubic meters in volume was used for this step. The oven was manufactured by Despatch Limited and had a closed loop temperature control system. The temperatures of the oven, the stamped panels and tensile specimens were monitored during heat treatment, using a PC data acquisition system running the LABTECH software. Thermo-couples were suspended in the oven and were taped to several of the panels and tensile specimens during heat treatment to ensure that differences in temperature were small.

4.3 Static Dent and Panel Stiffness Tests

Static dent tests were performed on both the AA5754 and AA6111 panels. The AA5754 panels were statically dented at the five locations (A,B,C,D,E) shown in Figure 4.2, while the AA6111 panels were dented at locations A, B and C. A schematic of the static dent test apparatus is shown in Figure 4.7, while a closeup of a panel being tested is shown in Figure 4.8. A 25.4mm (1 inch) steel ball was used as the indentor for both the static dent and stiffness tests.

It was mentioned in Chapter 1 that the experimental programme was derived from recommendations of ALCAN personnel [45] and the Standardized Dent Resistance Task Force report [34]. The static dent test procedure developed for the current work was as follows:

1. The IRDI panel was clamped to the adjustable platform. If necessary, the panel was trimmed to fit inside of the clamps shown in Figures 4.6 and 4.8.

2. A fiber-glass template was used to mark the location of each dent. This template was fabricated by moulding fiber-glass over one of the panels, after which holes were drilled at each dent location.

3. The bubble-type level shown in Figure 4.9 was used to insure that the panel was level at the dent location.

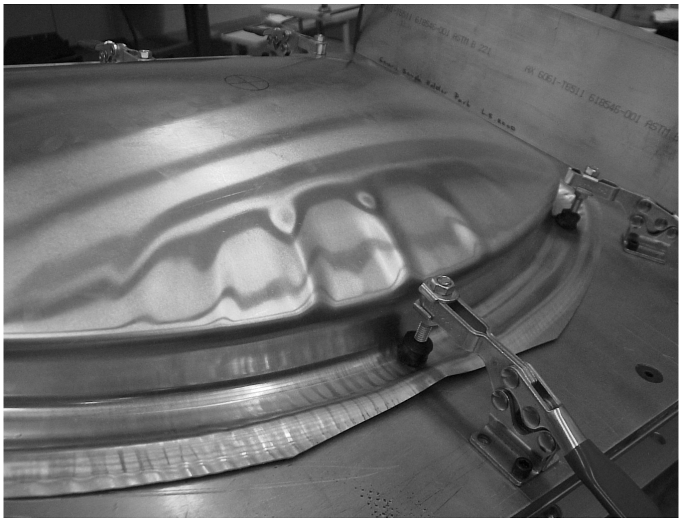

Figure 4.6: Wrinkles that were present in the 0.8mm and 0.93mm AA6111 sheet after forming.

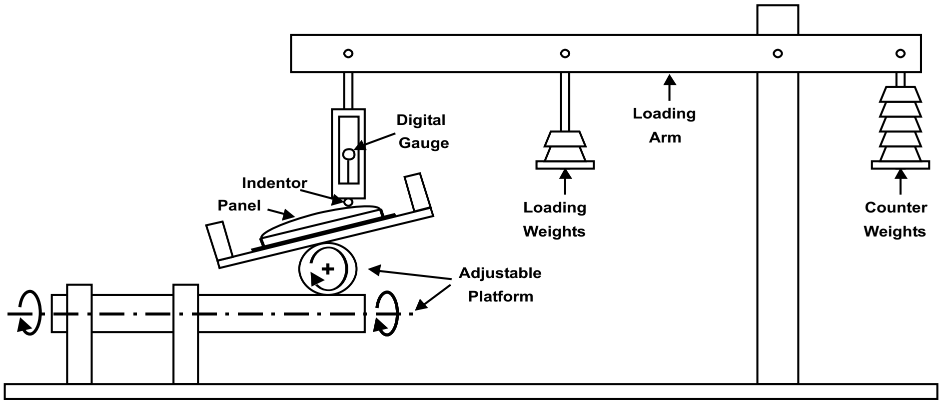

Figure 4.7: Experimental setup for a static dent test. Each panel is clamped in an adjustable platform that can be positioned so that the loading direction is normal to the surface of the panel. The loading arm is leveled and balanced prior to each test.

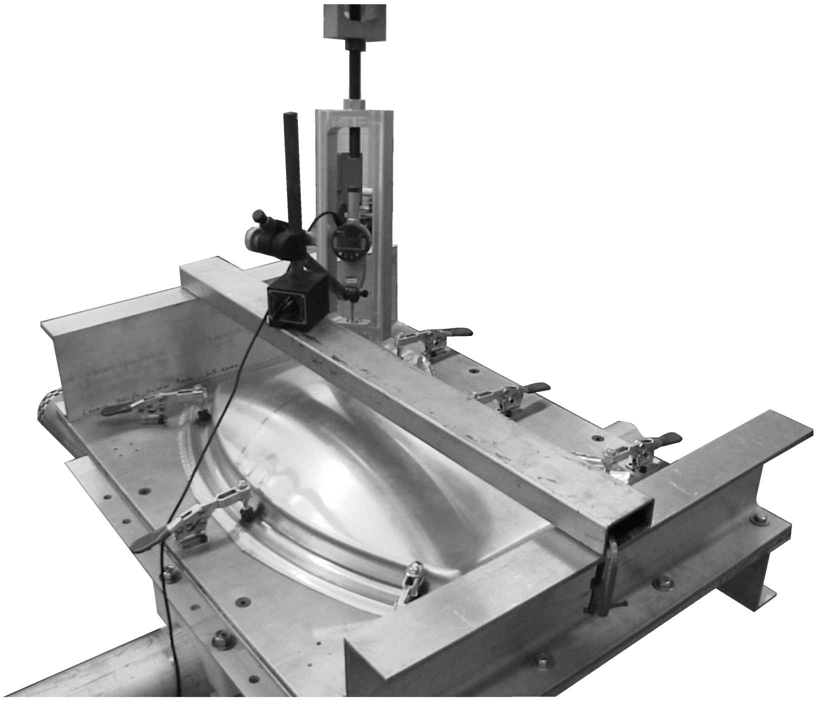

Figure 4.8: Closeup of a static dent test showing the clamped panel under load. The digital gauge measures panel deflection relative to the base of the platform.

4. The loading arm was positioned so that the indentor would contact the panel at the dent location.
5. The platform that held the weights was positioned halfway between the indentor arm and the loading arm pivot. For each weight added, a load of 1/2 the weight would be applied through the indentor to the panel.
6. The loading arm was levelled and balanced with counter-weights to ensure that the indentor was balanced at, or just above, the dent location.
7. A 4.45N (1-lb) weight was loaded onto the weight platform to pre-load the system.
8. As shown in Figure 4.10, the digital gauge was affixed to the adjustable

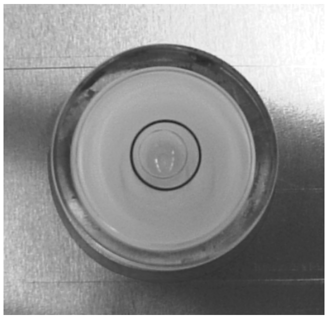

Figure 4.9: Bubble-type level used to level each panel at the dent site.

platform with a magnetic clamp, aligned to act in the vertical direction at the dent location and was zeroed. As the panel was leveled at the dent location, this ensured that the normal deflection of the panel would be measured.

9. A 44.48N (10-lb) weight was loaded onto the weight platform and 10 seconds was allowed to pass to allow any settling of the panel surface.
10. The displacement of the indentor was measured.
11. The 44.48N (10-lb) weight was removed and 10 seconds was allowed to pass.
12. The displacement of the indentor was measured.
13. The method described in the above four steps was repeated for total applied loads of 88.96, 133.44, 177.92, 222.40, 266.88, 311.36, 355.84, 400.32, 444.80 and 489.28N (20, 30, 40, 50, 60, 70, 80, 90, 100 and 110-lbs). As each weight was added or removed from the weight platform, ten seconds was allowed to pass before recording a displacement.
14. In order to save time during some tests, the ten seconds was only allowed to pass prior to recording the displacement at peak load, and

Figure 4.10: Close-up of the digital gauge used to measure normal displacement of the IRDI panel during static denting.

after complete unloading for each cycle. During these tests, no displacement data was recorded at the intermediate loads for each load cycle. For example, if the peak load for the cycle was 50-lbs, then the full 50-lbs would be loaded onto the weight platform, ten seconds would be allowed to pass and the displacement was then measured. Following this, the full 50-lbs would be removed, ten seconds would be allowed to pass and the displacement was then measured.

15. The residual dents for each load was the displacement of the indentor after unloading to the 1-lb preload weight.
16. Initial panel stiffness was calculated for each panel using the static dent load-displacement data. Each stiffness value was calculated as 44.5N divided by the displacement of the indentor at the 44.5N load, which is in accordance with the Auto/Steel Partnership report [34].

4.4 Dynamic Dent Tests

A schematic of the test apparatus used to perform the dynamic dents is shown in Figure 4.11. This setup uses kinetic energy gained from a free-falling 25.4mm diameter indentor to dent the panel. Prior to its release, the indentor is held by an electromagnet above the panel, the height of which can be varied. The impact velocities of the indentor ranged from 1.98 to 4.2 meters per second, calculated based on drop heights of 200mm to 1200mm, and neglecting drag. Each type of panel was dented at locations A, B and C in Figure 4.2; however, the number performed depended on the repeatability of each test, as well as the dent depths that were achieved in prior tests. As the number of tests performed on each type of panel varied, a summary of all the dynamic dent tests performed is given in Table 4.1.

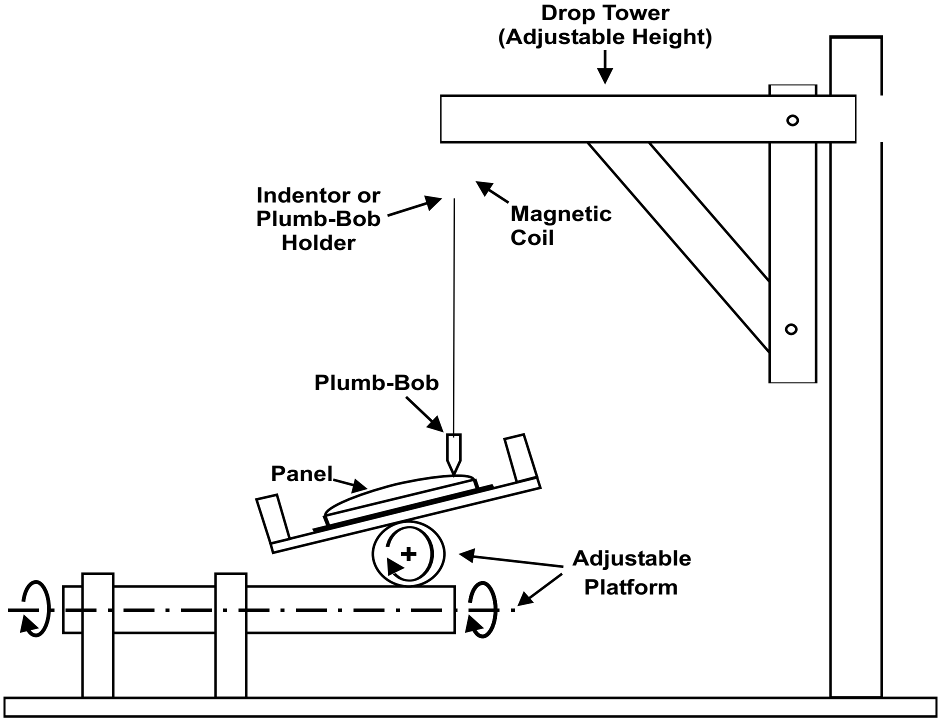

Figure 4.11: Experimental setup for a dynamic dent test. Each panel is clamped to an adjustable platform that is positioned so that the vertical direction is normal to the surface of the panel. The electromagnetic coil is used to hold the indentor, or plumb-bob directly above the dent site and is de-activated with a remote switch. The height of the drop tower is adjustable so that sufficient kinetic energy can be gained during the indentor's free-fall.

Table 4.1: A listing of the number of dynamic dent tests performed on each type of stamped panel.

Drop Height [mm]	**Panel Type and Location**											
	5754			**6111**								
	1.0mm			**0.8mm**			**0.93mm**			**1.0mm**		
	A	**B**	**C**	**A**	**B**	**C**	**A**	**B**	**C**	**A**	**B**	**C**
200	3		1	1		2						
300	1	1	1			1						
400	1	1	3									
500	1	1	1	3	3	3	3	3	3	3	3	3
600	3	1	1									
700	1	1	1	2								
800		1		1	2	1	1	1	1	1	1	1
900		1	2	1								
1000				2								
1100												
1200				4	3	4	3	3	3	3	3	3

The procedure for each dynamic dent test was again derived from recommendations of ALCAN personnel [45] and the Standardized Dent Resistance Task Force report [34] and was as follows:

1. Each panel was trimmed and clamped to the adjustable platform as in the static dent tests.

2. The dent location was marked and levelled using the adjustable platform and a level.

3. A dent measurement fixture, shown in Figure 4.12(a), was positioned over the dent location and levelled. This fixture consists of a flat platform and three sharpened pins for legs. The pins enabled small indentations to be made in the panel surface, which allowed the measurement fixture to be repositioned in the same location.

4. The initial position of the panel surface relative to the measuring platform was taken as shown in Figure 4.12(b). This reading was taken three times for each test and between each reading, the measurement fixture was removed and re-positioned. The panel height prior to denting was taken as the average of these three readings

5. The electro-magnet on the drop tower was aligned above the dent location at the drop height using a plumb-bob as shown in Figure 4.13(a).

6. The indentor (a 25.4mm steel ball bearing) was held by the electro-magnet as shown in Figure 4.13(b).

7. The indentor was allowed to fall onto the dent site and was caught manually as it rebounded from the panel.

8. Three measurements of the final position of the panel surface relative to the measuring platform were taken as in Steps 3 and 4 (above). An average value was calculated.

9. The dynamic dent depth for each test was the magnitude of the difference between initial and final positions of the panel surface.

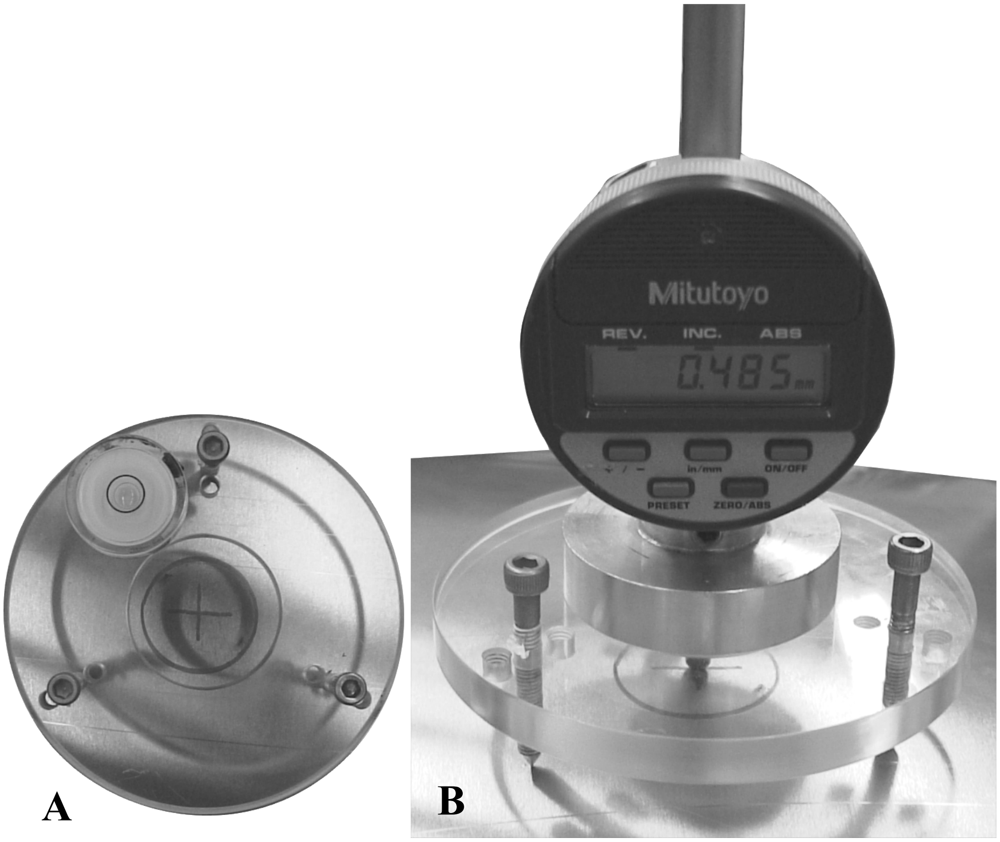

Figure 4.12: (a) Flat measuring platform that is positioned over the dent site, note the use of a bubble-type level to insure level positioning. (b) Measurement of panel location relative to the platform at the dent site.

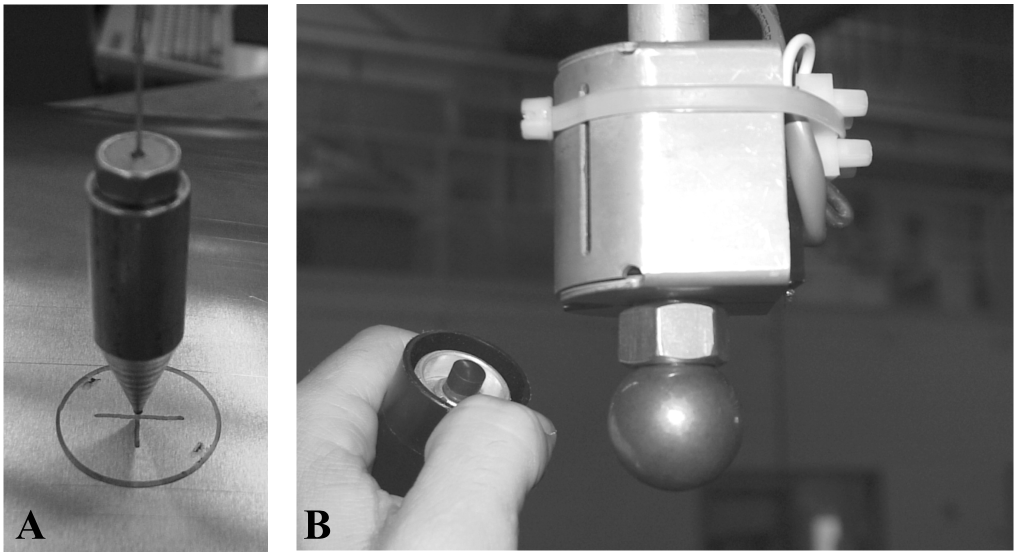

Figure 4.13: (a) Plumb-Bob that was used to position the drop tower. (b) Electro-magnetic coil holding the indentor prior to dynamic denting.

Chapter 5

Finite Element Models

A principal goal of this research was to produce software tools and methodologies to facilitate use of the finite element method (FEM) for accurate predictions of panel stiffness and dent resistance. Figure 1.5 portrays the steps (forming, springback, mesh refinement, static or dynamic denting and springback) that must be simulated in order to predict panel stiffness and dent resistance. The numerical models and simulation techniques developed as part of this research are discussed in this chapter.

The numerical simulations were performed on three different UNIX computing platforms. These were an 18 cpu Silicon Graphics Origin 2000, a 4 cpu Origin 200 and an 8 node Linux cluster. The Silicon Graphics computers ran the IRIX 6.5 operating system, while the Linux cluster ran RedHat version 6.2. The Origin 2000 was configured with 9 gigabytes of memory, the Origin 200 had 2 gigabytes and the cluster had 256 megabytes on each node. The forming, springback and dynamic denting simulations were solved using the LS-DYNA version 950-d [46] finite element software. The static denting simulations were solved using ABAQUS version 5.8.18 [53].

Both LS-DYNA and ABAQUS have implicit and explicit solution capability. In general, implicit solvers are used to solve a system of equations having the general form:

$$\bar{\mathbf{F}}_i = \mathbf{K}\bar{\mathbf{x}}_i \tag{5.1}$$

where $\bar{\mathbf{F}}_i$ and $\bar{\mathbf{x}}_i$ are nodal force and displacement vectors, respectively, and $\mathbf{K}$ is the global stiffness matrix. Usually the forces are specified as boundary conditions, whereas the displacements are unknown. This makes it necessary to invert the stiffness matrix, ($\mathbf{K}$) which for large problems can be quite time consuming and require large amounts of memory. This matrix inversion is subject to numerical round-off errors. Also, certain classes of problems such as sheet metal springback compound the issue due to the ill-conditioned nature of the stiffness matrix. When material non-linearities are considered, the initial estimate of stiffness can be significantly different from the actual stiffness. This requires iterative techniques to be used in order to solve Equation 5.1 for static equilibrium.

Conversely, explicit solvers use forward integration to solve the equations of motion:

$$\bar{\mathbf{F}}_i = \mathbf{K}\bar{\mathbf{x}}_i + \mathbf{B}\bar{\mathbf{v}}_i + \mathbf{M}\bar{\mathbf{a}}_i \tag{5.2}$$

where $\bar{\mathbf{F}}_i$, $\bar{\mathbf{x}}_i$, $\bar{\mathbf{v}}_i$, $\bar{\mathbf{a}}_i$ are nodal force, displacement, velocity and acceleration vectors, respectively and $\mathbf{K}$, $\mathbf{B}$, $\mathbf{M}$ are the stiffness, damping and mass matrices. Usually the damping matrix is either neglected or treated in a simplified fashion in explicit dynamic finite element codes so that the system of equations reduces to:

$$\bar{\mathbf{F}}_i = \mathbf{K}\bar{\mathbf{x}}_i + \mathbf{M}\bar{\mathbf{a}}_i$$

The approach to solving these explicit equations is that at time t=0, the displacements and forces are known, but the acceleration vector is unknown, so:

$$\bar{\mathbf{a}}_i = \mathbf{M}^{-1}\left[\bar{\mathbf{F}}_\mathbf{i} - \mathbf{K}\bar{\mathbf{x}}_\mathbf{i}\right]$$

can be used as an estimate of the nodal accelerations. Inversion of the mass matrix ($\mathbf{M}$) is trivial since in explicit formulations a diagonal lumped mass matrix is typically used. Acceleration is the second derivative of displacement, so multiplication of $\bar{\mathbf{a}}_i$ by the time step twice is an estimate of nodal displacement for the time step. This process is repeated over many time steps until the specified problem time duration is reached. When this method is used the time step must be kept quite small to avoid instabilities. The time step required for solution and stability is governed by the Courant criterion. Computationally, the time is spent doing many simple calculations, whereas in an implicit calculation, the time is spent doing fewer more difficult calculations (matrix inversion). These differences in solution technique makes each form of solver more attractive to a certain class of problem. In problems such as sheet metal forming, many solution steps are required to accurately model the deformation and intermittent tooling-workpiece contact. This makes the explicit solution technique attractive. An implicit technique would require too many matrix inversions to be practicable. Springback problems generally require less solution steps as well as a requirement of attaining static equilibrium. Thus, they are normally solved using implicit techniques.

5.1 Forming Models

In recent years, the explicit dynamic finite element method has been shown to model forming of sheet metal reasonably well with good computational efficiency [50–52]. These simulations must capture tooling contact, friction, drawbeads and sheet anisotropy for accurate prediction of panel strains and final shape. A brief discussion as to how these problems were modelled in the current work is discussed in the following sections.

5.1.1 Finite Element Mesh

Discretisation of the IRDI tooling was provided by ALCAN in the form of a finite element mesh. This model was modified for the current work to simulate both the AA6111 and AA5754 forming operations. An exploded view of this finite element mesh is shown in Figure 5.1. The tooling surfaces for each forming model were modelled using rigid four-node quadrilateral shell elements. Since each forming model was to be used in subsequent denting analysis, the symmetry of the panel was not used to reduce the problem size.

One rather useful feature of LS-DYNA is automatic or "adaptive" mesh refinement of the blank during the simulation. This allows the coarsely meshed blank shown in Figure 5.1 to be refined only as necessary during the simulation, minimizing the computational effort. Within LS-DYNA, element refinement occurs when the curvature of approaching tooling will cause a user specified angle between adjacent blank elements to be exceeded. The element subdivision method is similar to that used in the D-Mesh program, (See Figure 2.7); however, the original curvature of the panel is not approximated. Any new midedge nodes that are added during refinement are constrained to lie halfway between the corner nodes of the original element.

Automatic mesh refinement was used for the blank in each forming model. This increased the problem size significantly during the simulation. The refined finite element mesh of the AA5754 blank after forming is shown in Figure 5.2. Two levels of refinement were specified for the 1.0mm AA5754 and AA6111 models, while one was allowed for the 0.93 and 0.81mm AA6111 models. It was found that at two levels of refinement the problem sizes were becoming large with the increased number of nodes and elements. The larger problem sizes required significant computer memory and CPU time to solve the subsequent springback and denting analysis and this mandated a decrease in problem size. It should be noted that no appreciable difference in forming strains were visible in trial runs of the same models with different levels of adaptivity. A summary of the number of elements present in each blank before and after forming is given in Table 5.1, along with the solution time while running on one SGI Origin 200 (180 Megahertz) cpu.

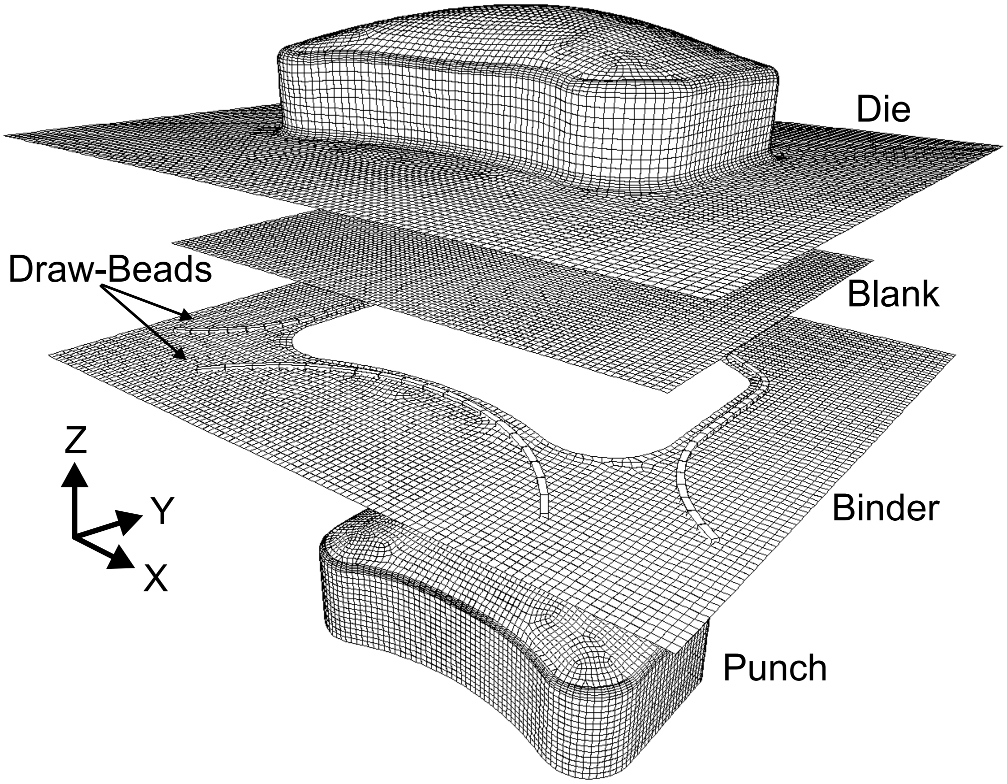

Figure 5.1: Exploded view of the finite element mesh used for the IRDI forming model. The simulated drawbead regions are shown attached to the binder.

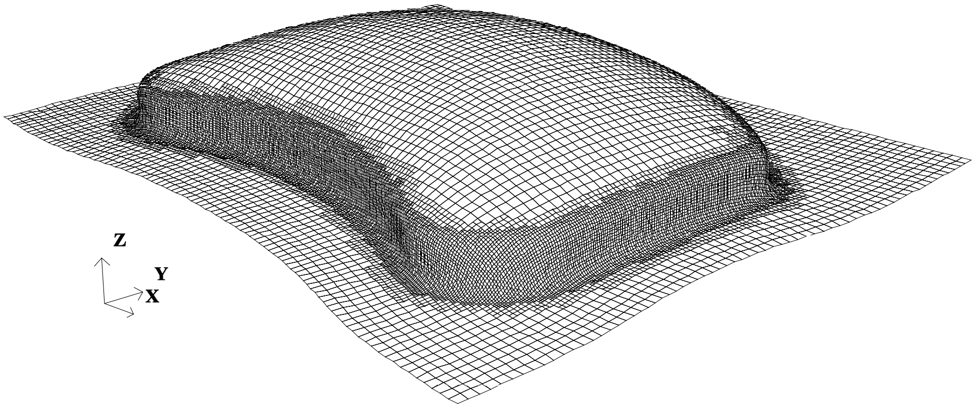

Figure 5.2: The finite element mesh of the blank after adaptive meshing has refined the sidewalls of the panel during the forming operation. This mesh shows two levels of adaptive refinement in the sidewalls.

Table 5.1: A listing of the number of elements initially present in the blank at the start of each forming simulation and the final number after automatic mesh refinement. Also shown is the time required to solve the problem on one SGI Origin 200 cpu running at 180 Megahertz.

Forming Model	**No. of Elements in Blank**		**Solution Time**
	Initial	**After Refinement**	
1.00mm AA5754	5785	27622	104.6 hours
1.00mm AA6111	5785	36563	99.6 hours
0.93mm AA6111	5785	13235	36.2 hours
0.81mm AA6111	5785	12061	30.2 hours

5.1.2 Element Formulation

Until recently, the Belytschko-Lin-Tsay element formulation [62] has been a popular choice for sheet metal forming simulations within LS-DYNA. This element formulation had provided the best balance between computational efficiency and the accuracy provided by a fully integrated shell element. It was found that this element formulation caused convergence difficulties in subsequent springback analysis, because very accurate residual stresses from the forming simulation are required. For this reason, the blank in each forming model was discretised with a new shell element available within LS-DYNA that is based on the work of Simo and Armero [74]. Within LS-DYNA this element is simply known as element number 16. This is a fully integrated shell element with four (2x2) integration points in-plane and seven through thickness integration points. Gaussian integration is employed for both the in-plane and through thickness directions and thickness changes are captured based on the in-plane strains. Use of a 2x2 integration scheme in the forming model eliminates the need for hourglass control and properly matches the integration scheme used in subsequent springback analyses. A higher computational cost (4 times) is incurred compared to a single point (in-plane) integration scheme as used by the Belytschko-Lin-Tsay element.

5.1.3 Contact

Within LS-DYNA, there are three types of contact algorithms. The one used for sheet metal forming simulations is known as the penalty method (see Hallquist [46, p23.2]). In this method, contact occurs if the nodes of one body penetrate the surface of another. When this condition occurs during the simulation, normal interface springs are placed between the penetrating nodes and contact surface. The interface spring stiffness, k_i of the penetrated element i is given by:

$$k_i = \frac{f_{si} K_i A_i}{l_i} \tag{5.3}$$

where f_{si} is the user defined interface stiffness scaling factor, K_i is the bulk modulus of the tooling, A_i is the surface area of the penetrated element, and l_i is the maximum shell diagonal of element i. For the current work, the default scale factor of f_{si}=0.1 was used, this value is dimensionless.

Several contact types within LS-DYNA use the penalty method, some of which have been formulated specifically for use in sheet metal forming simulations. These special formulations are required to account for variations of sheet thickness in the blank during forming. The particular contact algorithm used for the current work was the "Forming One Way Surface to Surface" algorithm which checks for penetration of the blank through the tooling, but not of the tooling through the blank. This one way method is faster than a two way algorithm and works best when the mesh of the blank is smaller than the tooling mesh.

5.1.4 Friction

The frictional characteristics of sheet metals can vary considerably from region to region within the tooling during a forming operation. There are many reasons for this, some of which are the quantity and type of lubricant in the local contact region, rolling direction of the sheet metal relative to material drawing direction, high contact pressure between the blank and tooling, temperature gradients within the tooling and degree of sliding along the tooling. Characterisation of different friction values within a forming simulation generally is not done; however, a Coulomb friction model is available within LS-DYNA [46]. This friction model allows for differences in static and dynamic coefficients of friction and has the form:

$$\bar{\mathbf{F}}_f = \left(\mu_d + (\mu_s - \mu_d)\, e^{-c|v|}\right) \cdot \bar{\mathbf{F}}_n \tag{5.4}$$

where $\bar{\mathbf{F}}_f$,$\bar{\mathbf{F}}_n$ are the friction and normal contact forces, μ_s, μ_d are the static and dynamic coefficients of friction, c is a decay constant and v is the relative velocity between the two parts. Examination of this equation reveals that the static coefficient is used until relative motion exists between the blank and tooling, after which the value will transition to the dynamic dynamic coefficient based upon the sliding velocity and decay constant. For the current work, values of 0.125 and 0.120 were used for the static and dynamic coefficients of friction, a value of 1.0 $^{s}\!/_{m}$ was used for c. These values were selected based on past experience at ALCAN and the University of Waterloo with aluminum and the oil-based lubricant that was used, Parker MP404.

5.1.5 Drawbeads

The cross section of a typical drawbead is shown in Figure 5.3. Drawbeads are used in sheet metal stamping processes to produce tension in normally compressive stress regions of the sheet in order to prevent the formation of wrinkles.

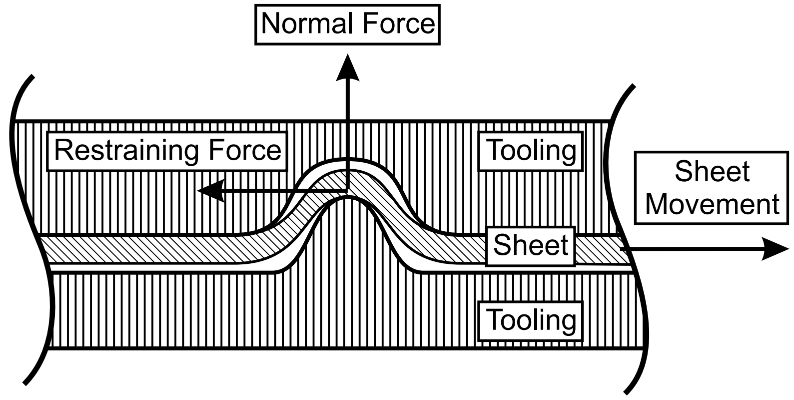

Figure 5.3: Schematic of a drawbead showing the motion of the sheet and the forces exerted on the sheet by the tooling.

Drawbeads can be modelled in two ways within a finite element simulation. The first way is to directly incorporate (mesh) the drawbead geometry within the simulation. This method is generally not done as the amount of refinement required to accurately model the drawbeads would result in an exceedingly small time step size. The second method is to use an analytical drawbead treatment that introduces the tension produced by the drawbead as a restraining force on the nodes of the blank as they pass through the drawbead region. A normal force is also applied to the nodes as the tooling closes. This method was used for all of the forming models in this study; the drawbead regions are shown attached to the die in Figure 5.1. Note that the tooling and the sheet remain flat, as the geometry of the drawbead is not modelled. The tension and normal forces can be estimated for the simulation from prior experiments using a drawbead simulator [75] or from the results of separate finite element simulations that explicitly model of the drawbead geometry. For the current work, small finite element models of the drawbeads were simulated using the method of Maker [76], which predicted the sheet restraining forces and normal forces as a function of drawbead penetration as shown in Figures 5.4 and 5.5, respectively. Note how the shallow drawbead sections discussed in Section 4.1 create larger forces as the sheet is pinched between the die and binder.

5.1.6 Displacement Boundary Conditions

As was mentioned in Chapter 4, the IRDI press had a moving platen and stationary punch. The die, shown in Figures 4.4 and 5.1, was bolted to the platen, while the binder was forced against the moving die by hydraulic pistons. In order to model these motions during the forming operation, the following boundary conditions were enforced.

The downwards (-z direction) motion of the die was enforced with a cosine-hold velocity profile as shown in Figure 5.6. In order to model the gap created by the stop blocks discussed in Section 4.1.2, the motion of the binder also had to be enforced with the same velocity profile. The binder and die were additionally constrained from movement in the x and y directions, while the punch was fully constrained.

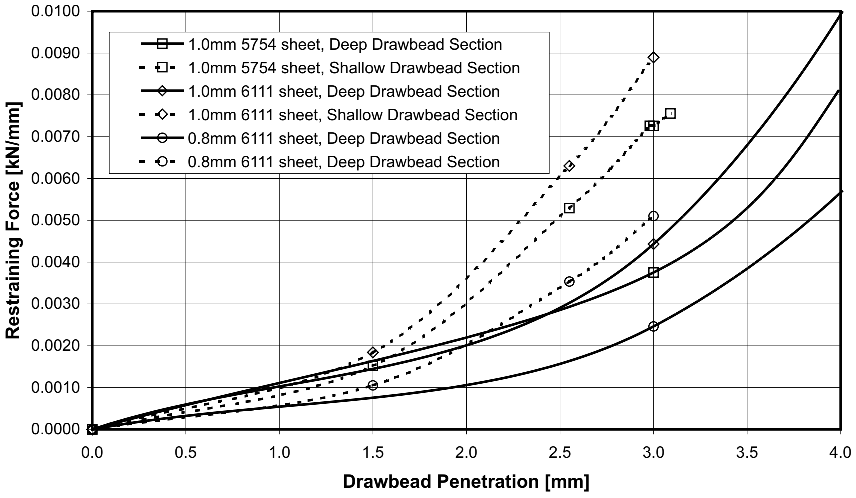

Figure 5.4: Estimation of IRDI drawbead restraining forces for AA5754 and AA6111 sheets. The drawbead force is normalised per unit length (1mm) of drawbead.

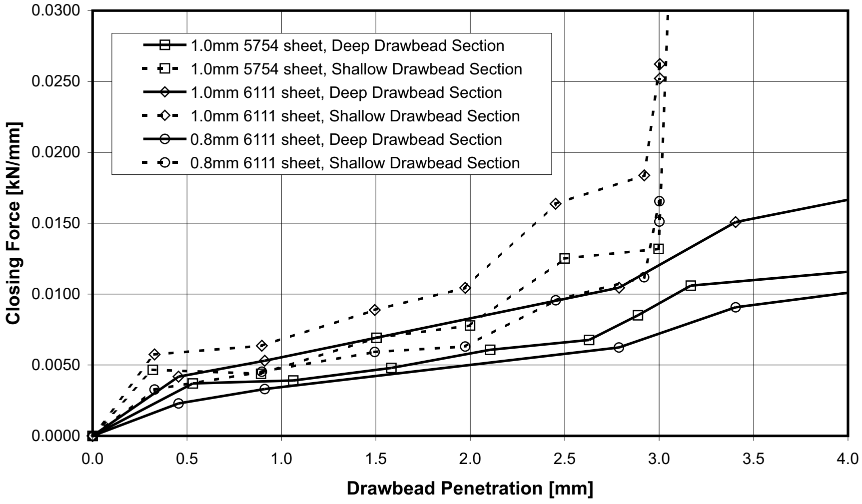

Figure 5.5: Estimation of IRDI drawbead normal forces for AA5754 and AA6111 sheets. The drawbead force is normalised per unit length (1mm) of drawbead.

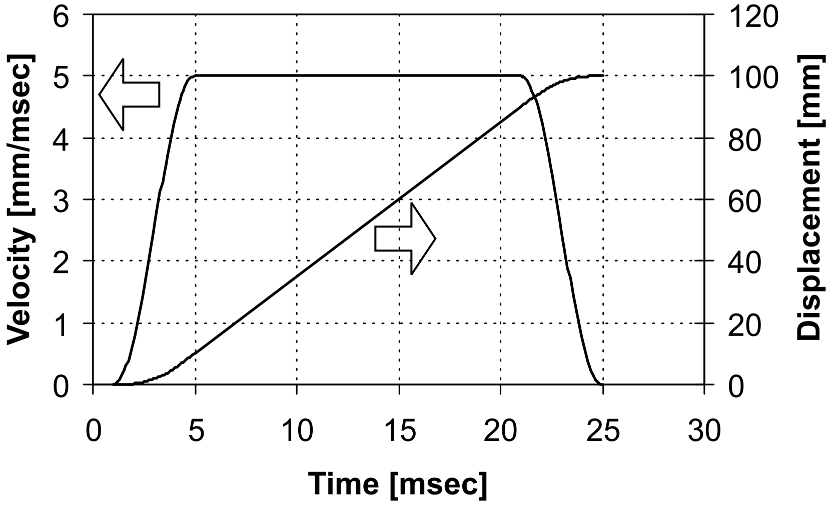

Figure 5.6: Prescribed cosine-hold velocity boundary condition for the die and binder. This type of boundary condition results in a smooth displacement curve which is also shown.

5.1.7 Anisotropy

As was discussed in Chapter 3, the aluminum sheet is an anisotropic material that has different physical properties in different directions. Anisotropic materials have been modelled using FEA, as in Lamontagne [51] who looked at the effect of using different plastic yield functions on the formability predictions of aluminum sheet. One of these yield functions was created by Barlat and Lian [77] and is available in LS-DYNA as the 3-Parameter Barlat material model. This material model is considered state of the art for capturing anisotropy and material thinning in sheet metal during forming simulations using shell elements, so it was used in this work to predict the sheet behaviour during the forming.

5.1.8 Forming Model Output

The results of the forming model are output in the form of computer files. One of these is the so-called “dynain” file, which contains the deformed finite element mesh, as well as the resulting stresses and strains at each integration point. This file is used as the input for the next stage of the process, springback.

5.2 Springback Models

The use of the implicit finite element method to predict springback in sheet metal after a forming simulation has been covered in several prior studies. Two of these are the Numisheet benchmark on springback of a U-shaped channel [52] and more recently by Zhou [54] on springback of U-channel formed tailor-welded blanks. Springback prediction for stamped parts remains an art due to the ill-conditioned nature of the equations. Ill-conditioning of any stiffness matrix (**K** in Equation 5.1) arises when a large percentage of both high and low eigenvalues are present after inversion. In sheet metal, large eigenvalues result from the stiff in-plane deformation modes, while the less stiff out-of-plane deformation modes produce small eigenvalues. The size of the finite element mesh also contributes to the problem, as round-off errors accumulate during the matrix inversion. Due to these problems, the analyst must typically coax the solution to converge by using numerical tricks such as artificial stabilisation and solution step size control. A discussion of the springback models and the techniques used to obtain convergent solutions are discussed next.

5.2.1 Finite Element Mesh

The finite element mesh for each springback model was taken from the last stage of the forming prediction. These models are written by LS-DYNA for the purpose of springback prediction and include the sheet thickness, residual stresses and plastic work accumulated by the elements. A typical mesh after forming was shown previously in Figure 5.2.

5.2.2 Boundary Conditions

During the experiments, each stamped panel was clamped to a flat adjustable base as shown in Figures 4.8 and 4.11. To enforce this condition for the subsequent denting analyses, the flat outer flange on each blank was fully restrained from movement. This flange is visible in Figure 5.2 and can best be described as the material that hasn't drawn into the die cavity during the forming simulation.

5.2.3 Element Formulation and Material Models

The proper choice of element formulation during a springback analysis is critical to obtaining a convergent solution. It was mentioned previously that LS-DYNA shell element number 16 is a fully integrated element, which aids convergence of springback problems. This element was found to give the best chance to obtain a convergent springback solution, so it was used for each springback problem. As in the forming simulations, a seven point Gaussian through thickness integration rule was used.

The choice of which material model to use for the springback solution depended on whether the model was to be used for a static or dynamic dent simulation. ABAQUS does not support the more advanced anisotropic 3-parameter Barlat material model [77], so for any models that were to be statically dented an isotropic von-Mises model [53] had to be used. The models which were to be used for dynamic denting retained the 3-parameter Barlat material description. The process of paint baking the AA6111 sheet was also included in the springback models by using the stress-strain curves taken from the tensile tests performed on paint baked panels as discussed in Chapter 3.

5.2.4 Springback Solution Control Parameters

Typically, each springback simulation was broken down into a target of four load steps, allowing non-linearities in the springback to be spread out over the four steps. LS-DYNA's capability to automatically decrease the step size in the event of non-convergence was employed for more problematic springback solutions. Several of the springback problems required many iterations, so the maximum allowable iterations per solution step was increased to 300 before LS-DYNA would decrease the step size and re-try. The default quasi-Newton BFGS non-linear equation solver [46] was used.

There are two criteria used by LS-DYNA to determine whether the solution has converged. These are the conditions placed on displacement:

$$\frac{\|\Delta \bar{\mathbf{u}}_i\|}{\bar{\mathbf{u}}_{max}} < \epsilon_d \tag{5.5}$$

and energy:

$$\frac{\left|\Delta \bar{\mathbf{u}}_i^t \bar{\mathbf{Q}}_t\right|}{\left|\Delta \bar{\mathbf{u}}_0^t \bar{\mathbf{Q}}_0\right|} < \epsilon_e \tag{5.6}$$

where $\Delta \bar{\mathbf{u}}_i$ are the increments in nodal displacement and $\bar{\mathbf{u}}_{max}$ is the maximum nodal displacement. $\bar{\mathbf{Q}}_0$ is the initial residual force at each node and $\bar{\mathbf{Q}}_t$ is the final residual force at each node. The parameters ϵ_d and ϵ_e are user specified constants. For the current work they were set to 0.001 and 0.01, respectively.

5.2.5 Springback Model Output

LS-DYNA writes the results of the springback simulation to a series of computer files. The so-called "dynain" file is also written and is used as the input to the next stage, remeshing.

5.3 Remeshing

Once a springback solution was obtained, the resulting finite element mesh had to be refined at the location to be dented. This was necessary to insure sufficient resolution to capture the very small displacements and sharp gradients in strain adjacent to the dent site. Initial static denting models on the AA5754 pans used the linear paving algorithm discussed in Section 2.4.2. These models had three levels of refinement within a 30mm radius. Any mid-edge nodes present from the forming simulation were removed as discussed in Section 2.4.4. Although these models performed well, it was felt that panel softening would be better captured by a larger radius of refinement. As such, all denting models were refined using the target area paving algorithm also discussed in Section 2.4.2. The target area for each element was 3mm^2, while the refinement radius was 100mm. It was found that these parameters resulted in a final element size of slightly less than 1mm^2 beneath the indentor. Figure 5.7 shows a model refined at location C prior to denting. The other locations had similar refinements.

As discussed in Section 2.4.3, the curvature in each panel was estimated from the starting mesh and the newly created nodes were projected to this curved surface. For this, the default curvature scale factor of 1.0 was used. The indentor was positioned with its z-axis normal to the surface of each panel. ABAQUS does not account for shell thickness during implicit contact, so for models that were to be statically dented, the indentor was positioned right on the refined mesh, without accounting for shell thickness. This is necessary to ensure that contact will be properly established between the indentor and the blank at the start of the static denting simulation. Within LS-DYNA, shell thickness can be accounted for during contact simulations, so for dynamic denting models, each indentor was positioned 0.2mm away from the outer panel surface.

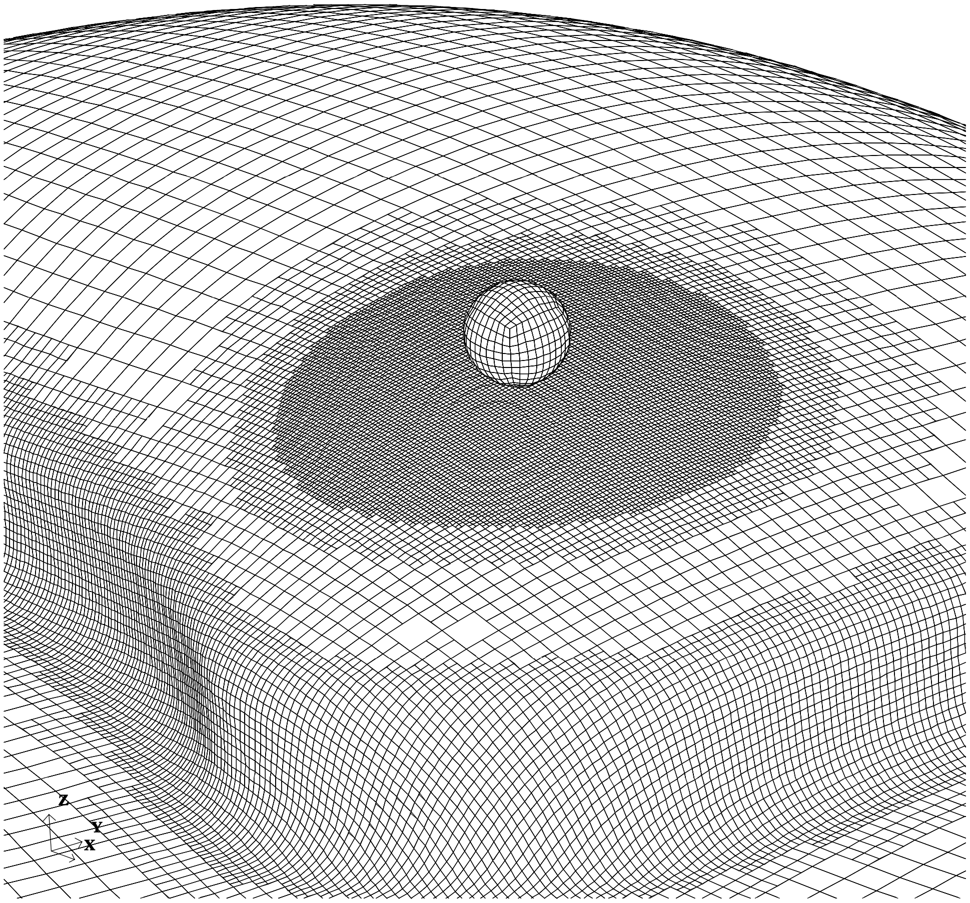

Figure 5.7: A refined finite element mesh prior to static denting at location C.

5.4 Denting

The finite element models output from D-Mesh consists of input files that require little modification to run. The content of these files is discussed in the following sections.

5.4.1 Panel Stiffness and Static Denting

The panel stiffness and static denting models were solved with ABAQUS Standard, version 5.8.18. The size of these models became quite large, requiring close to 900 Megabytes of RAM to run. File output from these simulations was considerable as well. It was common for a static dent simulation to output three Gigabytes of data to disk, which resulted in a more than 40 Gigabytes of data written to disk for the 14 static dent simulations. Fortunately, most of this simulation data was not required during post-processing, thereby allowing more reasonable disk space usage once the simulation had been completed.

5.4.2 Element Formulation and Material Properties

The IRDI panel was modelled using ABAQUS shell element type S4. This is a non-reduced integration element, similar to the element formulation adopted within LS-DYNA. Both of the elements use four in-plane integration points; however, the ordering convention of these points is different within each code. This fact is accounted for when stresses were initialised by the SIGINI and HARDINI subroutines, to be discussed next. The through thickness integration rule of each element was a seven point Gaussian scheme, the same used within LS-DYNA.

The indentor was discretised using the C3D8R element formulation. This is a reduced-integration, eight noded brick element. Although a rigid shell indentor could have been used, it was easier to use the same mesh in both the static and dynamic denting simulations. In the dynamic simulations, it was easiest to let LS-DYNA determine the inertial properties of the indentor, which required the use of a solid mesh. A limitation of the D-Mesh software also prevented the use of shell elements, as the indentor had to be modelled using brick elements.

The yield stress curves after paint baking were used for the AA6111 panels; these properties, along with the AA5754 sheet properties, were discussed in Chapter 3. An isotropic von-Mises hardening rule was used to model the sheet material yield surface within ABAQUS. The indentor was modelled using the elastic steel properties of E=207GPA and ν=0.29 with ρ=7850kg/m^3.

5.4.3 SIGINI and HARDINI User Subroutines

It is well known that work hardening effects must be included for any dent simulation to be accurate. By default, ABAQUS will only read in three local stresses (σ_{xx}, σ_{yy}, σ_{xy}) and one effective plastic strain value for each shell element in the input deck. This means that any differences throughout the element thickness would be lost if this default method of stress initialisation were used. ABAQUS also allows specification of user subroutines that are compiled and linked to ABAQUS at run time. The interface to these subroutines is described in the ABAQUS user manual [67, 25.2.11, 25.2.17]. If the SIGINI and HARDINI user subroutines are used, the stress and effective plastic strain values can be initialised at each integration point within the finite element mesh. For this work, both SIGINI and HARDINI were used. These were written in FORTRAN 77. These subroutines read the "stresses.inp" file written by D-Mesh (see Section 2.4.6) into memory and then assign the plastic strain and local values of stress for each integration point when called. In this manner, no element history data is lost when transferring results from LS-DYNA to ABAQUS.

5.4.4 Contact

Surface-to-surface-with-gap contact is used to model the interaction between the indentor and the panel during denting. This type of contact allows the surfaces of the indentor and panel to slide and open or close relative to one another. A friction coefficient of μ=0.15 was specified for the contact. The region that can contact with the indentor had to be kept small to minimise memory requirements. By default, D-Mesh includes any element on the panel that lies within 0.6 times the refinement radius as part of the contact definition. All of the elements in the indentor are included within the contact definition. Closed contact is initialised by ABAQUS between any node of the indentor that lies within 0.0005 mm of the panel surface. The careful placement of the indentor described in Section 5.3 resulted in closed contact only at the node closest to the refinement point.

The importance of this last point cannot be understated. Without this initial closed contact between the indentor and panel, the static dent simulation would be unable to converge at the first solution step. Alternatively, if more than one node were in contact, ABAQUS moves the nodes on the panel (without causing strain) to lie on the indentor surface. This would deform the surface of the blank prior to any applied load.

5.4.5 Boundary Conditions

The D-Mesh software writes a series of loading and unloading cycles for each static dent simulation to the output deck. Each cycle starts with a preload of one Newton on the indentor. This preload level was found through trial and error as the minimum amount that could be used without convergence issues becoming a problem. This load is increased to a maximum load in 22.2 Newton (5lbf) increments and then decreased back to 1 Newton by 22.2 Newton increments. The peak load is increased each cycle by 22.2 Newtons until a maximum load of 244.7 Newtons (55lbf) is reached. Recall that this is the same loading used in the experiments discussed in Chapter 4. Section 2.4.5 discussed how the indentor is positioned a specified distance above the panel surface. The application of the load is by a concentrated force to the node on the indentor that is closest to the node on the panel specified by the user. This concentrated force acts in a normal direction to the panel surface. The indentor is also constrained to move only in a direction normal to the panel surface. The panel is constrained from movement using the same constraints specified during springback, i.e., the outer flange of the panel is fully constrained.

5.4.6 Static Denting Model Output

ABAQUS can write abundant data to disk during the simulation. Only one file from each simulation is required to post process the resulting load versus displacement curves. This file has the extension of '.sta' and is know as the "status file". D-Mesh generates input control data specifying that the z-displacement of a node on the indentor to be written to this file. Note that the z-axis of the indentor's reference coordinate system is aligned with the outward normal of the panel at the dent location. This makes it easy to post-process the denting results.

5.5 Dynamic Denting and Final Springback

The dynamic denting models were solved with LS-DYNA version 950-d. On average, each denting model required 1 day to solve on one cpu of an Origin 2000 computer running at 300MHz. The input file written by D-Mesh for each dynamic denting simulation requires no modification to run. The contents of each file is discussed below.

5.5.1 Element Formulation and Material Properties

To retain continuity between the initial forming, springback and dynamic denting models, the element formulation used for each dynamic denting model was element number 16. As before, a seven point Gaussian through thickness integration rule was adopted.

The paint baked yield stress curves were used for the AA6111 panels, while the AA5754 panels used the AA5754-O yield stress curve. The material hardening rule for each panel was the 3-Parameter Barlat model. Initial stresses and effective plastic strains resulting from the forming and springback stages were also included. As in the static denting simulations, the indentor was modelled using the elastic steel properties of E=207GPA and ν=0.29 with ρ=7850kg/m^3.

5.5.2 Contact

A surface-to-surface-with-gap contact formulation was used to model the interaction between the indentor and the sheet during denting. In order to minimise the computing resources required, D-Mesh creates a list of nodes and shell elements that can interact during the simulation. The contact definition includes all nodes of the indentor; however, only shell elements lying within 0.6 times the refinement radius are considered during contact.

5.5.3 Boundary Conditions

Initial velocities of $2\,\nicefrac{m}{s}$, $3\,\nicefrac{m}{s}$ and $4\,\nicefrac{m}{s}$ were prescribed for the indentor at each dent location, for each panel. These velocities were oriented to strike the panel normal to impact surface. This allowed dent depth versus impact velocity to be simulated as in the experimental results. Each panel was constrained from movement using the same constraints as in the springback simulation, i.e., the outer flange of the panel was fully constrained.

5.5.4 Dynamic Denting Springback

Following each dynamic denting simulation, each panel had to undergo one final springback step. These models were run with the same element formulation, boundary conditions, material models and solution control parameters as in Section 5.2.4

5.5.5 Dynamic Denting Model Output

Output from each dynamic denting simulation was in the form of a "dynain" file. The final location of the node under the indentor was compared to its original location prior to denting. The dent depth for every simulation was calculated as the displacement of this node.

Chapter 6

Experimental and Numerical Results

This chapter presents a comparison of the panel forming, springback, and dent predictions with the experimental results. Comparisons of forming strains, blank draw-in and sheet thinning are presented after forming and springback. Load displacement history, panel stiffness and residual dent depth are compared for the static dent tests. Lastly, predictions of dynamic dent depth are compared with measured values for the range of indentor impact velocity considered.

6.1 Panel Forming and Springback

6.1.1 Blank Draw-In and Final Shape

Blank draw-in can be described as the amount of material that is drawn into the die during the forming operation. Typically this is measured as the displacement of the outer edge of the blank during the forming operation. For the current work, blank draw-in was measured for the AA5754 and AA6111 panels and compared to values taken from the forming models. The difference in draw-in between individual gauges of AA6111 was insignificant, so only a comparison of the values for 1.0mm AA6111 is given here. Figure 6.1 shows the dimensions that were measured on both the forming models and stamped parts. A comparison of the predicted and measured values of these dimensions is given in Tables 6.1 and 6.2.

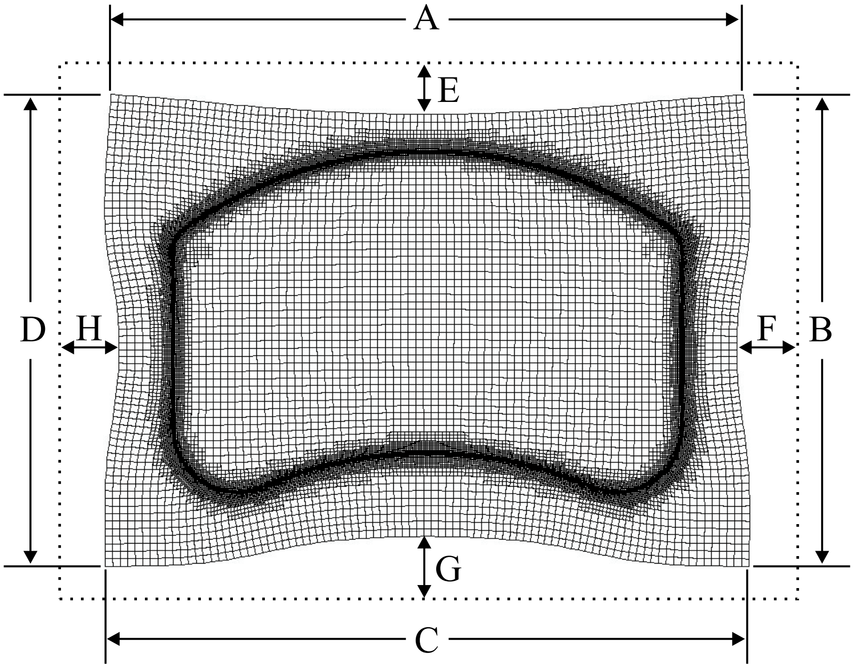

Figure 6.1: Dimensions used to compare the predicted and measured values of draw-in on the 1.0mm AA5754 and 1.0mm AA6111 panels after forming and springback. The initial shape of the blank is shown as a dotted line.

The values given in Tables 6.1 and 6.2 show that although there are some differences between the predicted and measured values of draw-in, the final shape of the panel has been predicted well. Small differences are expected to occur as the drawbead geometry has not been discretised in the finite element models. In the current work, it is important for the forming models to capture the draw-in, but it is much more important for the forming models to capture

Table 6.1: Predicted and measured dimensions of the 1.05mm AA5754 IRDI panel after forming and springback. All dimension values are in mm.

Dimension	**Predicted**	**Measured**	**Error w.r.t. Measured**	
			Absolute	Percentage
A	747.0	750.0	-3.0	-0.48%
B	550.5	550.0	0.5	0.01%
C	760.5	760.0	0.5	0.07%
D	550.9	550.0	0.9	0.16%
E	33.5	33.0	0.5	1.5%
F	28.4	26.0	2.4	9.2%
G	45.8	45.0	0.8	1.8%
H	29.6	26.0	3.6	13.9%

Table 6.2: Predicted and measured dimensions of the 1.0mm AA6111 IRDI panel after forming and springback. All dimension values are in mm.

Dimension	**Predicted**	**Measured**	**Error w.r.t. Measured**	
			Absolute	Percentage
A	743.4	747.5	-4.1	-0.55%
B	545.6	547.0	-1.4	-0.26%
C	753.1	752.5	0.6	0.08%
D	545.4	548.0	-2.6	0.47%
E	37.5	30.0	7.5	25.0%
F	32.0	30.5	1.5	4.9%
G	51.3	46.8	4.5	9.6%
H	33.3	30.5	2.8	9.2%

the thickness changes and strains present in the crown of the deformed panel. These values are compared in the following sections.

6.1.2 Panel Thickness

Tensile specimens were cut from the crown (the center) of each type of panel after stamping. Data from these specimens provided insight into the work-harding of each panel (Section 6.1.3, below) and also allowed measured panel thickness to be compared with the forming model predictions. Comparisons of the average predicted and measured thicknesses at the crown of each panel type are presented in Table 6.3. The AA5754 finite element forming models were run before the material was received, so nominal gauges had to be used in those finite element models. This error created the largest discrepancy, as the initial thickness of the AA5754 sheet was actually 1.050mm, (+5%) but a value of 1.000mm was used in the finite element model. The final measured thickness of the AA5754 panel was 1.030mm, while the predicted thickness was 0.975mm, the majority of the error (90%) due to the error initial thickness. Unfortunately, this model was never updated to reflect the actual thickness of the as-received sheet. It is doubtful whether this affected the subsequent static denting results significantly, as will be shown in Section 6.2; however, this may have affected the dynamic dent results as shown in Section 6.3.

Table 6.3: Predicted and measured panel thicknesses at the center of the IRDI panel after forming. All dimension values are in mm.

Panels	**Initial Thickness**	**Final Thickness**		**Error w.r.t. Measured**	
		Predicted	Measured	Absolute	Percentage
AA5754	1.050	0.975	1.030	-0.055	-5.3%
AA6111	1.002	0.979	0.971	0.008	0.8%
	0.931	0.909	0.904	0.005	0.6%
	0.809	0.785	0.785	0.000	0.0%

6.1.3 Forming Strains

Measurements of engineering strain in the crown of the AA5754 panels revealed strains of approximately 2% in the x-direction and 1% in the y-direction. These values were calculated from measured elongations of 1.0mm and 0.5mm; respectively, of 50.3mm circles scribed in the panel surfaces. The accuracy of these values was estimated to be within 0.3mm as a steel rule was used for measurement. The predictions of strain obtained from the AA5754 forming model are shown in Figure 6.2 for the x-direction and Figure 6.3 for the y-direction.

Note that in Figures 6.2 and 6.3 the range of contour values was set to -3.0% to 3.0%, even though the panels underwent strains as high as 25% in the sidewalls. This setting was used to show the variation of strain in the panel crown, which is the region of interest for denting. Both the measured and predicted strains are comparable, the predicted strains in the x-direction ranged from 1.5% to 2.7%, while strains in the y-direction ranged from 0.3% to 1.8%.

The predicted forming strains for the 1.0mm AA6111 panel are shown in Figure 6.4 for the x-direction and Figure 6.5 for the y-direction. The predicted strains in the 6111 panel had a similar pattern to those in the AA5754 panel, but were slightly less in magnitude. This is expected since AA6111 has a higher yield strength and is able to pull more material into the die prior to plastic yielding. The other gauges of AA6111 had similar strain distributions and are not shown here.

Instead of comparing strain values measured from the surface of each AA6111 panel, it is useful to compare the effective plastic strain values predicted by the forming simulation to those estimated from tensile tests performed on the IRDI panels after forming. This comparison is important because the adopted constitutive formulations utilise a strain hardening hypothesis in which strength is a function of effective plastic strain. Thus, the strength of the tensile specimens taken from the formed and paint baked panels can be used to determine the effective plastic strain for comparison

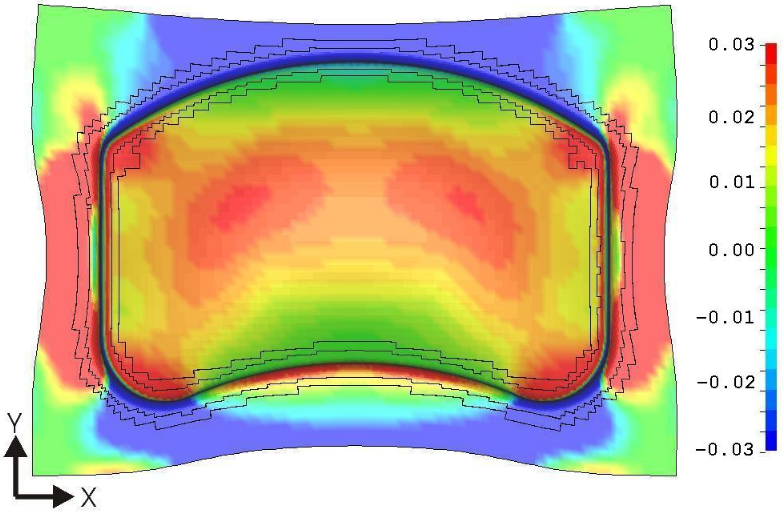

Figure 6.2: Predicted X-direction strains in the 1.000mm thick AA5754 IRDI panel after forming.

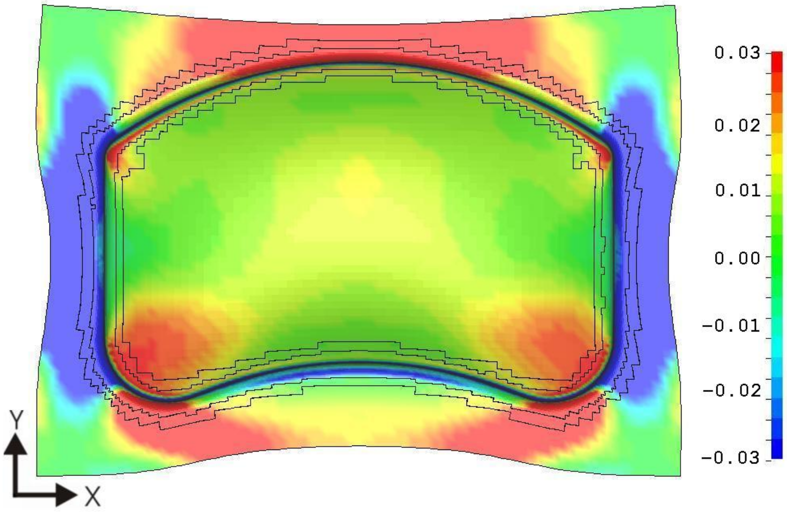

Figure 6.3: Predicted Y-direction strains in the 1.000mm thick AA5754 IRDI panel after forming.

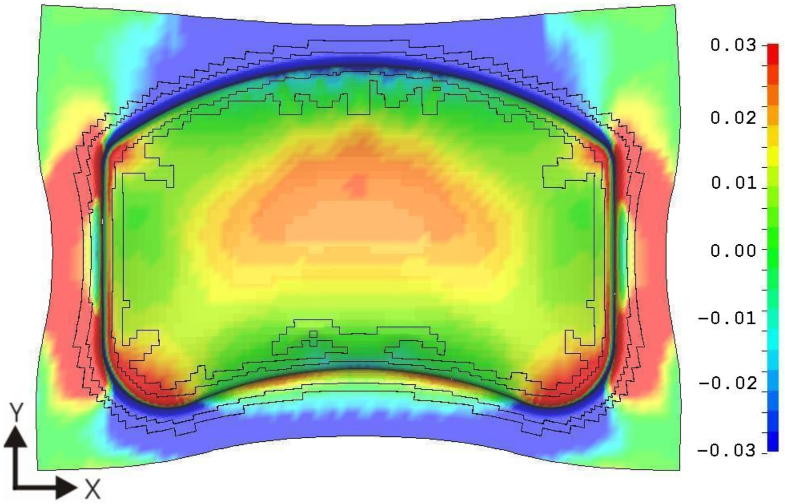

Figure 6.4: Predicted X-direction strains in the 1.0mm AA6111 IRDI panel after forming.

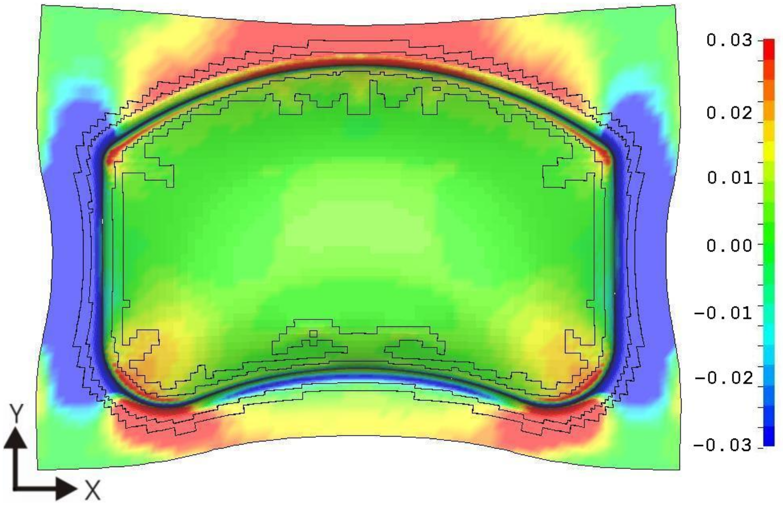

Figure 6.5: Predicted Y-direction strains in the 1.0mm AA6111 IRDI panel after forming.

with model predictions. In the current work, no tensile tests were performed on the formed AA6111 panels prior to paint baking, so the tensile tests performed on the panels after paint baking will be used. Note that it is generally considered that the yield strength increase achieved during a paint bake process is directly additive to the strength increase during work hardening [11]. Thus the yield strength curves shown in Figures 3.5, 3.6 and 3.7 can be used to determine the effective plastic strain in the panels after forming.

Comparison of initial yield strengths for each of the formed and paint baked tensile specimens with the yield strength curve for the paint baked specimen shows a strength increase due to approximately 2.0 to 2.5% effective plastic strain. This value is consistent for each of the AA6111 samples. Figure 6.6 shows the effective plastic strain predicted in the 1.0mm AA6111 panel after forming. At the center of the panel, the effective plastic strain ranges from 2.1% to 2.5%, which compares well with the tensile results. The values of effective plastic strain for the 0.81 and 0.93mm gauges of AA6111 were also in this range. An interesting feature of the AA6111 forming models was that the wrinkling of the sheet evident in Figure 6.6 occurred in the same region as in the experiments (See Figure 4.6). From these results it can be concluded that the forming models are capturing the strain distributions present in the crown of each of the IRDI panels.

6.2 Stiffness and Static Dent Tests

In this section, a series of plots of load versus displacement for each of the static dent tests is presented. The results for the AA5754 panels are presented first, followed by those for the AA6111 panels. For comparison purposes, each of the plots contain both the predicted and measured displacement data. Following the load versus displacement plots, tabulated values of panel stiffness are presented. For dent tests that exhibited more than one stiffness region (See Figure 1.1), data for the secondary and final stiffness regions are also presented. Plots of residual dent depth as a function of applied load

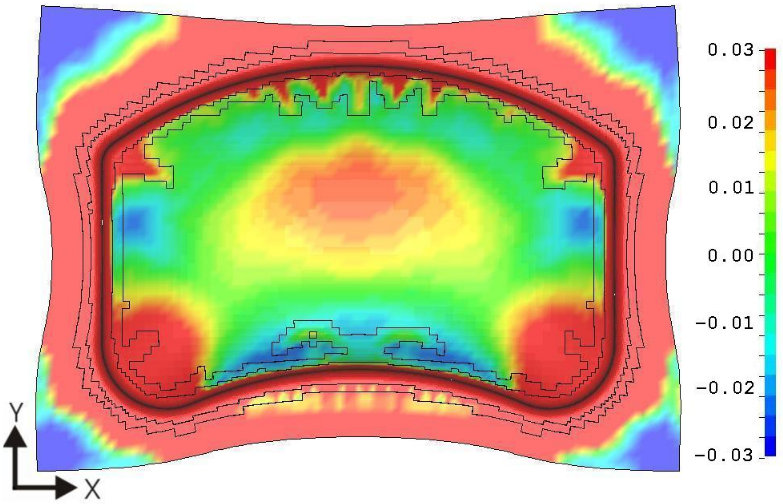

Figure 6.6: Predicted effective plastic strains in the 1.0mm AA6111 IRDI panel after forming. Note the pattern produced by wrinkling on the top of the panel.

are presented last, again with the AA5754 test data presented before the AA6111 test data. For comparison purposes, each type of plot is displayed with identical ranges on the axes.

6.2.1 AA5754 Panel Load-Displacement Responses

The indentor load versus displacement response of various sites on the AA5754 panels are shown in Figures 6.7 through 6.11. These graphs show remarkably good agreement between the numerical predictions of panel stiffness and their associated experimental results. Figure 6.8 shows how the trends of initial, secondary and final panel stiffnesses are captured well using the finite element method, while Figure 6.11 highlights the good agreement for the first two stiffness regions particularly well.

The tests performed on panel locations A,C,D and E (shown in Figures 6.7,6.9,6.10 and 6.11, respectively) showed only the first two panel stiffness regions, while the test performed on location B (Figure 6.8) showed all three. Recall that location B was chosen to lie at the point on the panel with the least curvature, which results in lower initial panel stiffness. During loading, this low initial stiffness was observed to allow a larger deformation zone in the panel relative to the stiffer locations. This deformation zone spread out with increased load, an action which causes bending stresses in the panel to first increase due to the extra moment created, but then decrease due to the larger cross sectional area in bending. As the deformation zone spreads out, the load applied by the indentor is carried initially by bending stresses, followed by membrane tension.

The difficulties in obtaining convergent solutions for these rather poorly conditioned models are highlighted in Figures 6.10. Although this panel is relatively stiff, during the final unloading step (from a load of 22.2 N to 1.0 N) the solver (ABAQUS) had to reduce the step size by 1/5th to obtain convergence. This is evidenced by the tighter clustering of data points on the final unloading step.

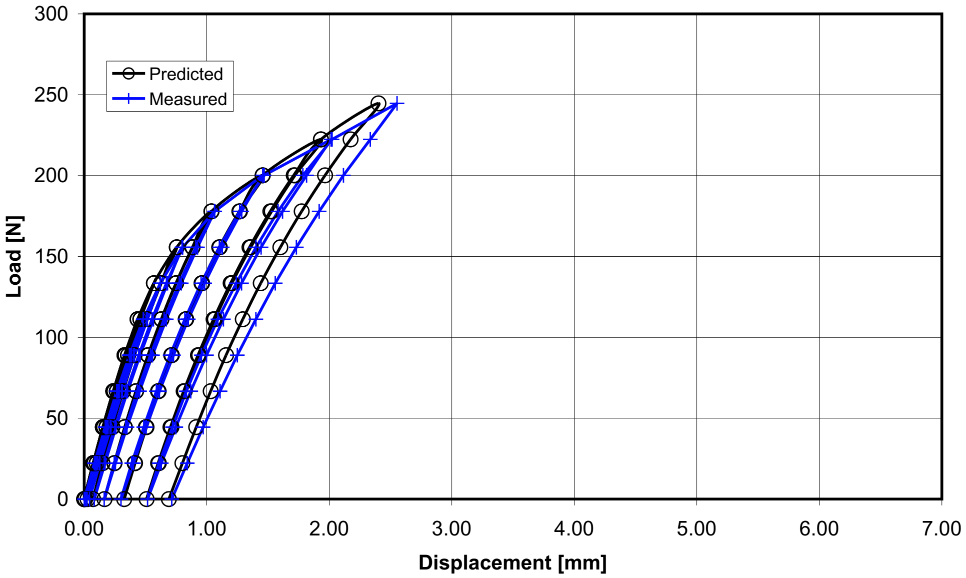

Figure 6.7: Predicted and measured load displacement curves for the 1.05mm AA5754 panel at location A.

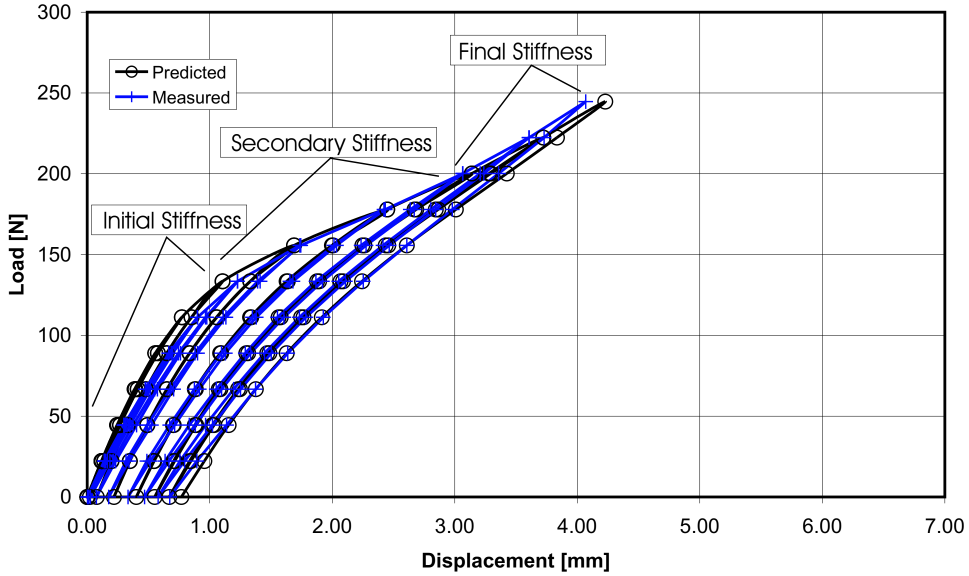

Figure 6.8: Predicted and measured load displacement curves for the 1.05mm AA5754 panel at location B.

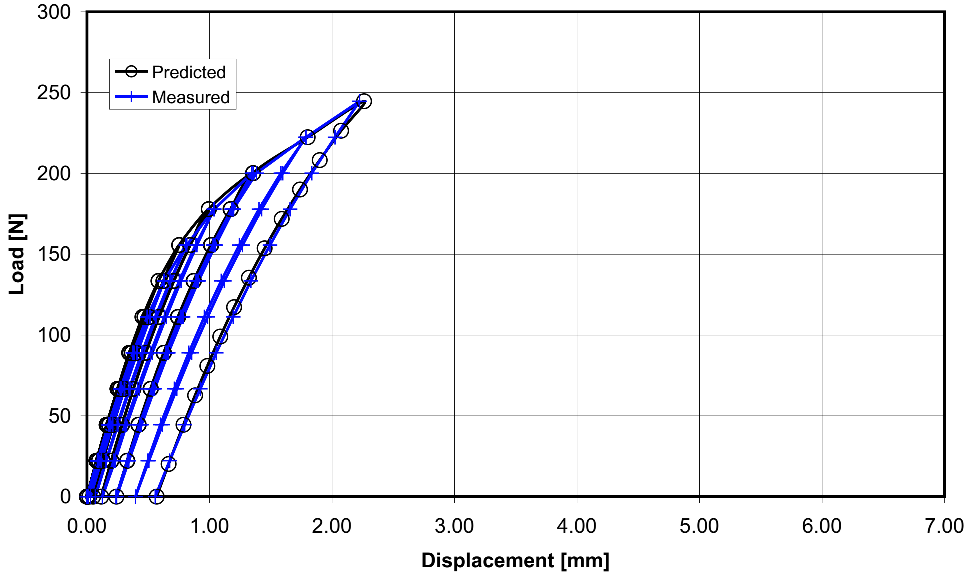

Figure 6.9: Predicted and measured load displacement curves for the 1.05mm AA5754 panel at location C.

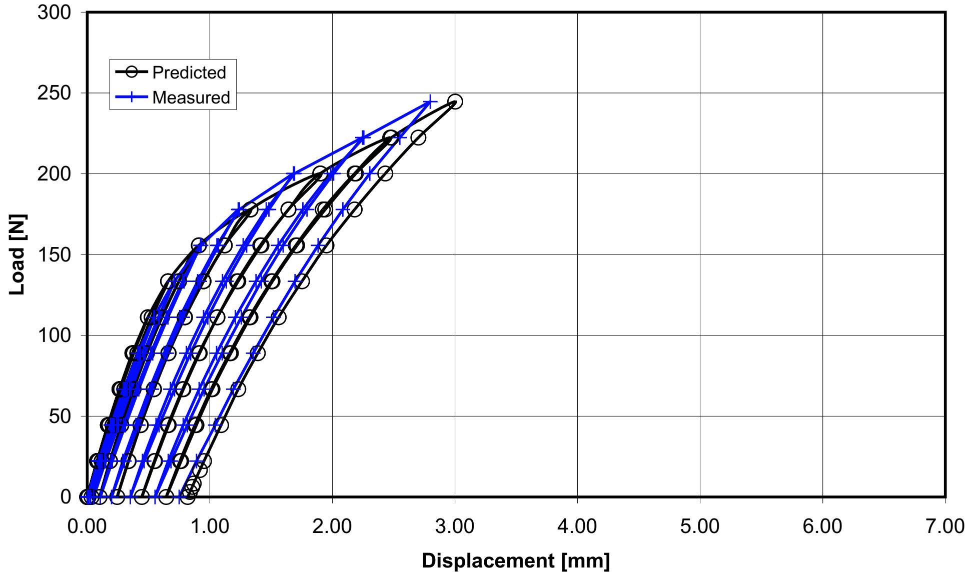

Figure 6.10: Predicted and measured load displacement curves for the 1.05mm AA5754 panel at location D.

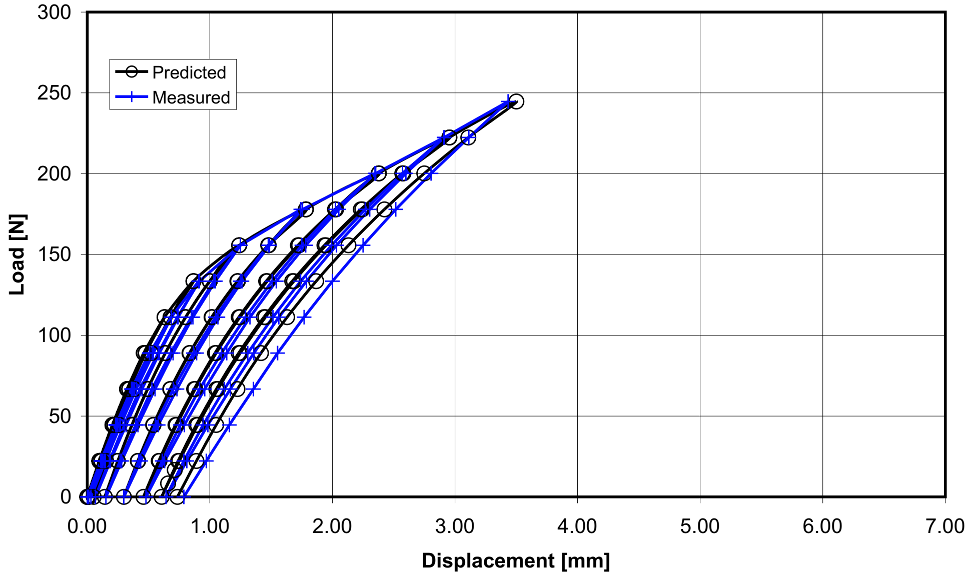

Figure 6.11: Predicted and measured load displacement curves for the 1.05mm AA5754 panel at location E.

6.2.2 AA6111 Panel Load-Displacement Responses

The indentor load versus displacement responses of the AA6111 panels are shown in Figures 6.12 through 6.20. The panels that were dented at locations A and B were tested without recording the data for the intermediate load and unload points, (as discussed in Section 4.3), although the finite element models included these points. During the tests, this made it possible to place or remove all of the weights from the loading arm at once, without waiting 10 seconds after the placement or removal of each weight. This was necessary to save time during the experiments, as each recorded load or unload point takes approximately 45 seconds to record. A test with complete loading and unloading history was estimated to take 2 to 3 hours to complete, so a significant time savings was achieved. It was determined that this did not affect the test results, as some test configurations were tested in both manners to confirm repeatability.

A comparison of the predicted and measured static dent test results for the AA6111 panels shows that the trends of initial, secondary and final panel stiffness were captured by the models. The predictions for the thinner gauge sheet (0.81mm) were particularly close to the measured values, while the thicker gauges (0.93 and 1.0mm AA6111) were not as close. Upon detailed inspection, it appears that, for each model, the oil-canning load at the transition between initial and secondary stiffness regions has not been predicted well.

Close scrutiny of Figures 6.12 through 6.20 shows that the initial stiffness of each test has been predicted quite well. This suggests that the panel sheet thickness, curvature and the modulus of elasticity were not in error, as these properties are known to affect the initial stiffness of a panel as stated by van Veldhuizen *et al.* [1]. Once oil-canning in the panel occurs, the deformation becomes a complex function of panel stiffness, curvature and material yield strength. At this point it is interesting to note that for each of the load displacement curves shown in Figures 6.12 through 6.20, the slope of each secondary stiffness region has also been captured. This suggests that accurately predicting the onset of the transition between initial and secondary stiffness regions is paramount to obtaining good static dent results.

At this stage in the research, it was decided not to pursue more accurate prediction of the onset of oil-canning. Numerical predictions of such instabilities are notoriously sensitive to meshing and other numerical parameters. The approach taken was to use the “best available” material data and forming modelling results and avoid “numerical tuning” of the predictions. Improvements to the predictions of oil-canning are left for future studies.

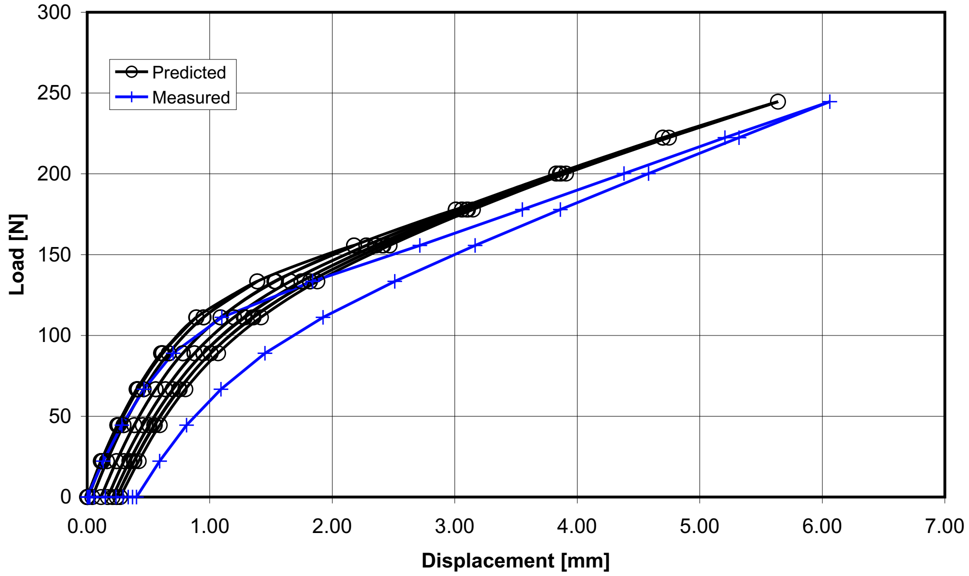

Figure 6.12: Predicted and measured load displacement curves for the 0.81mm AA6111 panel at location A.

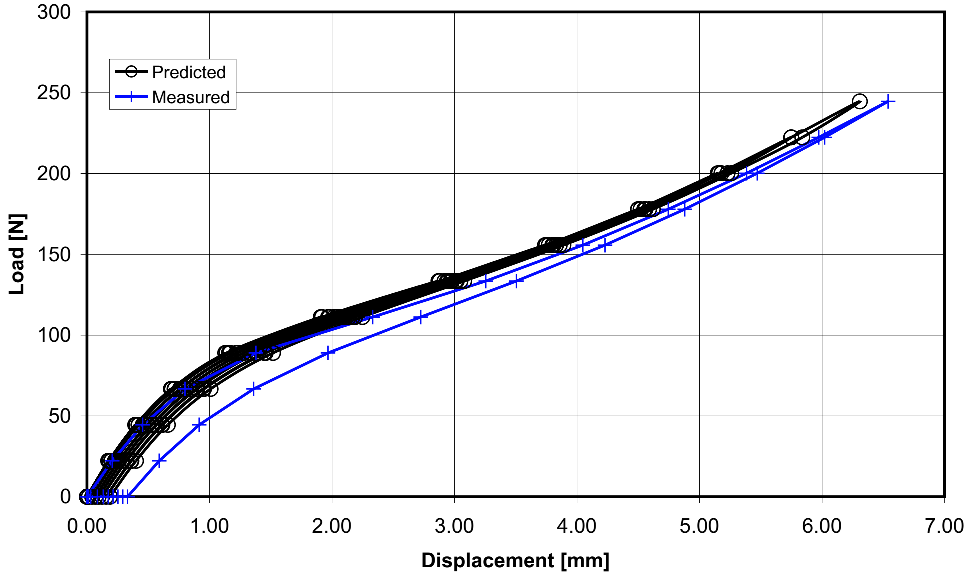

Figure 6.13: Predicted and measured load displacement curves for the 0.81mm AA6111 panel at location B.

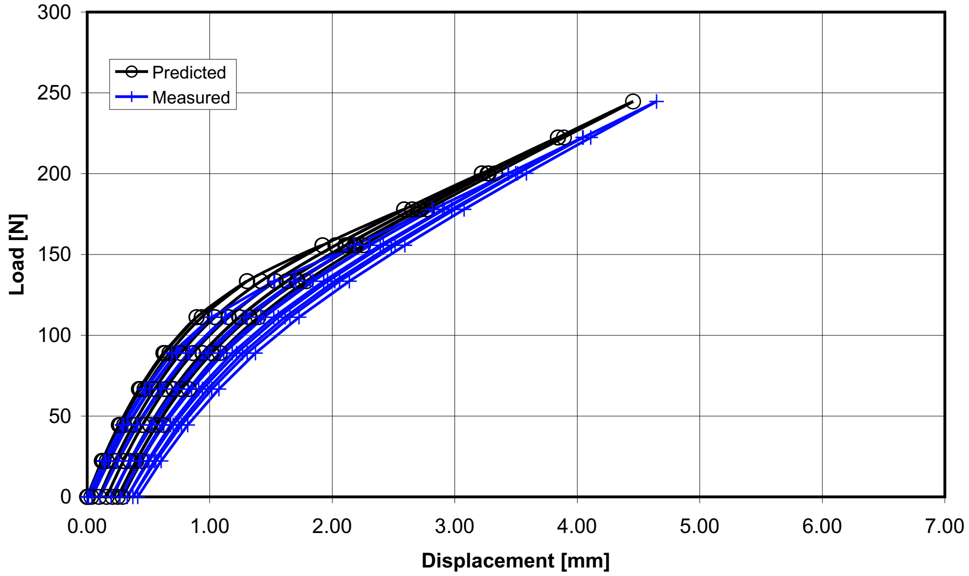

Figure 6.14: Predicted and measured load displacement curves for the 0.81mm AA6111 panel at location C.

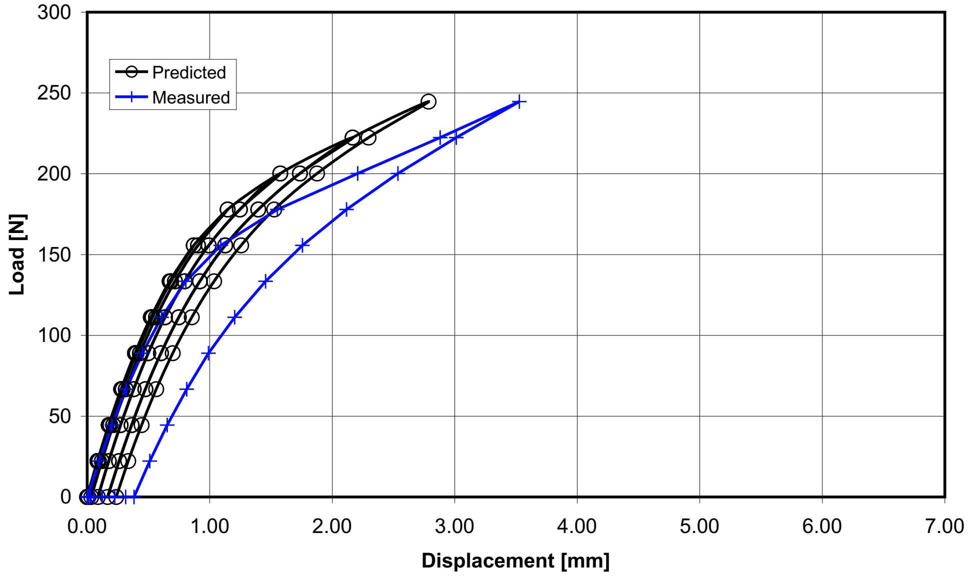

Figure 6.15: Predicted and measured load displacement curves for the 0.93mm AA6111 panel at location A.

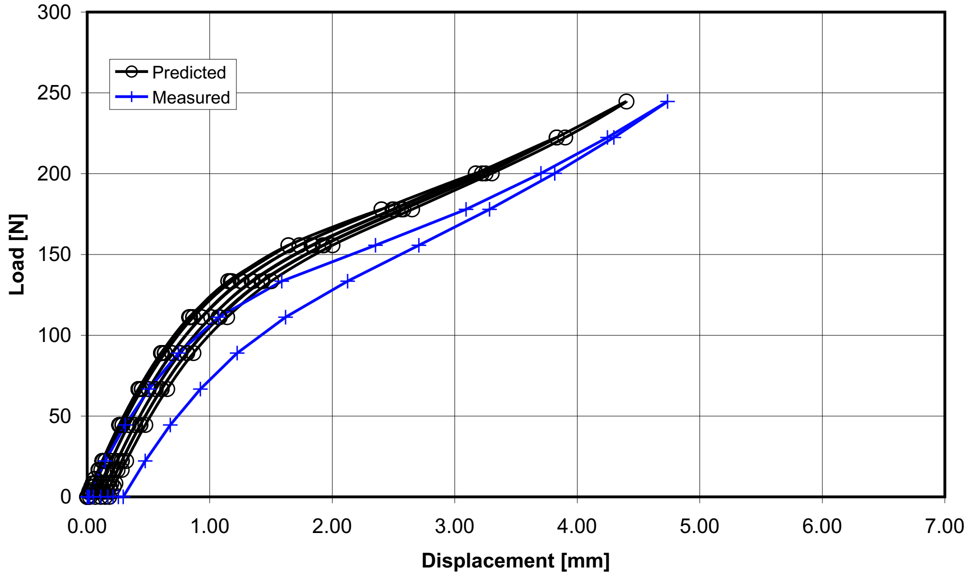

Figure 6.16: Predicted and measured load displacement curves for the 0.93mm AA6111 panel at location B.

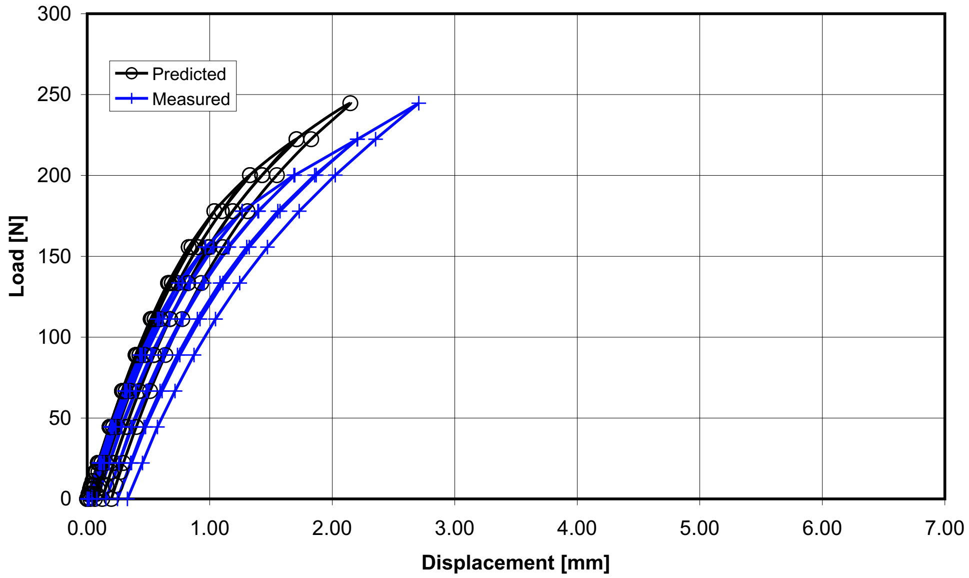

Figure 6.17: Predicted and measured load displacement curves for the 0.93mm AA6111 panel at location C.

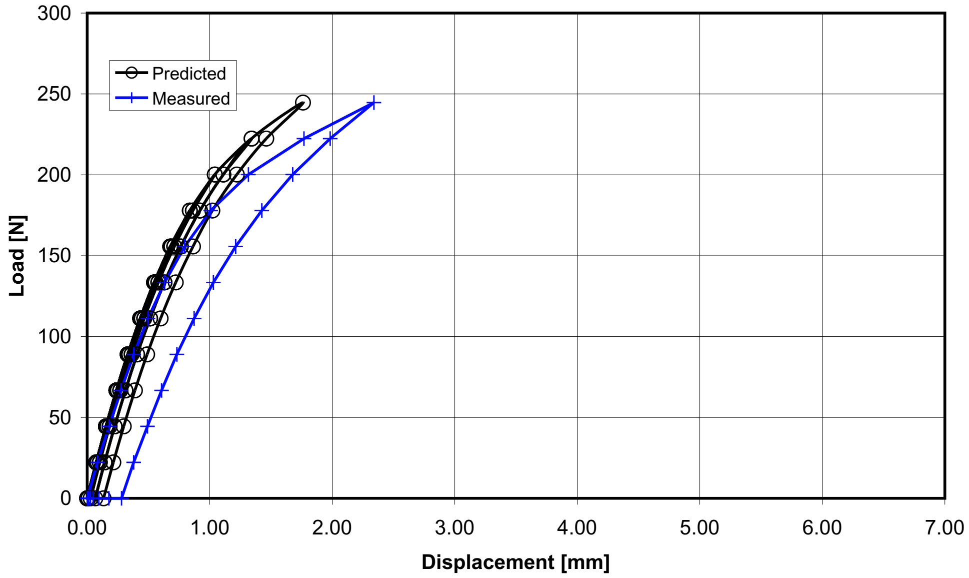

Figure 6.18: Predicted and measured load displacement curves for the 1.00mm AA6111 panel at location A.

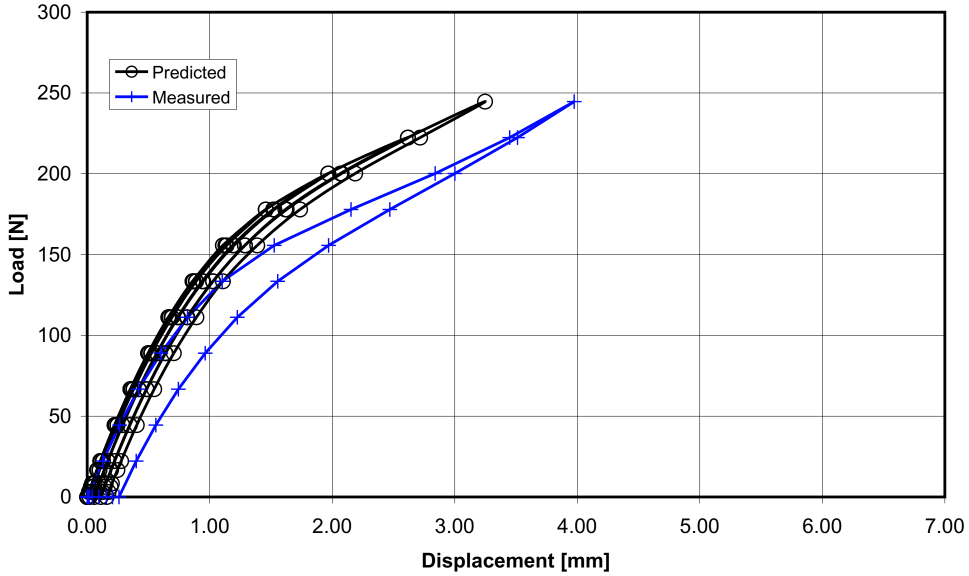

Figure 6.19: Predicted and measured load displacement curves for the 1.00mm AA6111 panel at location B.

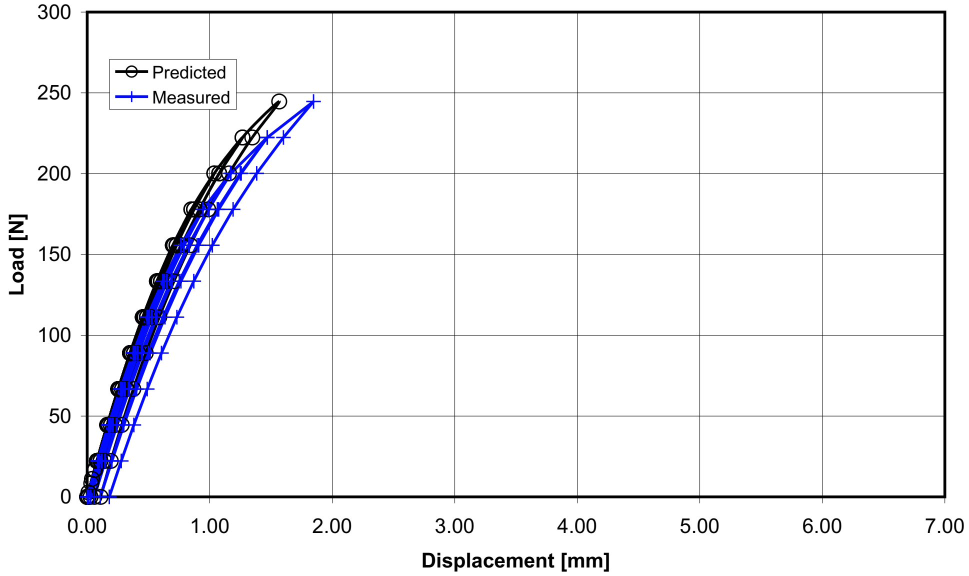

Figure 6.20: Predicted and measured load displacement curves for the 1.00mm AA6111 panel at location C.

6.2.3 Panel Stiffness

Tabulated values of measured and predicted initial panel stiffness are given in Table 6.4. The stiffness values in this table are calculated from the load-displacement plots discussed in the Sections 6.2.1 and 6.2.2. In all cases, the initial stiffness is over predicted by the finite element models. The mean over-prediction of stiffness was 26N/mm, which corresponds to an average error of 14%. One expects the panels to be numerically stiff when compared to the experiments because during the experiments, as each weight is loaded onto the loading arm, a small impulsive load is applied through the loading arm to the indentor when the weight is released. This impulsive load is in addition to the weight being applied and causes the panel to settle an extra amount. Careful handling of the weights minimised this effect; however, a displacement of 0.03mm is sufficient to cause this error. Considering the size of the panel, it is plausible that the placement of the weights could have caused this small error. In addition, the finite element simulation uses numerous nodal constraints to model clamping of the panel to the loading platform. The toggle clamps that were used during the experiments are marginally less rigid than the nodal constraints and so allow the panel to settle slightly during loading.

For the test sites that exhibited a clear secondary stiffness region, comparisons of the predicted and measured secondary stiffness values are given in Table 6.5. The 1.0mm panel was quite strong and a well-defined secondary stiffness region was not noted for locations A and C, the stiffest locations on the panel. Overall, the secondary stiffnesses were well predicted by the finite element models, the average error on secondary stiffness was only 2.1N/mm, or 5%. Only three of the test sites exhibited a final panel stiffness region. Comparisons of the predicted and measured final stiffness values are given in Table 6.6. The final stiffness values were also well predicted, the average error was 2.5N/mm, or 6%.

Table 6.4: Predicted and measured values of initial panel stiffness at the different locations tested on the IRDI panels.

Panel	**Loc.**	**Initial Stiffness [N/mm]**		**Error w.r.t. Measured Values**	
		Predicted	**Measured**	**[N/mm]**	**[%]**
1.05mm AA5754	**A**	292	259	33	13
	B	182	148	34	23
	C	276	253	23	9
	D	264	232	32	14
	E	216	193	23	12
0.81mm AA6111	**A**	182	157	24	16
	B	113	98	15	16
	C	172	156	16	10
0.93mm AA6111	**A**	253	220	33	15
	B	170	143	26	18
	C	243	233	10	4
1.00mm AA6111	**A**	290	249	42	17
	B	198	168	30	18
	C	272	254	18	7

6.2.4 Residual Dent Depths for the AA5754 panels.

Using the static dent test data, graphs of residual dent depth (after unloading) versus peak applied load can be obtained. Figures 6.21 through 6.25 show a comparison of the predicted and measured residual dent depths for the AA5754 panels at locations A through E. Again, there is remarkably good agreement between the predicted and measured values. Considering that each panel measures approximately 700mm by 500mm, the agreement of the predicted dent depths to within 0.03mm of the measured values can be considered quite good.

Recall that a commonly accepted measurement of static dent resistance is the ability of a panel to support a load prior to a dent of 0.1mm occurring. With this definition, it can be said that location C on the panel had the highest dent resistance. This location was able to support a load of 163N

Table 6.5: Predicted and measured values of secondary panel stiffness at the different locations tested on the IRDI panels.

Panel	**Loc.**	**Secondary Stiffness [N/mm]**		**Error w.r.t. Measured Values**	
		Predicted	**Measured**	**[N/mm]**	**[%]**
1.05mm AA5754	**A**	49.0	44.8	4.1	9
	B	30.7	33.7	-3.0	-9
	C	51.1	51.3	-0.2	0
	D	40.0	42.9	-2.9	-7
	E	39.3	40.7	-1.4	-3
0.81mm AA6111	**A**	26.2	26.3	-0.1	-1
	B	25.7	25.0	0.7	3
	C	35.3	35.7	-0.4	-1
0.93mm AA6111	**A**	36.8	33.8	3.0	9
	B	29.1	29.0	0.1	0
	C	54.2	46.3	7.9	17
1.00mm AA6111	**B**	34.8	33.9	0.9	3

Table 6.6: Predicted and measured values of final panel stiffness at location B on the IRDI panels.

Panel	**Loc.**	**Final Stiffness [N/mm]**		**Error w.r.t. Measured Values**	
		Predicted	**Measured**	**[N/mm]**	**[%]**
1.05mm AA5754	**B**	40.9	44.3	3.4	8
0.81mm AA6111	**B**	38.4	38.5	0.2	-
0.93mm AA6111	**B**	43.0	39.0	4.0	10

prior to a dent depth of 0.1mm occurring. Location B had the lowest dent resistance, with a permanent dent occurring at 139N. It is interesting to note that the locations that had the highest static dent resistance (Locations A and C) were also the stiffest locations on the panel. This trend is in agreement with results from Yutori *et al.* [6] and van Veldhuizen *et al.* [1].

6.2.5 Residual Dent Depths for the AA6111 Panels.

Comparisons of the predicted and measured residual dent depths versus peak applied load for the AA6111 panels are shown in Figures 6.26 through 6.34. The finite element models consistently underpredict the dent depth in each case. This is undoubtably due to over prediction of the oil-canning load for each of the panels. The magnitude of error is at most 0.15mm, which is quite small compared to the size of the panels (700mm by 500mm).

Figure 6.35 shows the residual dent depths obtained from the experiments performed on the 0.81, 0.93 and 1.00mm AA6111 panels at location A. This figure shows how an automotive panel can be tailored to pass a required performance specification. In all cases, increasing the panel thickness resulted in better static dent performance of the panel; however, if the panel was required to support a 150N load prior to a permanent dent of 0.1mm occurring, then the 0.81mm gauge sheet would be too thin.

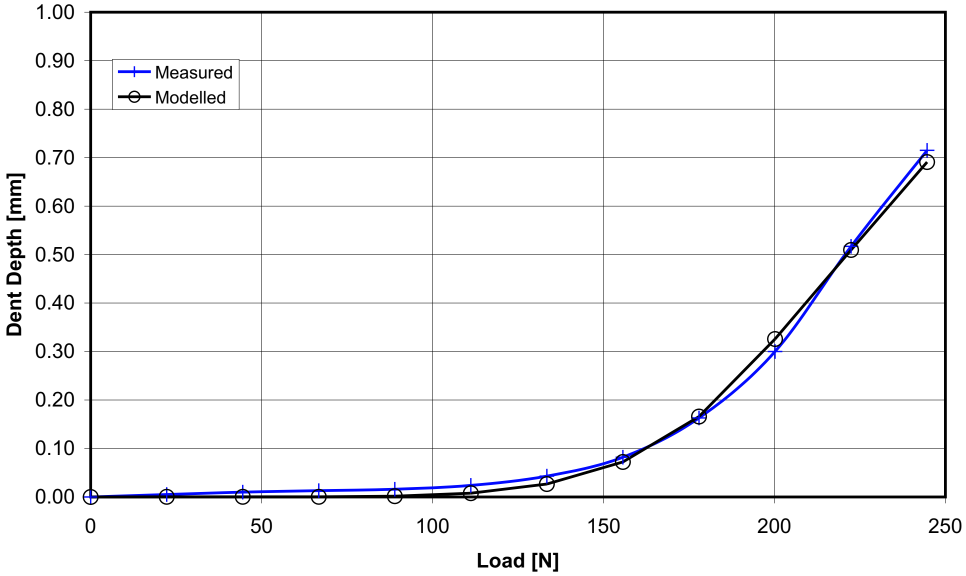

Figure 6.21: Predicted and measured residual dent depths for the 1.05mm AA5754 panel at location A.

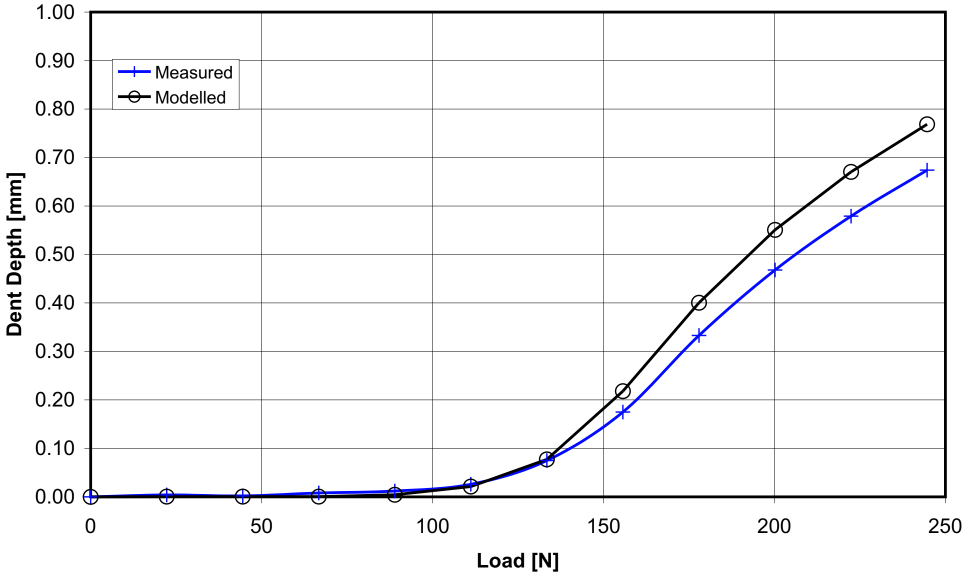

Figure 6.22: Predicted and measured residual dent depths for the 1.05mm AA5754 panel at location B.

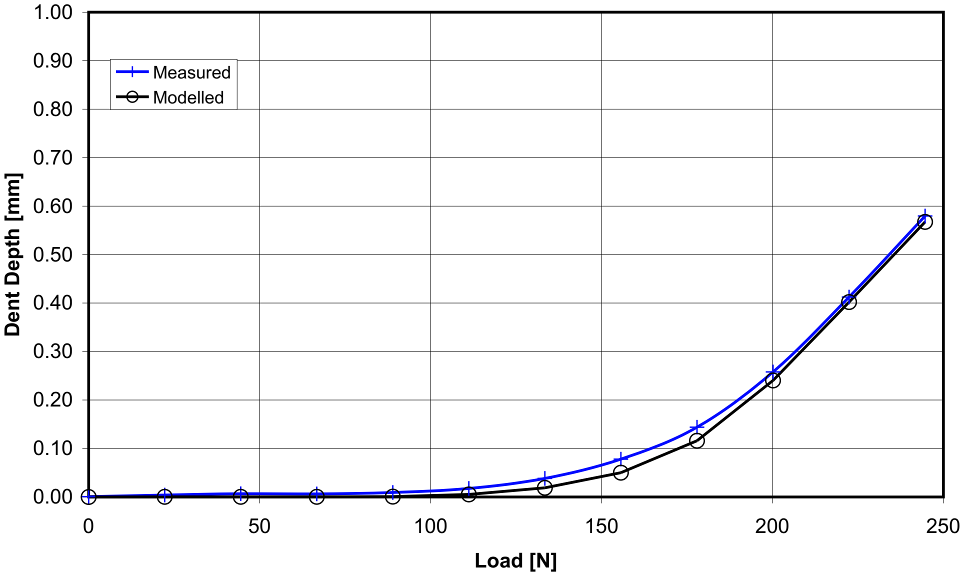

Figure 6.23: Predicted and measured residual dent depths for the 1.05mm AA5754 panel at location C.

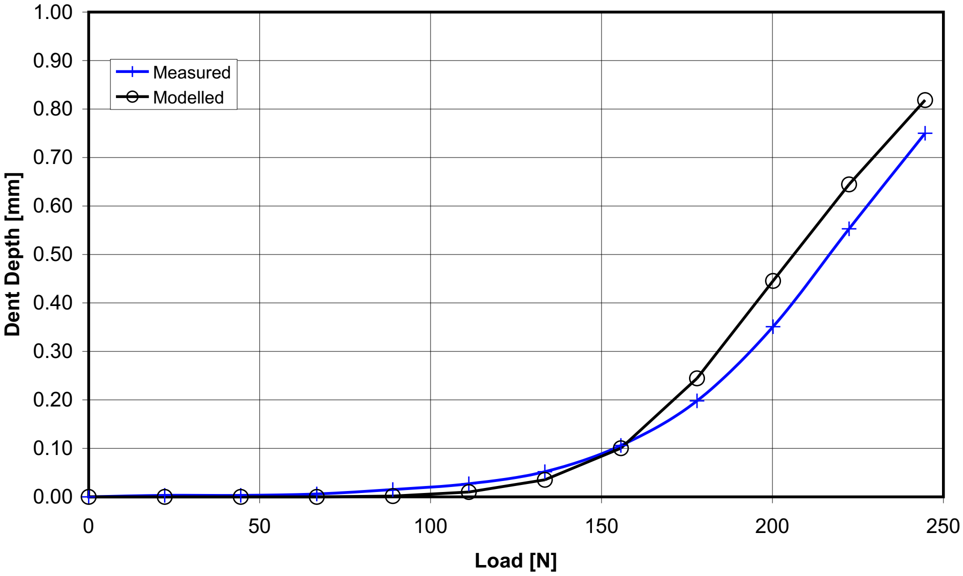

Figure 6.24: Predicted and measured residual dent depths for the 1.05mm AA5754 panel at location D.

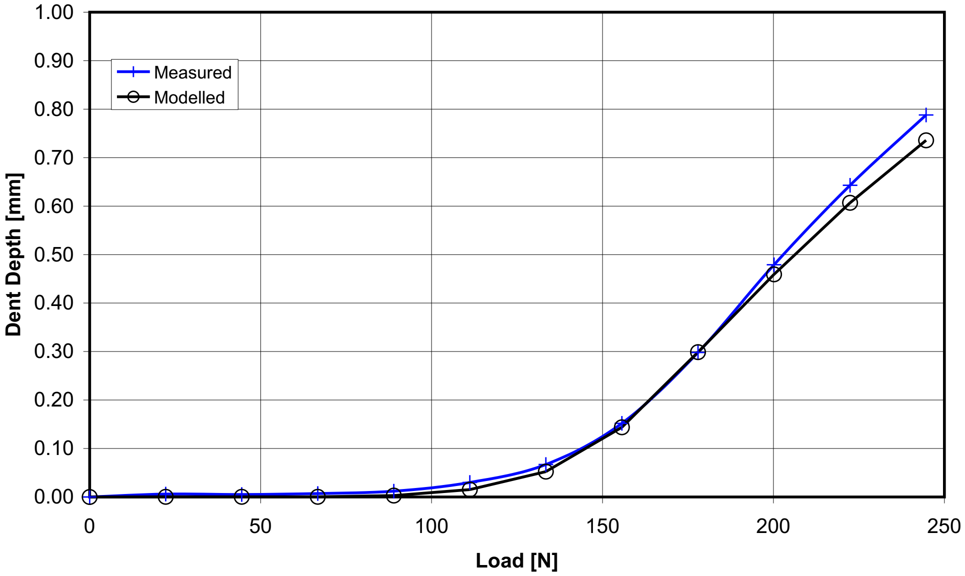

Figure 6.25: Predicted and measured residual dent depths for the 1.05mm AA5754 panel at location E.

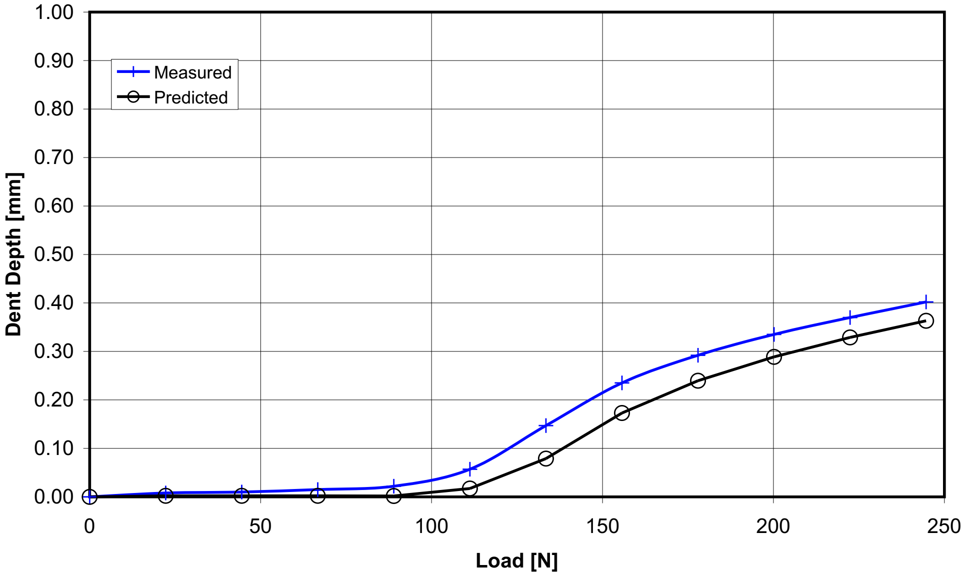

Figure 6.26: Predicted and measured residual dent depths for the 0.81mm AA6111 panel at location A.

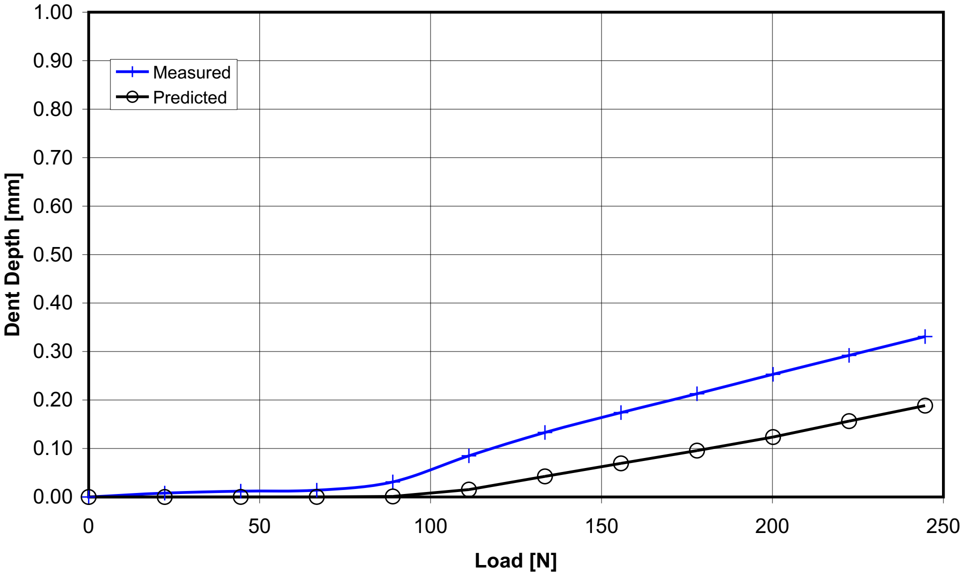

Figure 6.27: Predicted and measured residual dent depths for the 0.81mm AA6111 panel at location B.

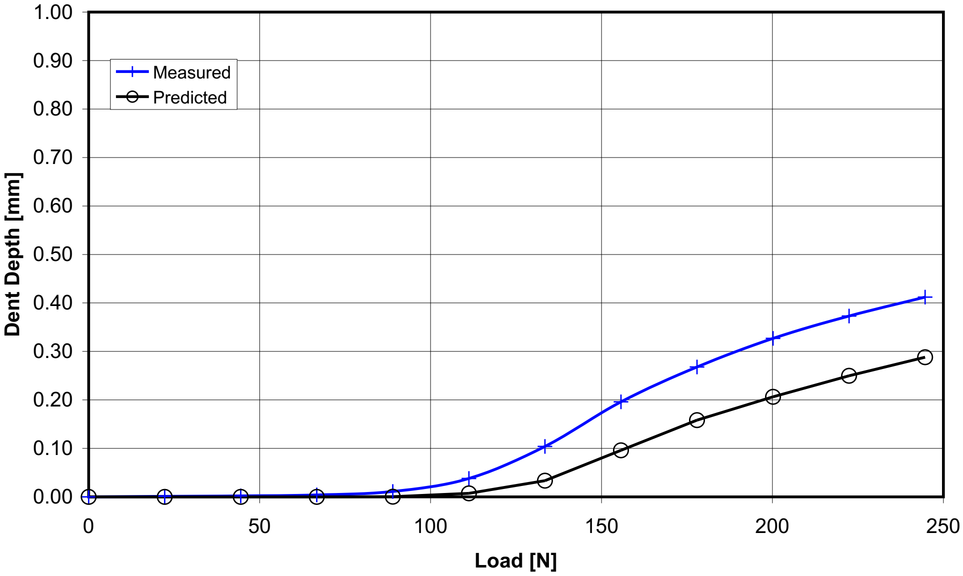

Figure 6.28: Predicted and measured residual dent depths for the 0.81mm AA6111 panel at location C.

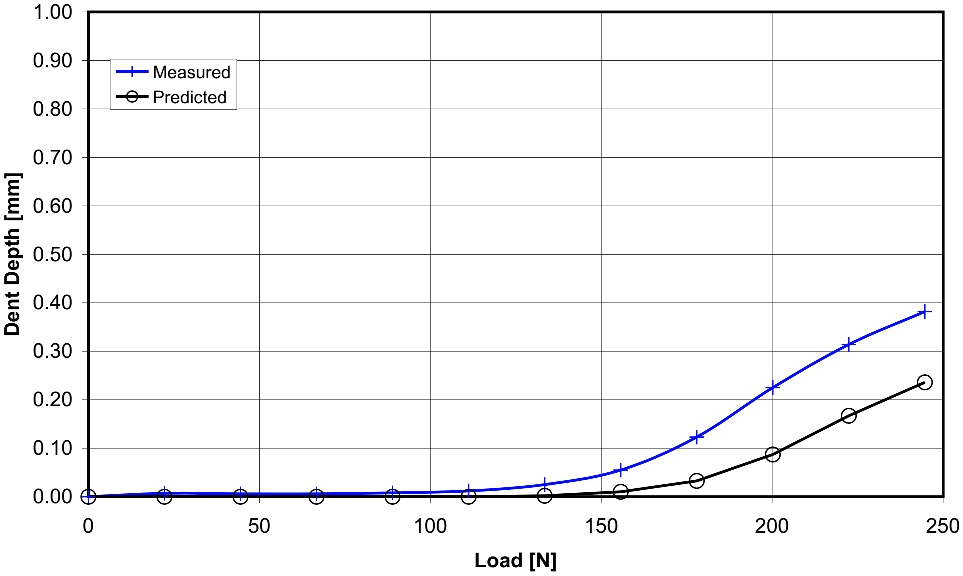

Figure 6.29: Predicted and measured residual dent depths for the 0.93mm AA6111 panel at location A.

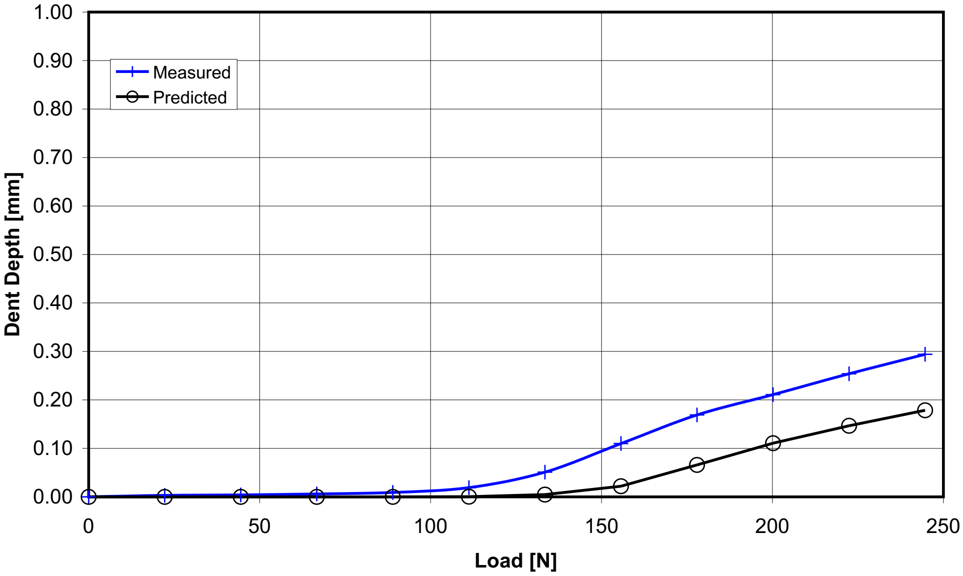

Figure 6.30: Predicted and measured residual dent depths for the 0.93mm AA6111 panel at location B.

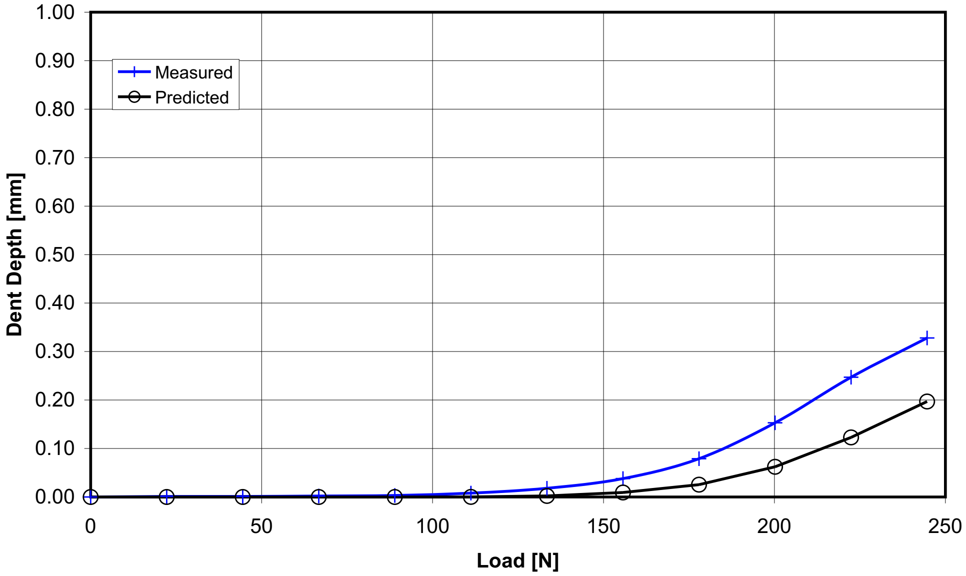

Figure 6.31: Predicted and measured residual dent depths for the 0.93mm AA6111 panel at location C.

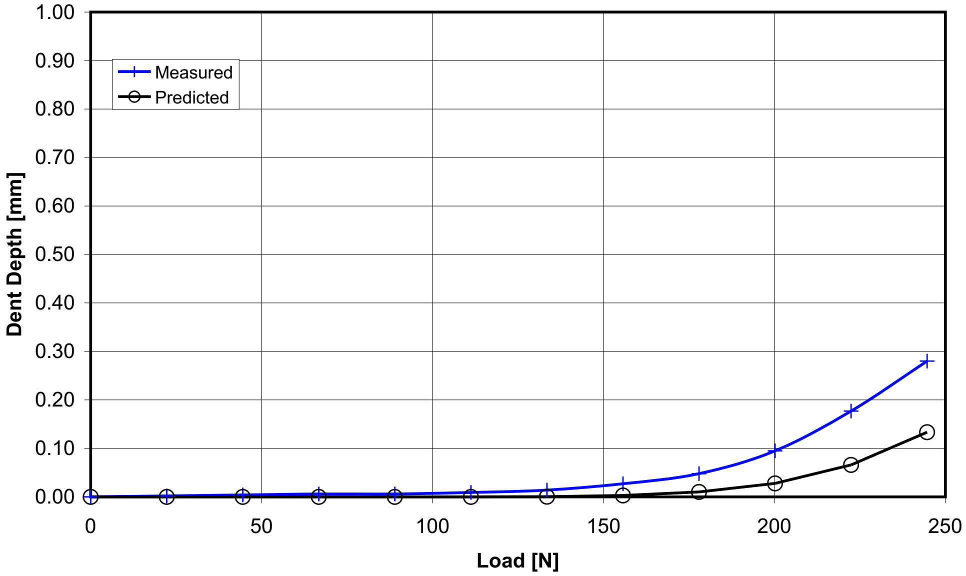

Figure 6.32: Predicted and measured residual dent depths for the 1.00mm AA6111 panel at location A.

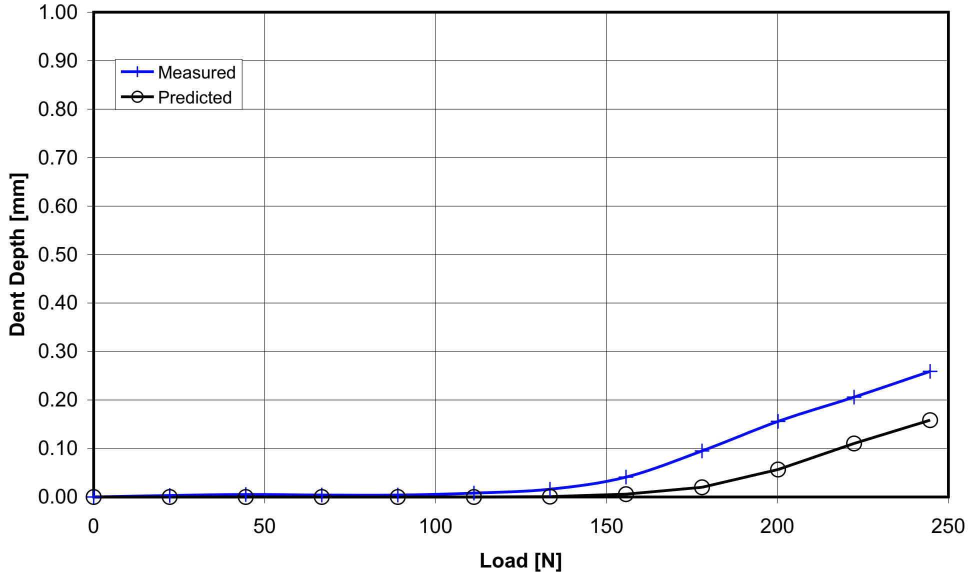

Figure 6.33: Predicted and measured residual dent depths for the 1.00mm AA6111 panel at location B.

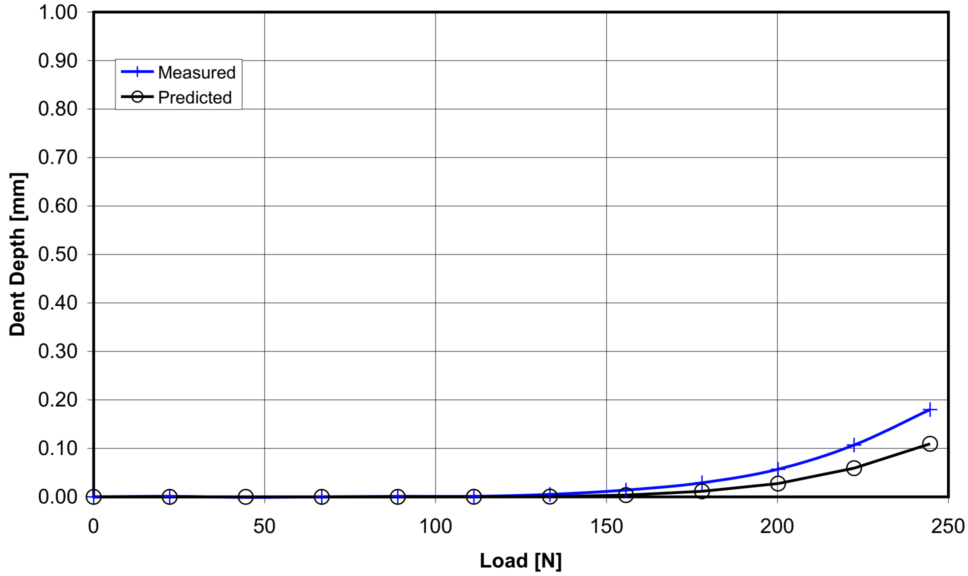

Figure 6.34: Predicted and measured residual dent depths for the 1.00mm AA6111 panel at location C.

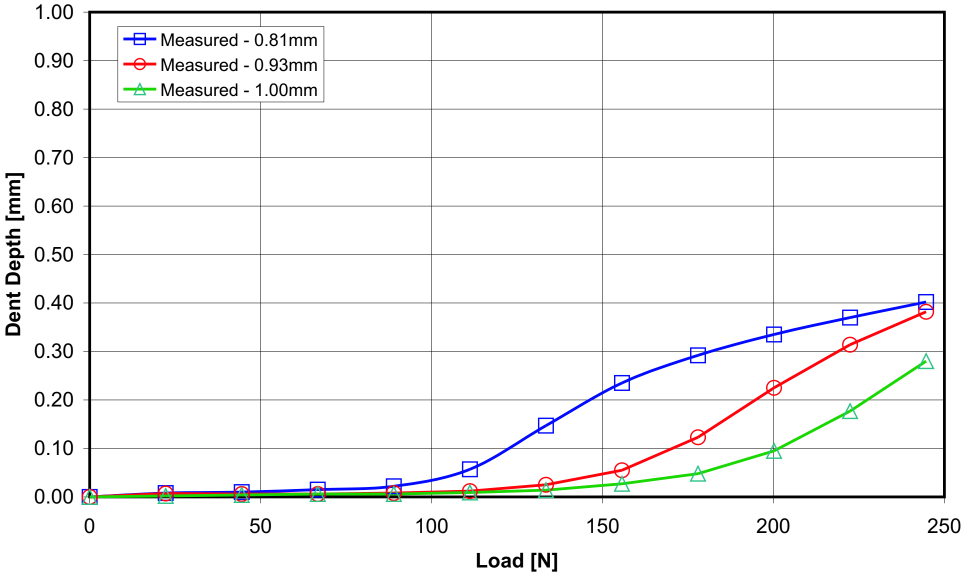

Figure 6.35: Measured residual dent depths for the 0.81, 0.93 and 1.00mm AA6111 panels at location A.

6.3 Dynamic Dent Tests

6.3.1 Dynamic Dent Response of the AA5754 panels.

The predicted and measured dynamic dent test results for the 1.05mm AA5754 panels are shown in Figure 6.36. The trend of dent depth increasing linearly with impact velocity is well captured with each of the simulations. This is a known trend that has been recorded by several previous studies [12–17]. The relative difference between dents performed at different panel locations has also been captured. Dent depths were lowest at location B, as this was the least stiff panel location. Locations A and C had quite similar initial stiffness regions as shown in Figures 6.7 and 6.9; however, the dents produced at location C were visibly smaller. This is a result of the slightly higher plastic straining during forming and resultant higher strength at location C than A.

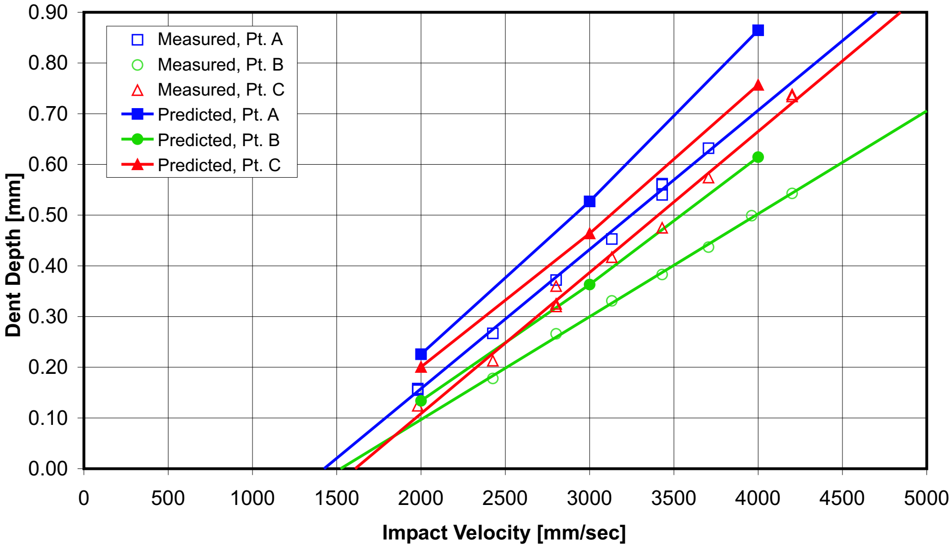

Figure 6.36: Predicted and measured dynamic dent depths for the 1.05mm AA5754 panel at locations A,B and C.

In general, the measured dynamic dent depths were over-predicted by about 0.1mm. This discrepancy is attributed to the 0.050mm difference in sheet thickness between the value of 1.000mm assumed in the forming simulation and the actual value of 1.050mm. Although this seems like a small difference, prior studies [10] have stated that the dynamic dent depth produced in a panel is proportional to thickness squared. A scaling law can be developed combining equations 1.8 and 1.9, that can be used to compare dynamic dents produced on panels of equal curvature, stiffness and yield strength but differing thicknesses. This scaling law is:

$$D_2 = \frac{D_1 t_1^2}{t_2^2} \tag{6.1}$$

Here D_1 is the dent depth produced on a panel of thickness t_1 and D_2 is the dent produced on a panel of thickness t_2. Consider, for example, the measured dent depth of 0.707mm obtained from a 4 m/s dynamic dent on the 1.05mm AA5754 panel at location A (see Figure 6.36). The final thickness of the 1.050mm AA5754 panel after forming was actually 1.030mm; however, the denting simulation used 0.975mm from the forming model. Substituting $t_1 = 1.030$mm, $t_2 = 0.975$mm and $D_1 = 0.865$mm gives a corrected dent depth (D_2) of 0.775mm. This corrected value is considerably closer to the measured dent depth (0.707mm) than the original prediction of 0.865mm. Thus, while it was decided not to rerun the calculations for the 1.05mm AA5754 panels, these results serve to emphasise the importance of accounting for panel thickness changes during forming and to use actual panel thicknesses rather than nominal values.

6.3.2 Dynamic Dent Response of the AA6111 panels.

The predicted and measured dynamic dent test results for the 0.81, 0.93 and 1.00mm AA6111 panels are shown in Figures 6.37, 6.38 and 6.39, respectively. The dynamic dent predictions for the AA6111 panels are much closer to experiment than those predicted for AA5754. This is attributed in part to better prediction of panel thickness and strain during the forming simulations. Overall, the AA6111 panels exhibited much better dynamic dent resistance than the AA5754 panels, due to the higher strength of the AA6111.

Figure 6.37 for the 0.81mm AA6111 panel shows an interesting change in slope for the predicted dent depths at location B. This change occurred because the 2 m/s denting simulation performed at location B did not converge during the final springback solution for the tolerances imposed for the other simulations. The convergence criterion used by LS-DYNA (given in equation 5.5) does not allow convergence in springback problems with very small displacements. Convergence will never occur when the Euclidean norm of the displacements ($\|\Delta\bar{\mathbf{u}}_i\|$) is less than the maximum displacement ($\bar{\mathbf{u}}_{max}$) multiplied by a convergence tolerance (ϵ_d). This situation occurred at location B, so the tolerance on displacement (ϵ_d) had to be increased from 0.001 to 0.005, which resulted in a less precise solution. Note how this combination of panel location (B) and thickness (0.81mm) was the least stiff of all the tested configurations (see Tables 6.4 and 6.5). This combination produced the lowest dynamic dent depths, but relatively large static dent depths, which highlights the competitive role that stiffness plays in static and dynamic denting.

Figures 6.40, 6.41 and 6.42 show the effect of increasing sheet thickness at each of the dent locations. General trends are observable for the stiff panel locations (Locations A and C), but not at the less stiff location (B). For the stiffer panels, at lower impact velocities, increased thickness aids dynamic dent resistance, but at higher impact velocities, increased sheet thickness hinders dynamic dent resistance. This trend is in agreement with results of Nomura *et al.* [18] who concluded that increased sheet thickness did not necessarily improve dynamic dent resistance. Thus when designing automotive panels for dynamic dent resistance, increasing sheet thickness may not have the desired effect, depending on the indentor velocity and sheet curvature. It also may have minimal effect if the panel is not very stiff as shown by Figure 6.41.

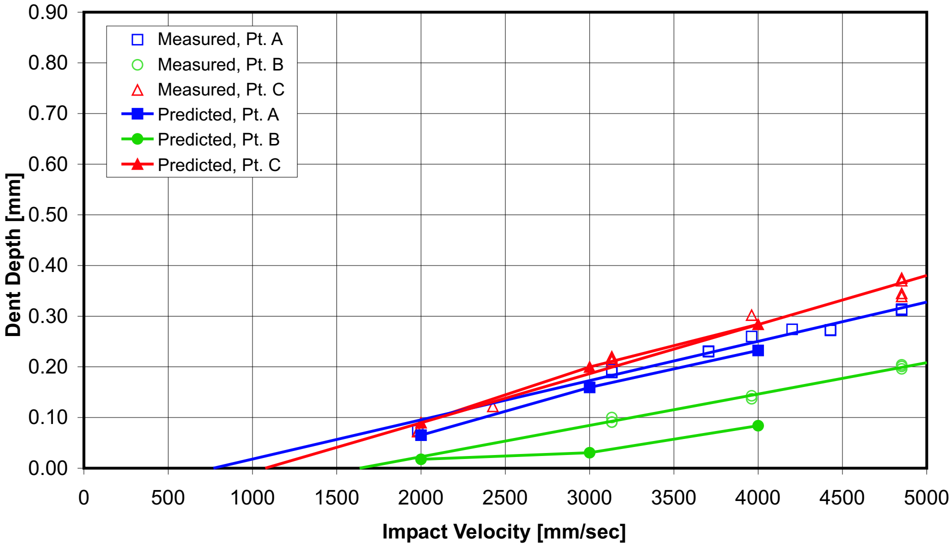

Figure 6.37: Predicted and measured dynamic dent depths for the 0.81mm AA6111 panel at locations A,B and C.

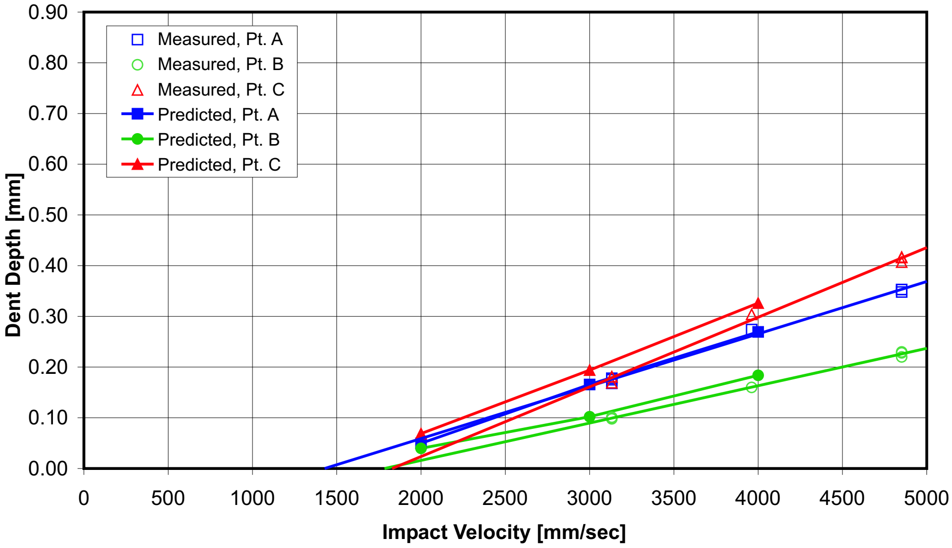

Figure 6.38: Predicted and measured dynamic dent depths for the 0.93mm AA6111 panel at locations A,B and C.

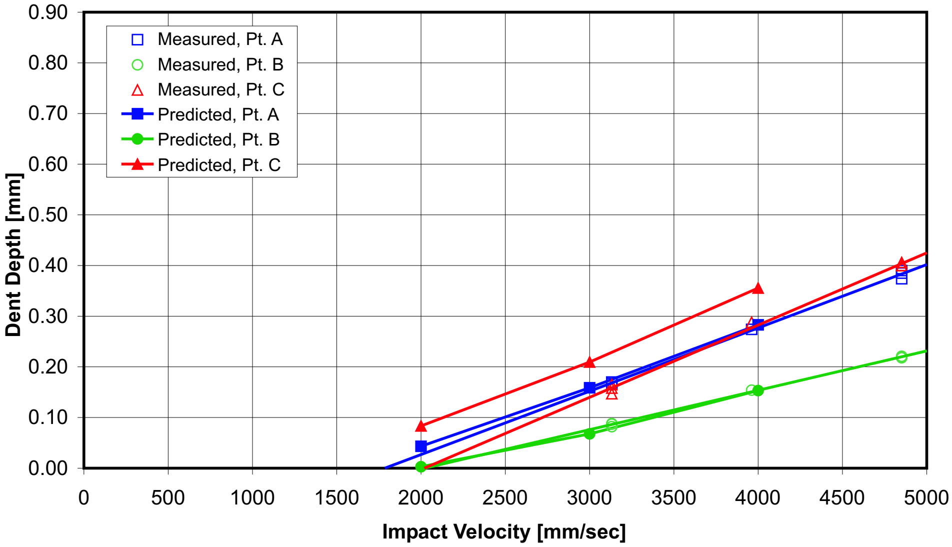

Figure 6.39: Predicted and measured dynamic dent depths for the 1.00mm AA6111 panel at locations A,B and C.

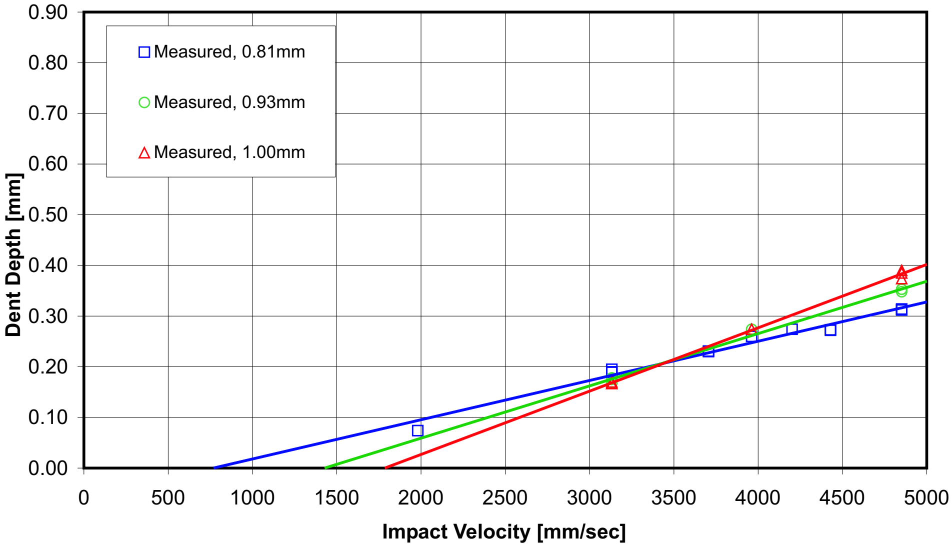

Figure 6.40: Measured dynamic dent depths for the 0.81, 0.93 and 1.00mm AA6111 panel at location A.

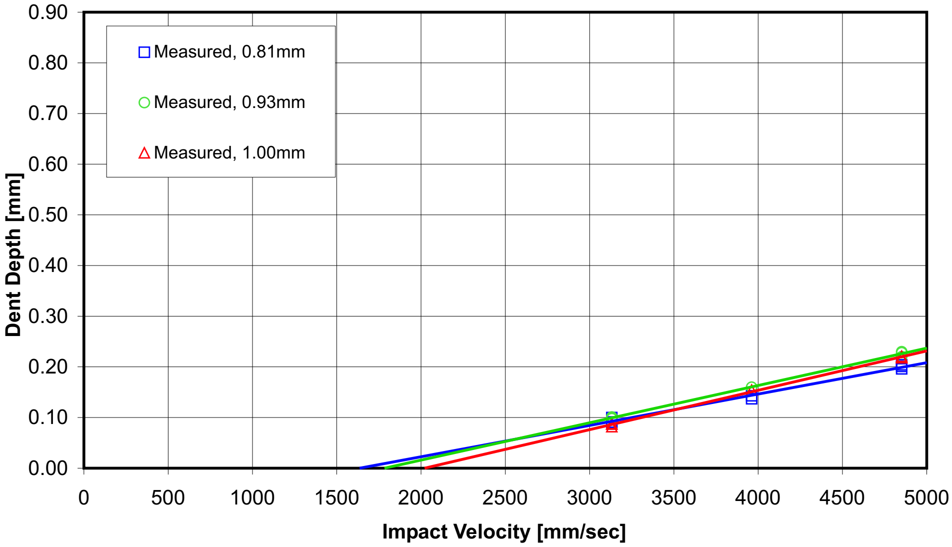

Figure 6.41: Measured dynamic dent depths for the 0.81, 0.93 and 1.00mm AA6111 panel at location B.

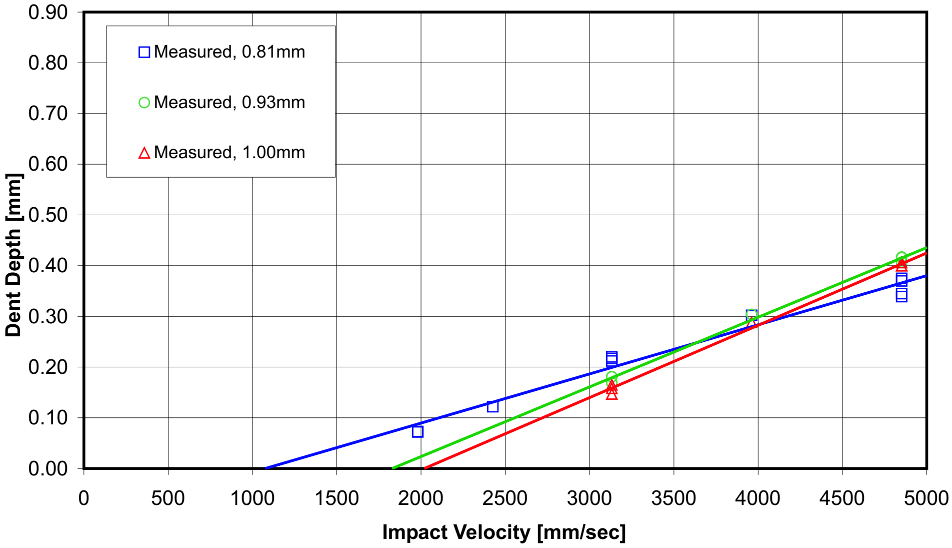

Figure 6.42: Measured dynamic dent depths for the 0.81, 0.93 and 1.00mm AA6111 panel at location C.

6.3.3 Sensitivity of the Dynamic Denting Results to Finite Element Model Parameters.

A series of finite element models were run to gain an understanding of how sensitive the results were to modelling parameters. It has already been shown that material thickness plays a very important role in obtaining good dynamic dent predictions. Many other factors such as element formulation, material yield function, mesh size and refinement radius, indentor position and residual stresses can also have an effect and were considered in this sensitivity study. Figure 6.43 shows the effect that each of these parameters had on the predicted dent depth for a 1.05mm AA5754 panel dented at location A for an initial velocity of 4 m/s. For comparison purposes, the measured dent depth for this case was 0.707mm.

6.3.3.1 Sensitivity to Element Formulation.

The choice of element formulation used in the finite element model had the largest effect on predicted dent depth. Use of the reduced integration Belytschko - Tsay shell element [61] resulted in a dent depth of 1.110mm, which represents an over prediction by 0.403mm, as shown by the result for finite element model number 1 in Figure 6.43. This element formulation is widely used in sheet metal forming simulations due to its numeric efficiency; however, it was not sufficiently accurate for the current work. This led to a trial of the non-reduced integration element formulated by Hughes and Liu [63]. This element formulation also overpredicted dent depth (0.919mm for model number 2 in Figure 6.43). The number 16 element formulation available within LS-DYNA [68] was recommended for use during this study by Maker [78]. This element produced dent predictions consistently closer to the measured value than the other shell element choices, as shown by models labelled 3 to 8 in Figure 6.43.

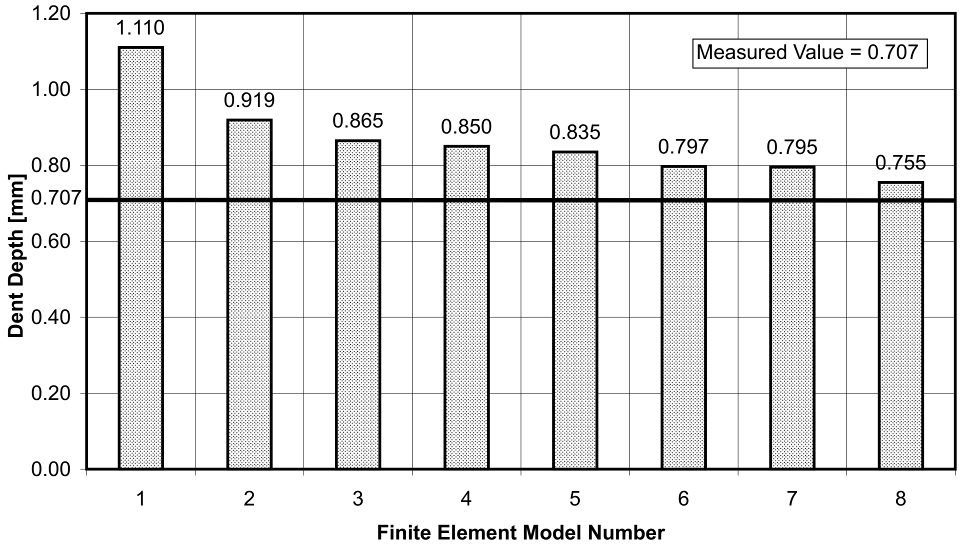

Model Number	Element Type	Hardening Rule	Mesh Size and Refinement Radius	Position of Indentor	Residual Stresses
1	Belytschko - Tsay	3-Paramater Barlat	1mm, 30 mm	0.2 mm above	Yes
2	Hughes - Liu	3-Paramater Barlat	1mm, 30 mm	0.2 mm above	Yes
3	Element 16	3-Paramater Barlat	1mm, 100 mm	0.2 mm above	Yes
4	Element 16	von - Mises	1mm, 100 mm	0.2 mm above	Yes
5	Element 16	von - Mises	1mm, 30 mm	0.2 mm above	Yes
6	Element 16	3-Paramater Barlat	1mm, 30 mm	0.2 mm above	Yes
7	Element 16	3-Paramater Barlat	1mm, 30 mm	0.7 mm above	Yes
8	Element 16	3-Paramater Barlat	1mm, 30 mm	0.2 mm above	No

Figure 6.43: This figure shows the sensitivity of the dynamic denting models to element formulation, material yield function, mesh size, location of the indentor above the panel and use of residual stresses. These results were obtained from 4 m/s dents simulated at point A on the 1.05mm AA5754 panel.

6.3.3.2 Sensitivity to Material Yield Function and Mesh Size.

Two material yield functions were considered for use in the finite element models. These were an isotropic von-Mises yield function and the anisotropic 3-Parameter Barlat yield function. Both of these yield functions are discussed in Chapter 5. Dent depths of 0.850mm and 0.835mm were obtained using the von-Mises Yield function (see models 4 and 5 in Figure 6.43). The result for model number 4 was obtained using a small refinement radius of 30mm, while the result from model number 5 used a larger refinement radius of 100mm. All other models in Figure 6.43 used the 3-Parameter Barlat yield function. Comparison of the yield functions can be made by either model 4 to model 3 or model 5 to model 6. In the first comparison (models 3 and 4), the use of the von-Mises yield criteria resulted in a dent depth prediction that is closer to the measured value, while in the second comparison the opposite is true. The lack of a general trend is likely a combined effect of mesh refinement and choice of material yield function.

Models 4 and 5 required switching material yield functions after the first springback step. Without considering the dent, switching the yield function after the first springback step could result in slightly different equilibrium position for the panel obtained during the final springback solution. Mesh refinement compounds this issue by introducing an averaged stress distribution in the refined elements, which also causes a slight difference in the equilibrium position of the panel prior to denting.

Even though model 3 in Figure 6.43 shows that the combination of a 3-Parameter Barlat yield function and wide radius of refinement did not produce a predicted dent in better accord with the measured values, these modelling parameters were adopted in the current study as they represent "best practice". The 3-Parameter Barlat yield function was chosen to help match the material thinning during forming, which was deemed very important. The larger refinement radius was chosen for consistency with the static dent models and to avoid mesh sensitivity issues, even though it produced a larger dent depth in this particular case.

6.3.3.3 Sensitivity to Position of the Indentor.

One would generally consider that the relative position of the indentor above the panel should not affect the dynamic dent prediction. In a dynamic dent simulation, this parameter should only affect how long it takes the indentor to strike the panel, as the velocity of the indentor is constant prior to denting in the absence of gravity. However, during the dynamic dent simulations it was also observed that the panels tended to oscillate after the springback stage, prior to the indentor striking the panel. These oscillations produced negligible displacements, but velocities of the same order of magnitude as the indentor. One would expect the panel to be stationary following a springback step, so questions were drawn regarding the validity of the equilibrium state. It was determined by Maker [78] that these oscillations were very high frequency stress waves traversing the panel, an artifact of the explicit finite element formulation in LS-DYNA. These stress waves produced high velocities, but only small displacements at the nodes. As a method of determining whether these oscillations caused differences in dynamic dent predictions, two simulations were run so that the panel was struck at different times. Any differences in dent depth caused by local panel momentum effects would thus be visible. The dent depth predictions obtained from models 6 and 7, shown in Figure 6.43, are nearly identical, so these stress waves did not have an effect.

6.3.3.4 Sensitivity to Residual Stresses.

Residual stresses are present in the panel after the forming stage. The springback step allows these stresses to find an equilibrium state, which in some cases can cause large deflections. If these residual stresses did not contribute to the final dent depth, the dent simulation process could be simplified for stiff panels by foregoing springback steps. The result for model number 8 in Figure 6.43 was simulated without the residual stresses from the forming simulation, but utilised the predicted effective plastic strains (work hardening). The dent that was predicted without the use of residual stresses was 0.755mm, while the dent predicted using residual stresses was 0.797mm. This difference shows that residual stresses do have an effect on dent depth predictions and should be included in the denting simulation.

Chapter 7

Discussion and Conclusion

7.1 Discussion

A numerical method of predicting both static and dynamic dents in automotive panels has been developed. This method is centered around an integrated suite of commercial and custom software programs. This modelling system uses the finite element method as a predictive tool which enables automotive panel designers to assess performance prior to production of tooling. Experimental validation of dent predictions using this method has shown that the trends of both static and dynamic dent resistance have been captured quite well. These validations also showed the sensitivity of the results to various parameters such as panel thickness, pre-strain, curvature and thickness as well as numerical formulation parameters. It is particularly important to use forming data within the denting models for accurate results to be obtained. In this regard, the software created as part of this research is able to both refine and remap data from existing forming models for use in subsequent dent tests. This software has been particularly successful in transforming the forming models into "ready-to-run" finite element denting models, thereby minimising the effort required to perform dent simulations.

The current models have captured static and dynamic denting trends very well. In some experiments, such as the AA5754 static dents and AA6111 dynamic dents, values were predicted that were very close to those measured.

In other tests, such as the dynamic dents performed on the AA5754 panels, the predicted dent depths were larger than those measured, while in the AA6111 static tests, the dent depths were under-predicted. These errors are not unexpected considering the small size of the dent depth compared to the panel size and the numerous sources of uncertainty in the experiments. Thus, it is advisable at present to treat dent prediction as a qualitative comparison tool. Such conservatism would still permit comparison of the relative performance of different panel designs in assessments of changes in panel thickness or alloy, for example.

The resolution required in a dent test exacerbates the issue. In general, dents are determined to be visible when their depth is greater than 0.1mm. Therefore, for this method to be applicable for panel certification purposes, repeated resolution to values of less than 0.01mm are necessary. For this level of resolution, it may be necessary to consider other finite element discretisation techniques, such as several layers of brick elements in the denting region. Considering the large size of most automotive panels, the computational costs associated with such an approach are likely prohibitive. Models that were run during this work were almost unmanageable due to their size and computer hardware requirements.

Owing to the sensitivity of the results to material data, it may be necessary to obtain more accurate tensile data of the initial yield behaviour of the aluminum. The tensile data given in Chapter 3 was adequate for the forming simulation; however, the strains present in a dent are small compared to those produced during forming. The prediction of the initial yield point requires very accurate low strain data, which may have been obscured during the curve fitting technique used during the current work. This could help explain the over-prediction of the oil-canning loads in the AA6111 panels.

The choice of material yield criterion was limited by the finite element codes. Whereas LS-DYNA has several anisotropic material models, such as the 3-Parameter Barlat model, that are formulated specifically for sheet metal forming, ABAQUS does not. This necessitated the use of an isotropic von-Mises yield function for the static dent tests. Use of this isotropic yield function could have contributed to some of the discrepancy within the static dent models since a different yield locii are predicted by the two models. These yield locii are shown in Figure 7.1 for the 0.81mm AA6111-T4 material data (R00=0.62, R45=0.66, R90=0.86 and σ_y=140MPa).

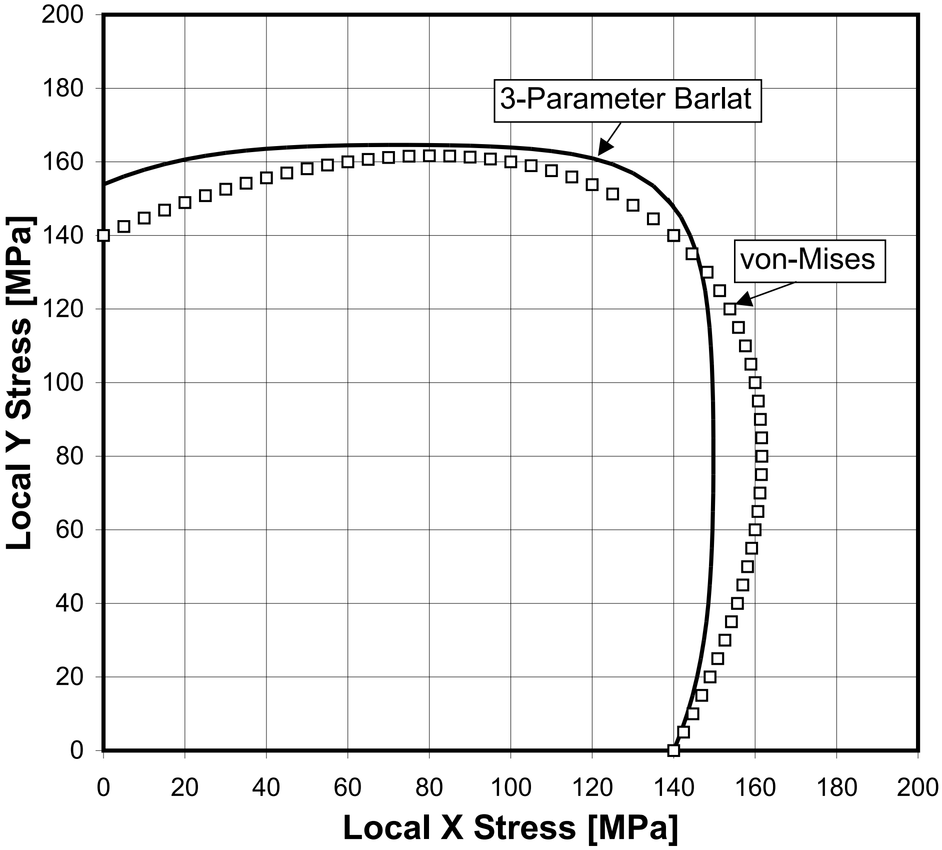

Figure 7.1: Yield locii predicted by the 3-Parameter Barlat and von-Mises yield functions for the 0.81mm AA6111-T4 material data (R00=0.62, R45=0.66, R90=0.86 and σ_y=140MPa).

Adoption of the 3-Parameter Barlat model has a further disadvantage. Although Harpell [50] has shown that the 3-Parameter Barlat material model captures sheet thinning well, Figure 7.1 highlights a deficiency of the model.

The 3-Parameter Barlat model matches the three R-values (R00, R45 and R90) and also the yield strength in the rolling direction. It does not, however, match the yield strength in material directions other than the rolling direction, such as the transverse direction. This limitation can cause under or over-prediction of the yield strength in the transverse direction, as shown when the transverse yield strength is compared to that measured during the tensile tests. In Figure 7.1 the transverse yield strength is 154Mpa, while the measured value shown in Figure 3.5 is 135Mpa. Newer material models that address this issue have been proposed by Barlat [79]; however, these models remain proprietary and are not yet available.

7.2 Conclusions

The following conclusions are drawn from this research.

- A software system which enables the automotive panel designer to quickly post-process an existing finite element forming model to generate a static or dynamic denting model has been created. This software tool set can be used to qualitatively predict both dynamic and static denting behaviour. Quantitative prediction requires greater caution and "calibration" with available experimental data.

- Both static and dynamic dents have been predicted for AA5754 and AA6111 panels. The AA6111 panels performed much better than the AA5754 panels due to their higher yield strength.

- Increasing sheet thickness will help static dent resistance, but in certain situations will hinder dynamic dent resistance. This is due to the effect that thickness has on panel stiffness. Whereas increased panel stiffness allows a higher static load to be carried by the panel prior to oil-canning, it creates larger contact forces during dynamic denting. These high contact forces cause localised deformation during a dynamic dent.

- The fully integrated shell element (number 16) was necessary to obtain repeatable convergent solutions within the springback simulations. It was also necessary to obtain reasonable dynamic dent predictions.

- During the current work it was found that the implicit LS-DYNA formulation was not robust enough to repeatedly gain convergence during static dent simulations. Moreover it did not have required boundary conditions that would enable its use for general automotive assemblies. To this end ABAQUS was used for the static dent tests. It was found that convergence of the static dent tests was repeatably achieved, without the requirement for user intervention.

7.3 Recommendations

Future work should include a mesh refinement study to determine if the accuracy of the results can be improved. This refinement should include other discretisation techniques such as solid elements. The refined denting region could be modelled with a different yield stress curve, one that only considers the strain range present in the denting region.

An improved yield surface formulation is required to accurately model the material yield strength in directions other than the rolling direction. This formulation should be used in both the implicit and explicit calculations for consistency.

This work should be extended to include complete automotive panel assemblies. In this manner, the support provided by inner panels can be included to assess the denting characteristics of the complete panel assembly.

Automating the static test apparatus would reduce the error caused by manual placement of the weights on the loading arm and would decrease the time required to perform a static dent test. Automation should follow the guidelines published in the Auto/Steel Partnership Report [34].

Bibliography

[1] Bart van Veldhuizen, Winfried Kranendonk, and Rob Ruifrok. The relation between the curvature of horizontal automotive panels, the panel stiffness and the static dent resistance. In *Materials and Body Testing IBEC'95*, pages 62–70. IBEC, 1995.

[2] Hikmat F. Mahmood. Combined shallow spherical shell and finite element method of panel stiffness. Technical Memorandum 8031, Chrysler Corporation, September 1978.

[3] A.V. Vadhavkar, M.G. Fecek, V.C. Shah, and W.E. Swenson. Panel optimization program (pop). Paper 810230, SAE, 1981.

[4] C.L. Alaniz, L.E. Brookes, and T.N. Seel. Investigation of body panel stiffness as predicted by finite element analysis. Paper 900716, SAE, 1990.

[5] J.A. DiCello and R.A. George. Design criteria for the dent resistance of auto body panels. Paper 740081, SAE, 1974.

[6] Y. Yutori, S. Nomura, I. Kokubo, and H. Ishigaki. Studies on the static dent resistance. *Memoires Scientifiques Revue Metallurgie*, 77(4):561–569, April 1980.

[7] Hikmat F. Mahmood. Dent resistance of surface panel and slam area. Paper 810099, SAE, 1981.

[8] E. Reissner. Stresses and small displacement of shallow spherical shells. *Math and Physics*, 25(24), 1947.

[9] M.A. McCormick, D.J. Meuleman J.R. Fekete, and M.F. Shi. Effect of steel strengthening mechanisms on dent resistance of automotive body panels. Paper 980960, SAE, 1998.

[10] T. E Johnson, Jr and W.O. Schaffnit. Dent resistance of cold-rolled low-carbon steel sheet. Paper 730528, SAE, 1973.

[11] M.J. Worswick, M.J. Finn, and J.J. Thorburn. A numerical study of the geometric and material parameters affecting static and dynamic denting. Internal Report KR-97/025, Alcan International Limited, Kingston Research and Development Centre, November 1997.

[12] C.E. Burley, B. A. Niemeier, and G. P. Koch. Dynamic denting of autobody panels. Paper 760165, SAE, 1976.

[13] C. E. Burley and B. A. Niemeier. Denting properties of aluminum autobody components. Paper 770199, SAE, 1977.

[14] R. L. Rolf, M. L. Sharp, and H. H. Stroebel. Structural characteristics of aluminum body sheet. Paper 770200, SAE, 1977.

[15] Bernard A. Niemeier and Carlton E. Burley. Hailstone response of body panels - real and simulated. Paper 780398, SAE, 1978.

[16] D. C. Chang and R. P. Khetan. Surface damage of steel, aluminum, and chopped-fiber composite panels due to projectile impact. *Journal of Reinforced Plastics and Composites*, 3:193–203, July 1984.

[17] Thomas N. Seel. Bake hardening steel application study - key factors of dent resistance improvement. Paper 910291, SAE, 1991.

[18] S. Nomura, Y. Yutori, J. Iwaya, M. Miyahara, and I. Kokub. A study of the dynamic dent resistance. In *IDDRG Conference Proceedings*, pages 394–402. IDDRG, 1984.

[19] Herbert J. Thorburn. Comparative tests of stiffness and dent resistance on aluminum and steel fenders. In *Automotive Body Materials IBEC'94*, pages 105–112. IBEC, 1994.

[20] Gunnar Ekstrand and Nader Asnafi. On testing of the stiffness and the dent resistance of autobody panels. *Materials and Desigh*, (19):145–156, 1998.

[21] Nader Asnafi. On strength, stiffness and dent resistance of car body panels. *Journal of Materials Processing Technology*, (49):13–31, 1995.

[22] Marcus A. Sabbagh, Ravi N. Chavali, and Jay S. Montgomery. Quasi-static dent depth simulation using non-linear fea. In *IBEC '95 Materials and Body Testing*, pages 87–90. IBEC, 1995.

[23] Jay Montgomery and Alan Brooks. Influence of geometry on outer panel dent resistance as demonstrated through fea. In *IBEC '94 Automotive Body Materials*, pages 85–89. IBEC, 1994.

[24] Mark F. Werner. Finite element simulation of steel body panel performance for quasi-static dent resistance. In *IBEC '93 Automotive Body Materials*, pages 87–90. IBEC, 1993.

[25] Kuo-Kuang Chen and Paul A. Salamie. A mathematical model for calculating the dent initiation loads at the door centers. Paper 841201, SAE, 1984.

[26] H. Sakai, K. Saito, and H. Tsukada. Stiffness and dent characteristics of body outer surface panel - finite element analysis and experiment. *Inernational Journal of Vehicle Design*, 4(1):13–22, 1983.

[27] Chung-Hsin Chen, Prabhat K. Rastogi, and Curt D. Horvath. Effects of steel thickness and mechanical properties on vehicle outer panel performance: Stiffness, oil canning load and dent resistance. In *Automotive Body Materials IBEC'93*. IBEC, 1993.

[28] C. L. Alaniz and J. E. Borchelt. Study of parameters that affect body panel performance predictions. Paper 910289, SAE, 1991.

[29] Ming F. Shi, David J. Meuleman, Christine L. Alaniz, and Stephen J. Zurdosky. Prestrain effects on static dent resistance of automotive steels. Paper 910288, SAE, 1991.

[30] F. Gatto and D. Morri. Forming properties of some aluminium alloys sheets for car - body use. In *12th Biennal Congress International Deep Drawing Research Group*. IDDRG, May 1982.

[31] A. Daglish and D.J. Cunnane. The static dent resistance of autobody alloys as a function of strain. Technical Report BR-81/77, ALCAN, 1981.

[32] Ming F. Shi and J. S. Wilczynski. Potential weight savings versus dent resistance performance of high strength steel body panels. In *Automotive Body Materials IBEC'93*. IBEC, 1993.

[33] Ronald P. Krupitzer and Rodney P. Harris. Improvements in the dent resistance of steel body panels. Paper 920243, SAE, 1992.

[34] Daniel J. Schaeffler. Procedures for dent resistance evaluations of automotive outer body panels and assemblies under quasi-static and dynamic indenting conditions. Technical Report 1.0, Auto / Steel Parnership Standardized Dent Resistance Test Task Force, January 1997.

[35] Aleksy A. Konieczny, Yishan Qiu, and Balbir Singh. A practical program set for stiffness / dent resistance calculation of autobody outer panels. In *Automotive Body Materials IBEC'97*, pages 54–58. IBEC, 1997.

[36] K.S. Raghavan and Naji Arwashan. Analysis of quasi-static denting behavior of automotive sheet steels. Paper 970984, SAE, 1997.

[37] M. F. Shi, J. A. Brindza, P. F. Michel, P. Bucklin, P.J. Belanger, and Jr. J. M. Prencipe. Static and dynamic dent resistance performance of automotive steel body panels. Paper 970158, SAE, 1997.

[38] Ravi Chavali and Wenhui Song. Coupling forming and denting simulation for automotive closure panels. Unknown Origin, 1996. Paper Number 96NM098.

[39] J.W. Phillips and H.H Calvit. Impact of a rigid sphere on a viscoelastic plate. *Journal of Applied Mechanics*, pages 873–878, December 1967.

[40] Chi-Mou Ni. Analysis of panel dent resistance. Internal Report N77 10290, General Motors, 1976.

[41] Peter T. Vreede, Paul J. Tamis, and Mary E. Roelofsen. The influence of material properties and geometry on dynamic dent resistance: Experiments and simulations. In *Materials and Body Testing IBEC'95*, pages 79–86. IBEC, 1995.

[42] Ming F. Shi, David J. Meuleman, Christine L. Alaniz, and Stephen J. Zurdosky. An evaluation of the dynamic dent resistance of automotive steels. Paper 910287, SAE, 1991.

[43] New dent resistance data. Dow Metal Products News, December 1960.

[44] Sidney H. Greenfeld. Hail resistance of roofing products. Paper, United States Department of Commerce, National Bureau of Standards, August 1969. CODEN: BSSNB.

[45] Larry Sutak. ALCAN, Private communication.

[46] John O. Hallquist. *LS-DYNA THEORETICAL MANUAL*. Livermore Software Technology Corporation, 1998.

[47] Pamstamp software. ESI Group Headquarters, 6, rue Hamelin, BP 2008-16 75761, Paris Cedex 16 France.

[48] Optris virtual press software, 2000. Dynamic Software, Vincent FERRAGU 5, Parc Club du Golf, 13856 Aix-en-Provence Cedex 3, France.

[49] Autoform 2.1 - finite element software, 2000. AutoForm Engineering GmbH, Technoparkstrasse 1, CH-8005 Zurich Switzerland.

[50] Eric T. Harpell. Numerical prediction of limiting draw ratio in aluminum cylindrical cup drawing. M.eng, Carleton University, Ottawa, Ontario, May 1997.

[51] Chantal G. Lamontagne. Numerical simulation of aluminum sheet forming incorporating plastic anisotropy. M.eng, Carleton University, Ottawa, Ontario, May 1996.

[52] J. C. Gelin and P. Picart, editors. *Proceedings of NUMISHEET '99*, volume 2, Beasancon - France, September 1999. Benchmark A - Forming of a Front Door Panel.

[53] *ABAQUS/Standard Theory Manual.* Hibbit, Karlsson & Sorensen, 1080 Main Street Pawntucket, RI 02860-4847 USA, 1997. Version 5.7.

[54] Xiao Zhou. Numerical prediction of springback in u-channel forming of aluminum tailor welded blanks. M.eng, Carleton University, Ottawa, Ontario, October 1999.

[55] *MARC Nonlinear Finite Element Solver.* MARC Analysis Research Coorporation.

[56] *LS-DYNA USERS'S MANUAL (Nonlinear Dynamic Analysis of Structures in Three Dimensions), Version 940.* Livermore Software Technology Corporation, 1997.

[57] B. Hodgins, M. Worswick, D. Thomas, M. Finn, and K. Gong. Dent resistance of medium scale aluminum structural assemblies. Paper 01B-119, SAE, 2001.

[58] *Standard Template Library Programmer's Guide*. Silicon Graphics Computer Systems, Inc., 1996.

[59] *CDE 2.1/Motif 2.1 User's Guide*. The Open Group, 29B Montvale Ave, Woburn MA 01801 USA, 1997.

[60] Pralay Dakua. Free source code downloaded from the internet, July 1997. ftp://ftp.x.org/contrib/widgets/motif/Tab.

[61] T. Belytschko and C.S. Tsay. Explicit algorithms for nonlinear dynamics of shells. *AMD*, 48:209–231, 1981.

[62] T. Belytschko, J.Lin, and C.S. Tsay. Explicit algorithms for nonlinear dynamics of shells. *Computer Methods in Applied Mechanical Engineering*, 42:225–251, 1984.

[63] T.J.R. Hughes and W.K. Liu. Nonlinear finite element analysis of shells: Part ii. three dimensional shells. *Computer Methods in Applied Mechanics*, 27:331–362, 1981.

[64] Michael E. Mortenson. *Geometric Modeling*. John Wiley and Sons, Inc., New York, 2 edition, 1997.

[65] *LS-TAURUS Data Base*. Livermore Software Technology Corporation, 1998.

[66] *LS-POST User's Manual*. Livermore Software Technology Corporation, 1998.

[67] *ABAQUS/Standard User's Manual*. Hibbit, Karlsson & Sorensen, 1080 Main Street Pawntucket, RI 02860-4847 USA, 1997. Version 5.7.

[68] LSTC. *LS-DYNA USERS'S MANUAL (Nonlinear Dynamic Analysis of Structures in Three Dimensions), Version 950*. Livermore Software Technology Corporation, 1999.

[69] D. J. Lloyd. Aluminum alloys used in automotive skin sheet. In D.S. Wilkinson, W.J. Poole, and A. Alpas, editors, *Advances in Industrial Materials*, pages 3–17. The Metallurgical Society of CIM, 1998. ISBN: 0919086-79-9.

[70] John A. Schey. *Introduction to Manufacturing Processes.* M$^{\text{C}}$ Graw Hill, 3 edition, 1999.

[71] W.T. Lankford, S.C. Snyder, and J. A. Bauscher. *Transactions of the ASM*, 42:1197, 1950.

[72] Theodore Baumeister, Eugene A. Avallone, and Theodore Baumeister III, editors. *Marks' Standard Handbook for Mechanical Engineers.* McGraw-Hill Book Company, 8 edition, 1978.

[73] R. Sowerby and J. L. Duncan. Failure in sheet metal in biaxial tension. *International Journal of Mechanical Science*, 13:217–229, 1971.

[74] J. C. Simo and F. Armero. Geometrically non-linear enganced strain mixed methods and the method of incompatible modes. *International Journal for Numerical Methods in Engineering*, 33:1413–1449, 1992.

[75] William F. Hosford and Robert M. Caddell. *Metal Forming - Mechanics and Metallurgy.* Prentice Hall, 2 edition, 1993.

[76] B. Maker. On drawbeads in sheet metal forming. Paper 2000-01-0776, SAE, 2000.

[77] Fred Barlat and J. Lian. Plastic behavior and stretchability of sheet metals. part 1: A yield function for orthotropic sheets under plane stress conditions. *International Journal of Plasticity*, 5:51–66, 1989.

[78] B. Maker, 1999. Livermre Software Technology Corporation.

[79] Fred Barlat. Private Communication, 2000.